Porous membranes for interfacing microfluidics with cell cultures

by

Christopher G. Sip

A dissertation

submitted in partial fulfillment of the

requirements for the degree of

Doctor of Philosophy

The University of Washington

2013

Reading Committee:

Albert Folch, Chair

Charles Frevert

Rachel Wong

Paul Yager

Program Authorized to Offer Degree:

Bioengineering

Dedication

With love to Dani

Acknowledgements

First, I would like to express my sincere gratitude to my advisor, Albert Folch. His creativity, motivation, and support have been invaluable throughout my Ph.D. years. I would like to thank Dr. Paul Yager for his thought provoking questions and valuable support with microfluidic problems. I am also thankful to Dr. Charles Frevert and Dr. Rachel Wong for advising me on chemotaxis assays and providing their biology expertise. I would also like to thank Nirveek Bhattacharjee for his willingness to listen and provide immeasurable guidance on all topics encountered in this research. During my time in the Folch Lab, I have had the opportunity to work with a fantastic group. I would like to extend special thanks to Tim Chang, Anthony Au, Samira Moorjani, Jonathan Cheng, and Lisa Horowitz for their enormous help and camaraderie throughout.

The University of Washington

Porous membranes for interfacing microfluidics with cell cultures

Christopher G. Sip, Ph.D.

2013

Chair of the Supervisory Committee:

Albert Folch, Department of Bioengineering

The sensing of chemical gradients plays an important role in the guidance of cells for tissue development, migration of cells in the immune system, and human disease. We have developed a microfluidic transwell insert for generating concentration gradients in a user-friendly and modular format that is compatible with conventional cell cultures. The device is simply inserted into a standard 6-well plate were it hangs self-supported at a distance of 250 μm above the cell culture surface. The core aspect of our design is the delivery of small microflows through a track-etched membrane into the cell culture well. The microfluidic transwell can deliver quantifiable, large-area gradients to a large number of cells or tissue explants with extremely low fluid shear stress. Finite-element modeling was used to describe porous membrane flow and molecular transport for predicting gradients generated by the device. Transwell microfluidic gradients were applied to a large population of neutrophil-like cells to demonstrate the direct observation of chemotaxis. Additionally, the modular design and low fluid shear stress made it possible to apply gradients to sensitive neuronal explant cultures. With a simplified interfacing scheme and well-defined, quantifiable gradients, the microfluidic transwell device has potential for broad applications to gradient sensing biology.

Table of Contents

List of Tables xii

List of Figures xiii

Chapter 1: Introduction 19

1.1 Introduction 19

1.2 Mechanisms of Gradient Formation 20

Principle of gradient generation between a source and sink 20

Formation of gradients in vivo 21

1.3 Conventional In Vitro Gradient Assays 23

1.4 Microfluidic Methods 26

Flow-based gradient generation 26

Flow-free gradient generation 26

Microjets device 28

Porous membrane-based microfluidic gradient generation 29

1.5 Commercialized Microfluidic Gradient Devices 30

1.6 Criteria for Cell Culture-Friendly Microdevices 32

1.7 Executive Summary 33

1.8 References 33

Chapter 2: Modular Microfluidic Design and Gradient Generation 41

2.1 Introduction 41

2.2 A Multi-Purpose Microfluidic Perfusion System with Combinatorial Choice of Inputs, Mixtures, Gradient Patterns, and Flow Rates 42

2.3 Modular Microfluidic Systems Using Reversibly Attached PDMS Fluid Control Modules 45

2.3.1 A self-aligning modular system for fluid automation 46

2.3.2 Summary and assessment of the method 50

2.4 A Modular Cell Culture Device for Generating Arrays of Gradients Using Stacked Microfluidic Flows 51

2.4.1 Methods and results 52
Fabrication of the stacked flow device 52
Stacked flow device operation 54
Finite-element modeling of stacked flows 56
Surface gradient detection 56
Cell culture and time-lapse imaging 56
2.4.2 Results and discussion 57
FEM predicts wide-area gradients and low shear forces at the surface 57
Large-area surface gradients can be dynamically tuned 58
Vacuum sealing operation and stacked-flow is benign to cell culture preparations 61
Scalable architecture enables arrays of multiple gradients 63
2.4.3 Summary and assessment of the method 65
2.5 An Open-Surface Micro-Dispenser Valve for the Local Stimulation of Conventional Tissue Cultures 67
2.5.1. Micro-dispenser device design for controlled stimulation 68
2.5.2. Methods and Results 70
Fabrication 70
Micro-dispenser valve sealing pressure 71
Surface-fluorescence characterization 73
2.5.3. Summary and assessment of the method 74
2.6 Irreversible Bonding of SU-8 Microstructures onto PDMS devices 75
2.6.1. Methods and results 76
SU-8 dry release method 76
Fabrication and pressure testing of PDMS-SU-8 hybrid devices 77
2.6.2 Summary and assessment of the method 79
2.7 A Microfluidic Platform for Generation of Sharp Gradients in Open-Access Culture 80
2.7.1. Methods and results 82

Adhesive-free fabrication of PDMS devices with integrated membranes 82
Characterization of laminar flow stability and gradient shape ... 83
Application of a sharp gradients to cells using live-cell florescent stains 86
2.7.2 Summary and assessment of the method 89
2.8 Summary 89
2.8.1 Microfluidic automation: from integrated systems to modular design 89
2.8.2 Interfacing microfluidics with cell cultures 90
2.8.3 Conclusions 91
2.9 References 92

Chapter 3: Stable chemical bonding of porous membranes and PDMS devices for long-term cell culture 98
3.1 Introduction 98
3.2 Materials and Methods 99
3.2.1 Materials 99
3.2.2 Silane treatment of PET track-etched membranes 100
3.2.3 X-ray photoelectron spectroscopy analysis 101
3.2.4 Fabrication of open-surface PDMS-PET membrane device 102
3.2.5 C2C12 cell culture and calcein AM stimulation 103
3.3 Results and Discussion 103
3.3.1 Evaluation of different silanes treatment for bond stability in DMEM at 37 °C 103
3.3.2 XPS analysis of surface composition of silane modified PET and degradation of silane layer 107
3.3.3 Demonstration of long-term culture and basal-side stimulation of differentiated myotubes 110
3.3.4 Rapid delamination is predicted for devices with a porous surface in contact with medium 111
3.4 Conclusions 114
3.5 References 115

Chapter 4: Microfluidic Transwell Inserts 118
4.1 Introduction 118
4.1.1 Microfluidic transwell inserts 119
4.1.2 Track-etched membranes 120
4.2 Fabrication of Microfluidic Transwell Devices 123
4.2.1 Multilayer soft-lithography 123
4.2.2 Embedding of PDMS into plastic supports 125
4.2.3 Exclusion molding of thin PDMS layers 126
4.2.4 Plasma bonding assembly and silane coupling of membranes 127
4.3 Design of Membrane Micro-Flows 128
4.3.1 Hydraulic-electric circuit analogy 128
4.4 Finite-Element Modeling of Devices 134
4.4.1 3D finite-element model and method 134
4.4.2 Time dependent simulations of concentration gradient development 140
4.4.3 Parametric study of flow rate and diffusivity sensitivity 142
4.4.4 Shear stress at the cell culture surface 144
4.5 Operation of Devices 145
4.6 Characterization of Diffusible Gradients 147
4.6.1 Orange-G for characterization of surface-level gradients 148
4.6.2 Diffusible Tracers for Epi-Fluorescence Live-Monitoring 150
4.7 Applications of Microfluidic Transwell Inserts to Cell and Tissue Cultures 152
4.7.1 HL-60 cell culture and device preparation 152
4.7.2 Tracking of neutrophil migration and chemotaxis 154
Image processing and automated tracking of cells 155
TrackMate automated tracking of cell migration 156
Statistical analysis of chemotaxis parameters 158
4.7.3 Application to Retinal Explant Tissue Cultures 162
Automated analysis of axon directionality 164

4.8 Summary and Future Work 167
4.9 References 168

List of Tables

Table 3.1: Comparison of APTES and bis-amino silane in polar aprotic solvent.....105

Table 3.3: Comparison of APTES and bis-amino silane bonding with anhydrous solvent.....107

Table 3.4: Elemental composition for freshly silane treated samples 109

Table 3.5: Elemental composition for freshly silane treated samples 110

Table 4.1: Formulation for Gey's medium used in HL-60 chemotaxis assays.....153

Table 4.2: Results of chemotaxis and control experiments with the Rayleigh test for a circular distribution.....160

Table 4.3: Results for Fourier spectrum analysis of retinal explant outgrowth.....165

List of Figures

Figure 1.1: Generation of gradient via diffusive transport between a source and sink. 22
Figure 1.2: Conventional in vitro assays for gradient generation. 25
Figure 1.3: Flow-based microfluidic gradient generation. 27
Figure 1.4: Flow-free microfluidic gradient generation. 28
Figure 2.1: Overview of multi-purpose perfusion device design. 43
Figure 2.2: Operation of the multiplexer for selection of individual inlets. 44
Figure 2.3: Control of gradient flow patterns in the central chamber. 44
Figure 2.4: Overview of the modular microfluidic system. 47
Figure 2.5: Soft-lithography fabrication of the PDMS control module. 48
Figure 2.6: PDMS fluid control module layout. 48
Figure 2.7: Examples of different designs for cell culture modules. 49
Figure 2.8: Demonstration of automated fluid handling in a PMMA chip used colored dyes. 49
Figure 2.9: The stacked flow device and gradient simulation. 52
Figure 2.10: Schematic illustration of fabrication process and operation of the vacuum-sealing stacked-flow gradient device. 55
Figure 2.11: Finite-element modeling and fluorescence characterization of surface gradients. 60
Figure 2.12: Finite-element modeling of surface gradients generated using stacked flows demonstrates dynamic tunability. 61
Figure 2.13: Vacuum sealing of the stacked-flow device to an established culture of MDA-MB-231 breast cancer cells. 63

Figure 2.14: The scalable stacked-flow architecture enables arrays of gradient generators for high-throughput screening. 65
Figure 2.15: Micro-dispenser device design. 69
Figure 2.16: The principle of operation for the micro-dispenser stimulation device. 70
Figure 2.17: Multilayer soft-lithography fabrication of the micro-dispenser. 71
Figure 2.18: Sealing pressures for varying device parameters of the micro-dispenser device. 72
Figure 2.19: Surface-level fluorescence characterization of micro-dispenser stimulation. 74
Figure 2.20: SU-8 dry release substrate treatment and method. 77
Figure 2.21: Hybrid PDMS/SU-8 devices with high-resolution and large arrays of apertures. 79
Figure 2.22: Fabrication schematic for the open-surface gradient device using an integrated track-etched membrane. 84
Figure 2.23: Gradient stability analysis using surface-fluorescence microscopy. 85
Figure 2.24: Staining of fluorescent gradients in an open cell culture device. 88
Figure 2.25: Micro-to-macro interfacing of integrated microfluidic devices. 90
Figure 2.26: Image contrast of cells grown on a track-etched membrane. 91
Figure 3.1: Schematic of the idealized surface modification reaction between PET membranes and bis-amino silane. 101
Figure 3.2: XPS elemental composition analysis for silane treated PET samples. 108

Figure 3.3: Example XPS survey spectra for PET track-etched membranes....109
Figure 3.4: An open-surface basal-side stimulation device using track-etched membranes. 111
Figure 3.5: Rapid delamination is predicted membranes bonded with an open-surface. 114
Figure 4.1: 3D rendering of the microfluidic transwell insert and 6-well plate assembly. 121
Figure 4.2: 3D rendering of the microfluidic transwell insert and cross-sectional views.....122
Figure 4.3: Top and cross-sectional views of the microfluidic transwell insert. 122
Figure 4.4: Photographs of a microfluidic transwell insert loaded with colored dyes.....123
Figure 4.5: Multilayer soft-lithography and plasma bonding assembly of devices. 124
Figure 4.6: Embedding of microchannel layer in plastic supports. 126
Figure 4.7: Exclusion molding of thin PDMS layers.....127
Figure 4.8: Hydraulic circuit for microfluidic transwell flows depicting the flow network for one inlet. 132
Figure 4.9: Hydraulic circuit for a microfluidic transwell device with 2 inlets and a common outlet.....133
Figure 4.10: Contextual diagram of the simulated region and FEM geometry. .135
Figure 4.11: Representative FEM geometry, meshing, and steady state solution for microfluidic transwell inserts.....137

Figure 4.12: Steady-state simulation of flow in the microfluidic transwell device. 138
Figure 4.13: Enlarged cross-sectional profile for the steady-state flow velocity generated in the external fluid space. 139
Figure 4.14: Steady-state simulation of surface concentration for a microfluidic transwell gradient. 140
Figure 4.15: Time dependence of microfluidic transwell gradients. 141
Figure 4.16: Convection and diffusivity dependence of microfluidic transwell gradients. 143
Figure 4.17: Local Peclét number analysis of simulated microfluidic transwell gradients. 143
Figure 4.18: Fluid shear stress at the cell culture surface for microfluidic transwell gradients. 145
Figure 4.19: Experimental setup for device operation, cell culture, and microscopy. 147
Figure 4.20: Characterization of the microfluidic transwell gradients using surface-fluorescence. 149
Figure 4.21: Demonstration of tunable gradients through rotation of the device. 150
Figure 4.22: Live-monitoring of microfluidic transwell gradients using fluorescent tracers. 151
Figure 4.23: Large-area image stitching for time-lapse tracking of HL-60 migration during chemotaxis experiments. 154

Figure 4.24: Monitoring of the 100 nM fMLP gradient with a fluorescent tracer during time-lapse of HL-60 chemotaxis. 155
Figure 4.25: Image processing setup for automated identification of cell bodies with Image J. 156
Figure 4.26: TrackMate plugin generated tracks for HL-60 cells and a 100 nM fMLP gradient. 157
Figure 4.27: A TrackMate sequence showing the tracking of cells in crowded regions. 158
Figure 4.28: Trajectory plots for 100 nM fMLP gradient and controls showing the cumulative traces of each individual cell tracked. 160
Figure 4.29: Statistical analysis of chemotaxis for HL-60 migration experiments. 161
Figure 4.30: E15 mouse retinal explants after 40 h cultured with BDNF and CNTF growth factors. 162
Figure 4.31: Application of a microfluidic transwell gradient of BDNF and CNTF growth factors to a retinal explant cultured 3 days in vitro. 163
Figure 4.32: Repositioning of the microfluidic transwell and application of a new gradient using a cAMP analog. 164
Figure 4.33: Fourier spectrum analysis of neuronal outgrowth for gradients of growth factors applied at 0° and cAMP at 45°. 166

Chapter 1: Introduction

1.1 Introduction

The sensing of chemical gradients plays an important role in the guidance of cells for tissue development[1], migration of cells in the immune system[2], and human disease[3]. Gradients of morphogens guide the development of tissue and organ structure[4], chemokines recruit leukocytes and lymphocytes during the inflammatory response[2,5], and guidance factors direct axon path finding in the developing nervous system[6–8]. Pathological gradient sensing mechanisms are involved in cancer metastasis[9], autoimmune diseases[10], infections, implant rejection, and chronic inflammatory diseases[11]. Modeling of receptor-ligand interactions, molecular transport, and cellular mechanisms has elucidated many of the processes involved in gradient sensing[4,12,13]. Continued efforts to further our understanding of gradient biology are important to the development of drugs and therapeutic interventions. For example, stem cells naturally migrate to the site of injury for regenerative stem cell therapy[14–17], and engineered T-cells are designed to target cancer for adoptive immunotherapy[18].

With the broad relevance of gradient sensing in biology, manipulation of the cell microenvironment is a critical technique for in vitro research. Currently, there exist a wide range of techniques available for conducting in vitro gradient assays, yet efforts to improve the quantification of gradients and facilitate compatibility with cell culture remain ongoing[19]. For the generation of quantifiable gradients, microfluidic methods have been most promising, however, cell culture compatibility has been a limitation to wider acceptance. In this chapter, we will discuss mechanisms of gradient formation and review commonly used conventional and microfluidic methods to apply gradients in vitro. We will draw upon the best features and limitations of these techniques to define ideal criteria for cell culture-friendly assays.

1.2 MECHANISMS OF GRADIENT FORMATION

In order to compare methods for generating gradients, we must first understand the basic principles and limitations of diffusive transport. The basic mechanism for generating gradients is the physical transport of chemical species by diffusion. The diffusive flux, movement of solutes from regions of high concentration to regions of low concentration, and the change in concentration over time are described by Fick's laws of diffusion[20]. The diffusion coefficient of a species is related to the molecular weight (MW) by

$$D \sim \frac{1}{MW^{1/3}} \quad (1)$$

The diffusion length characterizes the amount of time required for a chemical to diffuse across a distance:

$$t = \frac{L^2}{2D} \quad (2)$$

where D is the diffusion coefficient in units of $m^2\ s^{-1,}$ t is the diffusion time, and L is the diffusion length. Eqs. (1) and (2) relate the effect of molecular weight on the spread of concentration with time.

Principle of gradient generation between a source and sink

A linear concentration gradient is generated across a region at steady state when the boundaries serve as a source and sink (fixed at concentrations of C = 0 and C =1). However, the time required to reach steady state is dependent on the chemical species and distance between boundaries as shown in **Figure 1.1**. For chemical species of higher molecular weight, the diffusion coefficient is slower, which increases the time as described by Eq. (1). For greater distances, the time increases proportionally to the square of the length. The diffusion times calculated for simulations in **Figure 1.1**

demonstrate that for large distances and slow diffusing species, the time for reaching steady state becomes quite limiting for practical purposes.

Formation of gradients in vivo

Unsurprisingly, the formation of gradients in vivo is more complex than the simple example of free diffusion described in **Figure 1.1**. Due to interactions with other molecules in the extracellular matrix (ECM) or interstitial space, the effective diffusivity would be lower than for dilute and free solutions[4]. Other mechanisms proposed to regulate gradients include binding to cell surface or ECM factors such as heparin sulfates[21], depletion by endocytosis[22], regulation of cell secretion by a gradient of mRNA expression across tissue[23], and elongation of gradients by subtle interstitial flow[24,25]. With the diversity of gradients formed in vivo, assays must be flexible enough to generate gradients for a wide range of molecular weights and distances in a quantifiable manner.

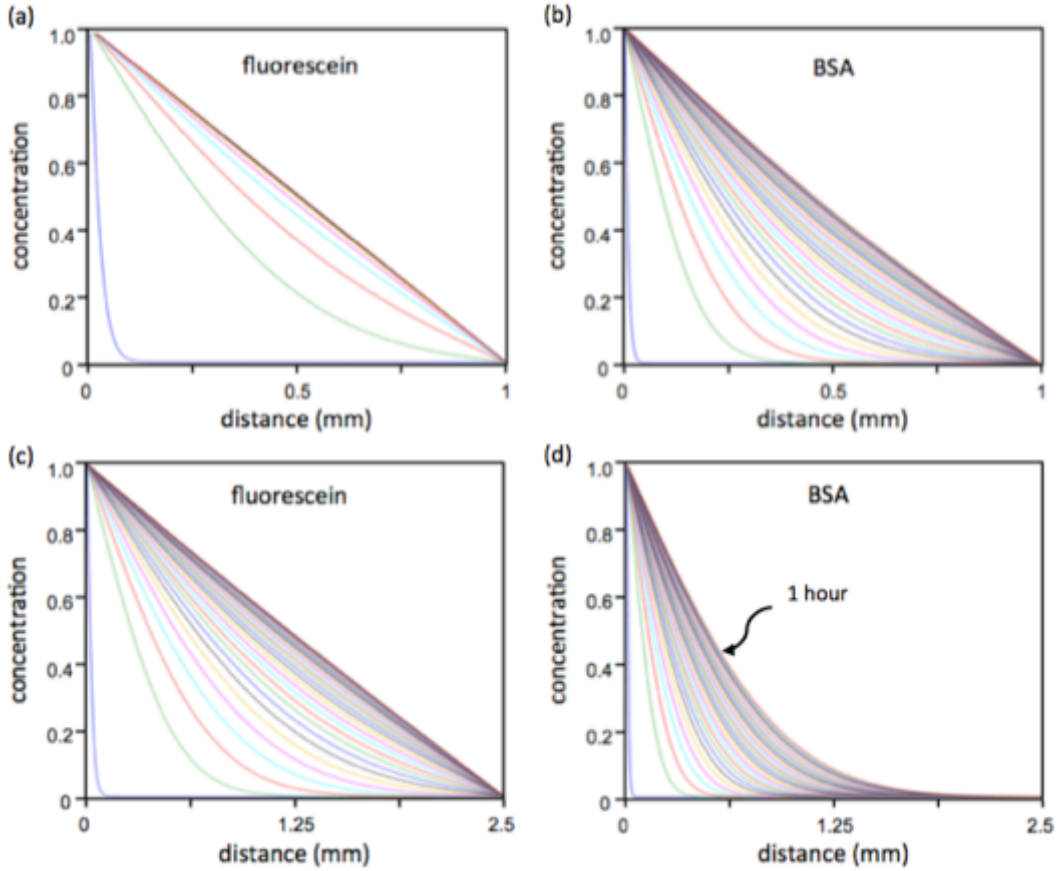

Figure 1.1: Generation of gradient via diffusive transport between a source and sink. In each plot the left edge represents a boundary condition with an unlimited source of the chemical species, C = 1, whereas the right boundary represents an unlimited sink, C = 0. The transport of the chemical species in the space between (initially at C = 0 for t = 0) is described by Fick's second law of diffusion for the change in concentration with time. Each trace represents the concentration distribution at 2 min intervals from t = 0 to 1 h. (a) Fluorescein ($D = 6.4\times10^{-10}$ m^2 s^{-1}) reaches steady state at 0.217 h. (b) Bovine serum albumin (BSA, $D = 0.72\times10^{-10}$ m^2 s^{-1}) reaches steady state after 1.35 h. For a distance of 2.5 mm, (c) fluorescein reaches steady state at 1.93 h, and (d) BSA at 12.1 h (not shown). The effects of increasing molecular weight and thus the diffusion coefficient can be seen comparing (a, c) fluorescein with (b, d) BSA. For larger distances between the source and sink (c, d) require more time to steady state. For slowly diffusing molecules and large distances, transport via only diffusion requires large time scales to reach steady state.

1.3 Conventional In Vitro Gradient Assays

Conventional in vitro technique has relied primarily on 4 types of assays to apply concentration gradients to cell and tissue cultures: porous membranes[26,27], micropipette assays[28–32], chamber assays[33–36], and gel assays[37–42]. These approaches to in vitro gradient stimulation have several key features and limitations that determine their preferred use. The porous membrane assay (**Figure 1.2(a)**), also known as the Boyden chamber[26] and by several brand names such as Transwell, is based on quantifying the migration of cells through the pores of a thin membrane. (3-12 μm diameter pores, 10-20 μm thick membranes) Migration or chemotactic potential can be measured by counting the amount of cells that traverse through the membrane. The gradient and cell migration is difficult to visualize and occurs across a short distance, therefore the technique is best used as an indirect screening tool for potential chemotaxis factors and cell types. Other techniques must be used to make direct observations of cell migration or morphological changes.

The micropipette assay (**Figure 1.2(b)**) is most often used to probe single-cell responses[28–32]. The gradient is generated by applying pulsatile pressure to a fine-drawn glass pipette with an orifice of approximately 1 μm in diameter. Using a micromanipulator, the micropipette is positioned at a close proximity to the target cell. For example, gradients can be generated at precise distances and angles relative to a growth cone in order to observe axon guidance. The complex, radial shape of micropipette gradients have been quantified and mathematically modeled[43]. However, the technique is limited to generating steep gradients across short distances (100-150 μm) and is therefore best suited for observations of single-cell responses. Additionally, the assay is preformed in an open bath that limits use for long-term experiments (assays with *Xenopus* neurons are typically performed at room temperature for a few hours). Since

cells are probed sequentially, the method could be susceptible to experimental bias and subtle behaviors may go undiscovered.

We define chamber assays (**Figure 1.2(c)**) to include several different devices based on generating a gradient across a narrow region separating two static fluid compartments[33,34,36]. The first devices were machined from plastic or glass slides and assembled with coverslips as demonstrated by Zigmond[33] and Dunn[34]. More recently pre-assembled slides have been developed with pipette accessible compartments to facilitate device operation and scalability[36]. The basic principle of this design is to generate linear gradients by the diffusion of factors across the narrow region separating fluid compartments (10-70 μm tall, 1 mm long and arbitrarily wide); however the volume of each solution is finite and therefore gradients achieve a pseudo-steady state condition for several hours only. The main advantage of the chamber assay technique is the ability to directly observe individual responses of cells using standard microscopy technique (typically 50-100 cells). Direct viewing of cells in large numbers strengthens statistical analysis and enables richer observations about cell behaviors and morphological changes. However, challenges with maintaining cell cultures with small fluid volumes in the enclosed chambers limit the assay for long-term experiments.

Gel assays (**Figure 1.2(d)**) refer to a wide range of experimental methods that rely on restricted diffusion in a porous matrix of agarose or ECM proteins like collagen[37–42]. These techniques can accommodate different types of dissociated cells or tissue explants. Chemoattractants or chemorepellants can be injected into the gel adjacent to a cell population[37], opposing gradients can be established with combinations of factors[42], transfected cells can be cultured adjacent to target cells or tissue[40], or beads can be loaded with factors to control release[21,44]. The flexibility of the method enables researchers to tailor the conditions for their specific application; however, the consequence is that

across different examples reported in the literature, the actual concentrations are difficult to quantify. Additionally, the porous matrix of the gel decreases image contrast, making direct visualization of individual cells and neurites impossible without staining[37,40].

A wide range of biological questions has been studied using these conventional gradient assays. However, across these assays, there is a compromise between the number of cells, length of gradients, quality of imaging, and ease-of-use. These limitations and the desire to control the timing and shape of gradients, have motivated development of new assays based on microfluidic technology.

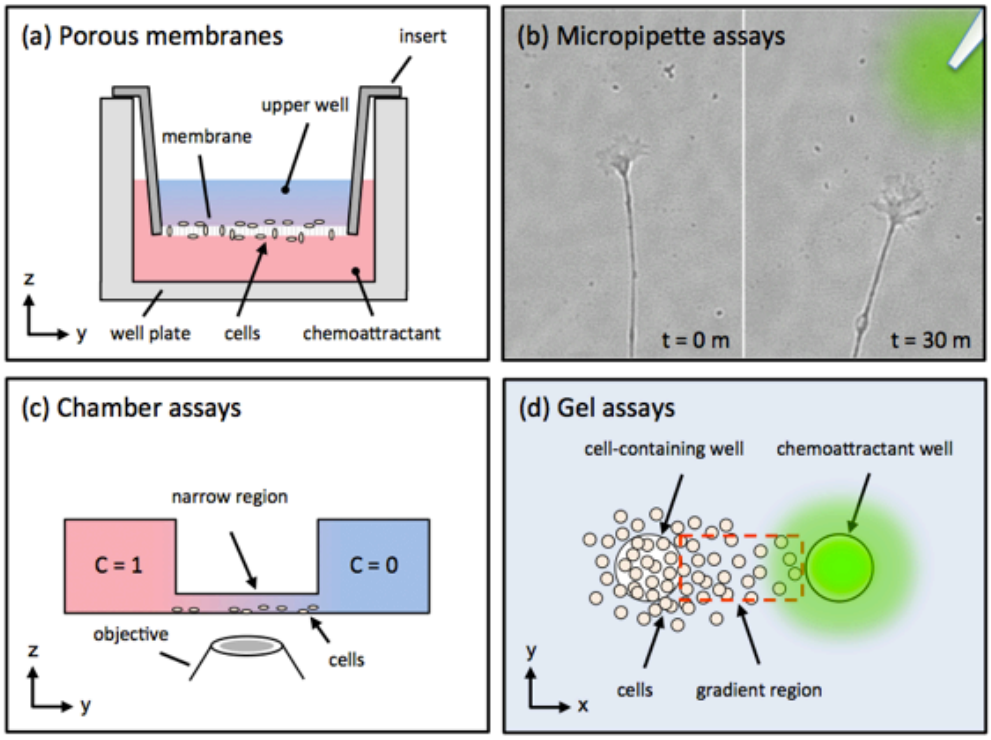

Figure 1.2: Conventional in vitro assays for gradient generation. (a) Cells migrate through the porous of a suspended membrane from the upper well towards the chemoattractant containing lower well. (b) A micropipette produces a local gradient adjacent to the growth cone of a neuron to elicit a turning response. (c) Cells migrate across a narrow region (10-70 μm) towards a chemoattractant compartment in a pseudo-steady state gradient formed by diffusion. (d) Cells embedded in a gel migrate through the porous matrix in a response to a gradient eluted from a chemoattractant containing well.

1.4 MICROFLUIDIC METHODS

Flow-based gradient generation

The effort to develop more sophisticated methods for generating gradients has been largely focused on microfluidic techniques. Microfabrication and laminar flow at small scales make possible precise spatial and temporal control for generating stable, quantifiable, and reproducible gradients[19,45,46]. The first flow-based devices used microchannel networks to control mixing of titrations and produced gradients from laminar streams[47] (**Figure 1.3**). A variety of mixing schemes have been explored to produce gradients having arbitrary shapes[48,49]. Flow-based gradient devices have been used to study a range of gradient sensing biology including chemotaxis[50,51], differentiation[52], and cancer cell migration[53]; however fluid shear stress exerted on cells has been a major limitation[54]. Wang et al.[55] demonstrated the integration of microfabricated trenches as a solution to protect neurons from shear within the device. Still, the designs are rather complex and additional concerns regarding culture within microchannels limit their wider use[56,57].

Flow-free gradient generation

Others have demonstrated control of gradients using diffusion of solutes in flow-free conditions. Drawing inspiration from the chamber and gel assays described earlier, these devices use microchannel restrictions or embedded gels to establish static fluids and gradients by diffusion (**Figure 1.4**). Typically flows through adjacent microchannels are used to intermittently exchange solutions for short-term gradients[58] or maintain steady state[59,60]. Variations of device geometry such as channel spacing, heights, and design enable generation of gradients having different shapes[60–67]. Confinement of cells in restrictive microchannels has also been demonstrated to enhance motility[68,69], localize gradients relative to individual cells[70,71], and study decision-making with bifurcating

channels[72,73]. Since gradient generation is based on diffusive mixing, flow-free devices are generally simpler to operate, negate harmful shear flow, and many are pipette accessible. However, slow time scales for gradient evolution limit dynamic control of gradients, and the visualization of cells in gels is less than optimal.

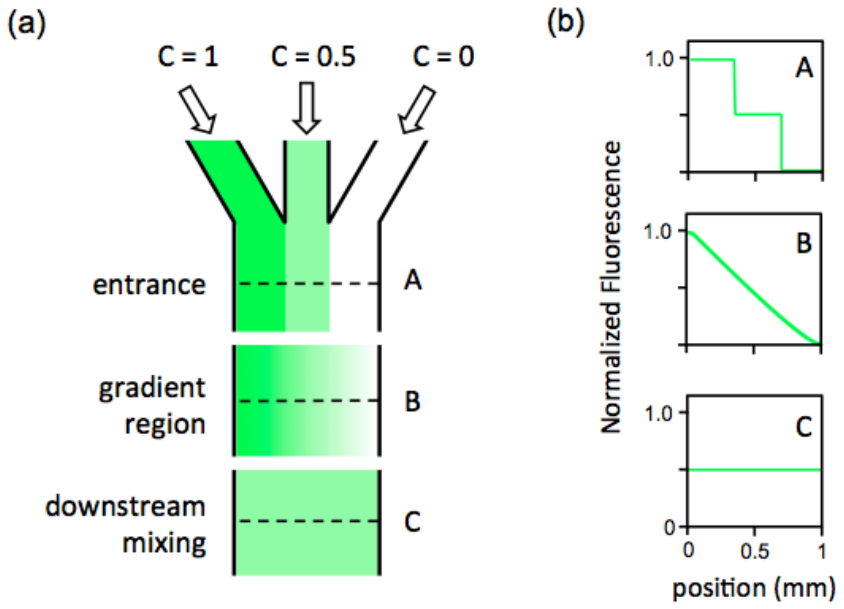

Figure 1.3: Flow-based microfluidic gradient generation. (a) On-chip titrations merge at the entrance to a central cell culture channel with laminar flow. A stepwise concentration profile is initially produced that mixes downstream to form a smooth gradient. (b) Concentration profiles are shown for positions A, B, and C. The amount of mixing at a given distance downstream is a function of the diffusion time and controlled by the flow rate of the device.

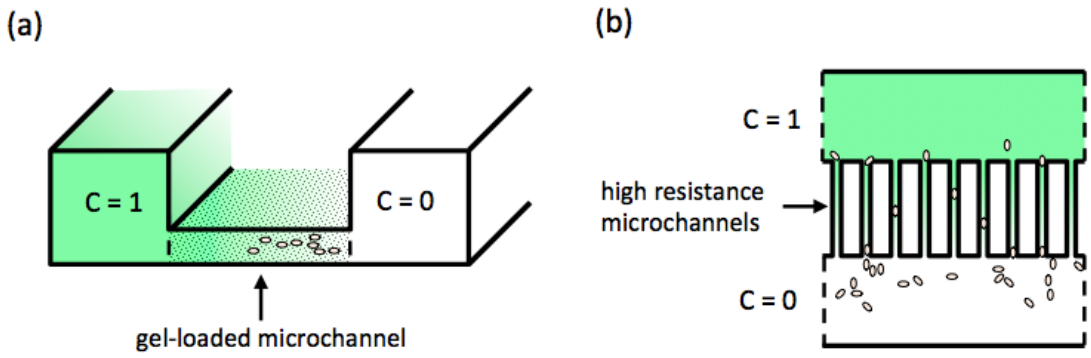

Figure 1.4: Flow-free microfluidic gradient generation. (a) Embedded gels or ECM can be used to partition microchannels to generate a gradient by diffusion. Cells are able to migrate through the porous matrix in the 3D space separating the source and sink. (b) Other designs use high resistance channels. Restricted flow and balanced pressures establish a flow-free state in which the gradient forms by diffusion. Cells squeeze through the microchannels and migrate towards the source of chemoattractant.

Microjets device

In the Folch lab, a microfluidic device having an open-surface was developed to facilitate conventional cell culture[74]. The microjets device uses flow ejected through high resistance microchannels at the cell culture surface of an open-bath. Flow entering the bath moves up and away from the surface; therefore, fluid shear stress is minimized at the cell culture surface. The low-shear and open-surface cell cultures are key features which make the device well suited for studying axon guidance, for which the culture of primary neurons is challenging[75]. However, fabrication of the devices in PDMS with exclusion-molding technique is particularly challenging, devices are prone to clogging, and difficult to operate for users not trained in microfluidic technique. While these issues could be resolved using different fabrication methods and flow driving technique, a fundamental problem is the inability to monitor the gradient during cell culture experiments. Since flow is directed upwards into a large open bath, fluorescent tracers that accumulate make

it impossible to image the gradient occurring just at the cell culture surface without using confocal microscopy. Without knowing the condition of the gradient during the course of a cell culture experiment, conflicting data or unexpected results pose a difficult problem for data analysis. Nevertheless, the microjets device is uniquely specialized for the study of large numbers of isolated, single neurons in low-shear gradients using conventional cell culture technique.

Porous membrane-based microfluidic gradient generation

More recently, several devices have been demonstrated in which integrated porous membranes deliver gradients to cell cultures while isolating microchannel flows[76–82]. Typically, thin porous filter membranes are used because they can be integrated directly between layers of micromolded PDMS. Several groups have used porous membranes to eliminate pressure imbalances in static fluid volumes for flow-free generation of gradients[76,78]. Maharbiz's group first demonstrated that cells cultured on a porous membrane could be stimulated with a sharp gradient through underlying flows in a separate microchannel layer[77]. The porous membrane served to isolate microfluidic and cell culture compartments while protecting cells from shear stress. VanDersarl et al.[79] demonstrated that flow-based gradient devices could be used in combination with porous membranes to isolate flow and generate complex gradients (similar to those demonstrated by Dertinger et al.[47]). Morel et al.[81] demonstrated rapid, dynamically tunable gradients controlled by flow delivered to porous membranes. Kim et al.[82] studied activation of Wnt/β-catenin signaling using diffusion- and convection-based transport in a membrane-based device. Kawada et al.[80] demonstrated spatial and temporal control of stem cell differentiation using membrane-based delivery of factors.

In these types of devices, cells have been cultured on a surface opposite the membrane[76,78,79,81] or directly on the membrane[77,80,82]. Culture opposite the membrane has

the advantage of improved optical clarity because the pores of the membrane are out of focus, whereas cells cultured directly on the membrane further restrict flow through the pores. Across reported devices, there exist a range of fabrication strategies for integrating the porous membrane due to challenges with bonding PDMS and the porous membranes. Additionally, there are various opinions regarding the ability to neglect flow through the membrane and consider only diffusive transport (for contrasting opinions compare Morel et al.[81] and VanDersal et al.[79] with Kim et al.[82] and Kawada et al.[80]). Regardless, porous membranes are a promising approach to interfacing microfluidic flows with cell cultures; however, progress will require further efforts improve fabrication techniques and characterization of membrane flows.

1.5 Commercialized Microfluidic Gradient Devices

While microfluidic-based gradient generating methods have received much attention from the engineering community, biologists to a large degree still favor the conventional methods described earlier. Partly, this may be due to lack of standardization, difficulties with device operation, and device-to-device variability inherent to PDMS-based prototyping. However, there exist several commercialized microfluidic gradient devices that have recently appeared on the market intended for direct visualization of cell cultures and generation of quantifiable gradients. In order to facilitate cell culture work, commercialized devices typically favor modular designs or simplified interfacing. Here, we will review the products available, their approach to user and cell culture friendliness, and ongoing limitations.

The Millicell μ-Migration Kit (also known as the Ibidi μ-Slide Chemotaxis Assay) is a streamlined chamber assay based on flow-free gradient generation. The device utilizes specially designed ports to facilitate loading of cells and solutions using standard plastic pipette tips[83]. Similarly, the Axis Axon Isolation Device enables neuron

culture with open wells and compartmentalizing microfluidic flows[84–88]. High resistance microchannels of this design protect neurites from shear and enable gradient generation in flow-free conditions. Similarly, the CellASIC platform uses high resistance microchannels to minimize flow and generate gradients. A sophisticated platform simplifies interfacing through specially designed manifolds to control microfluidic flow, switching, and cell culture in custom well plates[89–93]. However, the apparatus is quite complex and the initial cost is high for adopting the technology. The Iuvo Chemotaxis Assay is based on arrays of microchannels integrated in a familiar multi-well plate format[94]. It operates similarly to chamber assays, but fluid loading is simplified by surface tension-driven flow and the dispensing of precise volumes with pipettes. The specially designed multi-well plates enable scalable, high-content screening through integration with robotic fluid handling equipment. The Gradienttech CellDirector uses a modular microfluidic design with vacuum-assisted sealing to assist with cell culture[64,95,96]. The CellDirector is available with flow- or gel-based designs. For the flow-based version, gradients are limited in shape and area due to the limitations of shear flow; otherwise cells migration is biased. The alternative flow-free design uses an embedded gel, so direct visualization is hindered by poor image contrast.

Overall, the commercialized designs contribute to reliability of gradient assays with robust product manufacturing that is typical of cell culture disposables. The μ-Migration Kit, Axon Isolation device, and Iuvo Chemotaxis Assay have the simplest operation, yet flow-free operation yields time-dependent gradients. The CellAsic platform and CellDirector devices utilize flow to generate steady state gradients, however the operating apparatus is cumbersome and expensive. With the exception of the CellDirector, none of the commercialized devices are modular to enable interfacing with pre-existing cell cultures or tissue explants. Moreover, the large diversity between

products makes clear that engineers and biologists alike have not yet converged on an ideal solution to conduct chemotaxis assays.

1.6 Criteria for Cell Culture-Friendly Microdevices

For a microfluidic chemotaxis assay to achieve widespread adoption by non-microfluidic laboratories, we believe five criteria must be satisfied:

1. A quantitative measure of the gradients must be obtainable.
2. The device must allow for assaying large numbers of cells or tissue.
3. Cells must be directly observed under the microscope while in the device.
4. Operation of the device must be user-friendly by the standards of biologists.
5. Setup, operation or imaging of the gradient must be compatible with conventional cell culture techniques.

Most microfluidic methods naturally satisfy the first condition to achieve steady state or pseudo-steady state gradients that are easily monitored and quantifiable with fluorescence microscopy. Generally, designs are scalable to permit large numbers of cells for statistical analysis. On the other hand, only a complex vacuum sealing design has been demonstrated for applying gradients to intact tissue[64]. Materials are usually glass and PDMS, so optical quality is high in all devices except those using gels. Across all of the different types of microfluidic gradient devices, there is wide range of user-friendliness. Devices requiring microvalves and many fluid inputs are the least simple to operate. Gel-based devices and flow-free designs are the most straightforward to use. Closely related to user-friendliness, but difficult to satisfy, is compatibility with conventional cell culture technique. Compatible designs must use standard cell culture substrates that can be coated, seeded with cells, and incubated in the same way as traditional cell culture vessels. At this stage in the progression of microfluidic gradient designs, user-

friendliness and compatibility with conventional cell culture technique remain the most difficult challenges to address before wider acceptance can be achieved.

1.7 Executive Summary

The overarching goal of this dissertation was to develop a microfluidic gradient device satisfying the criteria of cell culture-friendly design. We explore several strategies for gradient generation and device modularity in **Chapter 2** before settling on porous membrane-based methods. In **Chapter 3**, we develop a fabrication technique for reliably bonding porous membranes with PDMS devices for cell culture conditions. Finally, in **Chapter 4** we describe the development of a modular and porous membrane-based microfluidic device that is compatible with conventional cell culture and standard 6-well plates. We ultimately demonstrate stable, quantifiable gradients, finite element modeling of porous membrane flows, and significant biological responses with cells and tissue cultures.

1.8 References

1. Weijer CJ. Collective cell migration in development. *J Cell Sci*. 2009;122(18):3215–3223.

2. Sallusto F. The role of chemokine receptors in primary, effector and memory immune response. *Exp Dermatol*. 2002;11(5):476–478.

3. Jin T, Xu X, Hereld D. Chemotaxis, chemokine receptors and human disease. *Cytokine*. 2008;44(1):1–8.

4. Wartlick O, Kicheva A, González-Gaitán M. Morphogen Gradient Formation. *Cold Spring Harb Perspect Biol*. 2009;1(3).

5. Zlotnik A, Yoshie O. Chemokines: a new classification review system and their role in immunity. *Immunity*. 2000;12:121–127.

6. Tessier-Lavigne M, Goodman CS. The Molecular Biology of Axon Guidance. *Science*. 1996;274(5290):1123–1133.

7. Song H, Poo M. The cell biology of neuronal navigation. *Nat Cell Biol*. 2001;3(3):E81–E88.

8. Dickson BJ. Molecular Mechanisms of Axon Guidance. *Science*. 2002;298(5600):1959–1964.

9. Roussos ET, Condeelis JS, Patsialou A. Chemotaxis in cancer. *Nat Rev Cancer*. 2011;11(8):573–587.

10. Godessart N, Kunkel SL. Chemokines in autoimmune disease. *Curr Opin Immunol*. 2001;13(6):670–675.

11. Gerard C, Rollins BJ. Chemokines and disease. *Nat Immunol*. 2001;2(2):108–115.

12. Goodhill GJ, Baier H. Axon guidance: stretching gradients to the limit. *Neural Comput*. 1998;10(3):521–527.

13. Levchenko A, Iglesias PA. Models of eukaryotic gradient sensing: application to chemotaxis of amoebae and neutrophils. *Biophys J*. 2002;82(1 Pt 1):50–63.

14. Imitola J, Raddassi K, Park KI, Mueller F-J, Nieto M, Teng YD, Frenkel D, Li J, Sidman RL, Walsh CA, Snyder EY, Khoury SJ. Directed migration of neural stem cells to sites of CNS injury by the stromal cell-derived factor 1α/CXC chemokine receptor 4 pathway. *Proc Natl Acad Sci*. 2004;101(52):18117 –18122.

15. Passier R, Laake LW van, Mummery CL. Stem-cell-based therapy and lessons from the heart. *Nature*. 2008;453(7193):322–329.

16. Lindvall O, Kokaia Z, Martinez-Serrano A. Stem cell therapy for human neurodegenerative disorders–how to make it work. *Nat Med*. 2004;10:S42–S50.

17. Robinton DA, Daley GQ. The promise of induced pluripotent stem cells in research and therapy. *Nature*. 2012;481(7381):295–305.

18. Restifo NP, Dudley ME, Rosenberg SA. Adoptive immunotherapy for cancer: harnessing the T cell response. *Nat Rev Immunol*. 2012;12(4):269–281.

19. Keenan TM, Folch A. Biomolecular gradients in cell culture systems. *Lab Chip*. 2008;8(1):34.

20. Bird RB, Stewart WE, Lightfoot EN. *Transport phenomena*. Wiley; 2006.

21. Makarenkova HP, Hoffman MP, Beenken A, Eliseenkova AV, Meech R, Tsau C, Patel VN, Lang RA, Mohammadi M. Differential Interactions of FGFs with Heparan Sulfate Control Gradient Formation and Branching Morphogenesis. *Sci Signal*. 2009;2(88):ra55.

22. Bökel C, Brand M. Generation and interpretation of FGF morphogen gradients in vertebrates. *Curr Opin Genet Dev*. 2013;In press.

23. Dubrulle J, Pourquié O. fgf8 mRNA decay establishes a gradient that couples axial elongation to patterning in the vertebrate embryo. *Nature*. 2004;427(6973):419–422.

24. Helm C-LE, Fleury ME, Zisch AH, Boschetti F, Swartz MA. Synergy between interstitial flow and VEGF directs capillary morphogenesis in vitro through a gradient amplification mechanism. *Proc Natl Acad Sci U S A*. 2005;102(44):15779–15784.

25. Rutkowski JM, Swartz MA. A driving force for change: interstitial flow as a morphoregulator. *Trends Cell Biol*. 2007;17(1):44–50.

26. Boyden S. The chemotactic effect of mixtures of antibody and antigen on polymorphonuclear leucocytes. *J Exp Med*. 1962;115(3):453.

27. Frevert CW, Wong VA, Goodman RB, Goodwin R, Martin TR. Rapid fluorescence-based measurement of neutrophil migration in vitro. *J Immunol Methods*. 1998;213(1):41–52.

28. Gundersen R, Barrett J. Neuronal chemotaxis: chick dorsal-root axons turn toward high concentrations of nerve growth factor. *Science*. 1979;206(4422):1079 –1080.

29. Gundersen RW, Barrett JN. Characterization of the turning response of dorsal root neurites toward nerve growth factor. *J Cell Biol*. 1980;87(3):546 –554.

30. Gerisch G, Keller H. Chemotactic reorientation of granulocytes stimulated with micropipettes containing fMet-Leu-Phe. *J Cell Sci*. 1981;52(1):1–10.

31. Ming G, Song H, Berninger B, Holt CE, Tessier-Lavigne M, Poo M. cAMP-dependent growth cone guidance by netrin-1. *Neuron*. 1997;19(6):1225–1235.

32. Song H, Ming G, Poo M. cAMP-induced switching in turning direction of nerve growth cones. *Nature*. 1997;388(6639):275–279.

33. Zigmond SH. Ability of polymorphonuclear leukocytes to orient in gradients of chemotactic factors. *J Cell Biol*. 1977;75(2):606.

34. Zicha D, Dunn GA, Brown AF. A new direct-viewing chemotaxis chamber. *J Cell Sci*. 1991;99(Pt 4):769–775.

35. Muinonen-Martin AJ, Veltman DM, Kalna G, Insall RH. An Improved Chamber for Direct Visualisation of Chemotaxis. Gullberg D, ed. *Plos One*. 2010;5(12):e15309.

36. Zengel P, Nguyen-Hoang A, Schildhammer C, Zantl R, Kahl V, Horn E. μ-Slide Chemotaxis: A new chamber for long-term chemotaxis studies. *Bmc Cell Biol*. 2011;12(1):21.

37. Nelson RD, Quie PG, Simmons RL. Chemotaxis under agarose: a new and simple method for measuring chemotaxis and spontaneous migration of human polymorphonuclear leukocytes and monocytes. *J Immunol*. 1975;115(6):1650.

38. Letourneau PC. Chemotactic response of nerve fiber elongation to nerve growth factor* 1. *Dev Biol*. 1978;66(1):183–196.

39. Brown A. Neutrophil granulocytes: adhesion and locomotion on collagen substrata and in collagen matrices. *J Cell Sci*. 1982;58(1):455–467.

40. Chen H, He Z, Bagri A, Tessier-Lavigne M. Semaphorin-neuropilin interactions underlying sympathetic axon responses to class III semaphorins. *Neuron*. 1998;21(6):1283–1290.

41. Niclou SP, Jia L, Raper JA. Slit2 is a repellent for retinal ganglion cell axons. *J Neurosci*. 2000;20(13):4962.

42. Heit B, Tavener S, Raharjo E, Kubes P. An intracellular signaling hierarchy determines direction of migration in opposing chemotactic gradients. *J Cell Biol*. 2002;159(1):91.

43. Pujic Z, Giacomantonio CE, Unni D, Rosoff WJ, Goodhill GJ. Analysis of the growth cone turning assay for studying axon guidance. *J Neurosci Methods*. 2008;170(2):220–228.

44. Wang Y, Irvine DJ. Convolution of chemoattractant secretion rate, source density, and receptor desensitization direct diverse migration patterns in leukocytes. *Integr Biol*. 2013;5(3):481–494.

45. Kim S, Kim HJ, Jeon NL. Biological applications of microfluidic gradient devices. *Integr Biol*. 2010;2(11-12):584.

46. Wu J, Wu X, Lin F. Recent developments in microfluidics-based chemotaxis studies. *Lab Chip*. 2013;13(13):2484–2499.

47. Dertinger SKW, Chiu DT, Jeon NL, Whitesides GM. Generation of gradients having complex shapes using microfluidic networks. *Anal Chem*. 2001;73(6):1240–1246.

48. Irimia D, Geba DA, Toner M. Universal microfluidic gradient generator. *Anal Chem*. 2006;78(10):3472–3477.

49. Campbell K, Groisman A. Generation of complex concentration profiles in microchannels in a logarithmically small number of steps. *Lab Chip*. 2007;7(2):264–272.

50. Jeon NL, Baskaran H, Dertinger SKW, Whitesides GM, Van de Water L, Toner M. Neutrophil chemotaxis in linear and complex gradients of interleukin-8 formed in a microfabricated device. *Nat Biotechnol*. 2002;20(8):826–830.

51. Lin F, Nguyen CM-C, Wang S-J, Saadi W, Gross SP, Jeon NL. Neutrophil migration in opposing chemoattractant gradients using microfluidic chemotaxis devices. *Ann Biomed Eng*. 2005;33(4):475–482.

52. Chung BG, Flanagan LA, Rhee SW, Schwartz PH, Lee AP, Monuki ES, Jeon NL. Human neural stem cell growth and differentiation in a gradient-generating microfluidic device. *Lab Chip*. 2005;5(4):401–6.

53. Saadi W, Wang SJ, Lin F, Jeon NL. A parallel-gradient microfluidic chamber for quantitative analysis of breast cancer cell chemotaxis. *Biomed Microdevices*. 2006;8(2):109–118.

54. Walker GM, Sai J, Richmond A, Stremler M, Chung CY, Wikswo JP. Effects of flow and diffusion on chemotaxis studies in a microfabricated gradient generator. *Lab Chip*. 2005;5(6):611–618.

55. Joanne Wang C, Li X, Lin B, Shim S, Ming G, Levchenko A. A microfluidics-based turning assay reveals complex growth cone responses to integrated gradients of substrate-bound ECM molecules and diffusible guidance cues. *Lab Chip*. 2008;8(2):227.

56. Young EWK, Beebe DJ. Fundamentals of microfluidic cell culture in controlled microenvironments. *Chem Soc Rev*. 2010;39(3):1036–1048.

57. Yew AG, Pinero D, Hsieh AH, Atencia J. Low Peclet number mass and momentum transport in microcavities. *Appl Phys Lett*. 2013;102(8):084108–084108–4.

58. Diao J, Young L, Kim S, Fogarty EA, Heilman SM, Zhou P, Shuler ML, Wu M, DeLisa MP. A three-channel microfluidic device for generating static linear gradients and its application to the quantitative analysis of bacterial chemotaxis. *Lab Chip*. 2006;6(3):381.

59. Saadi W, Rhee SW, Lin F, Vahidi B, Chung BG, Jeon NL. Generation of stable concentration gradients in 2D and 3D environments using a microfluidic ladder chamber. *Biomed Microdevices*. 2007;9(5):627–635.

60. Shamloo A, Ma N, Poo M, Sohn LL, Heilshorn SC. Endothelial cell polarization and chemotaxis in a microfluidic device. *Lab Chip*. 2008;8(8):1292.

61. Wu H, Huang B, Zare RN. Generation of complex, static solution gradients in microfluidic channels. *J Am Chem Soc*. 2006;128(13):4194–4195.

62. Cheng S-Y, Heilman S, Wasserman M, Archer S, Shuler ML, Wu M. A hydrogel-based microfluidic device for the studies of directed cell migration. *Lab Chip*. 2007;7(6):763.

63. Mosadegh B, Huang C, Park JW, Shin HS, Chung BG, Hwang S-K, Lee K-H, Kim HJ, Brody J, Jeon NL. Generation of Stable Complex Gradients Across Two-Dimensional Surfaces and Three-Dimensional Gels. *Langmuir*. 2007;23(22):10910–10912.

64. Barkefors I, Thorslund S, Nikolajeff F, Kreuger J. A fluidic device to study directional angiogenesis in complex tissue and organ culture models. *Lab Chip*. 2009;9(4):529.

65. Ahmed T, Shimizu TS, Stocker R. Bacterial Chemotaxis in Linear and Nonlinear Steady Microfluidic Gradients. *Nano Lett*. 2010;10(9):3379–3385.

66. Atencia J, Morrow J, Locascio LE. The microfluidic palette: A diffusive gradient generator with spatio-temporal control. *Lab Chip*. 2009;9(18):2707.

67. Atencia J, Cooksey GA, Locascio LE. A robust diffusion-based gradient generator for dynamic cell assays. *Lab Chip*. 2011;12(2):309–316.

68. Tong Z, Balzer EM, Dallas MR, Hung W-C, Stebe KJ, Konstantopoulos K. Chemotaxis of Cell Populations through Confined Spaces at Single-Cell Resolution. *Plos One*. 2012;7(1):e29211.

69. Balzer EM, Tong Z, Paul CD, Hung W-C, Stroka KM, Boggs AE, Martin SS, Konstantopoulos K. Physical confinement alters tumor cell adhesion and migration phenotypes. *Faseb J*. 2012;26(10):4045–4056.

70. Irimia D, Charras G, Agrawal N, Mitchison T, Toner M. Polar stimulation and constrained cell migration in microfluidic channels. *Lab Chip*. 2007;7(12):1783.

71. Irimia D, Toner M. Spontaneous migration of cancer cells under conditions of mechanical confinement. *Integr Biol*. 2009;1(8-9):506–512.

72. Ambravaneswaran V, Wong IY, Aranyosi AJ, Toner M, Irimia D. Directional decisions during neutrophil chemotaxis inside bifurcating channels. *Integr Biol*. 2010;2(11-12):639.

73. Butler KL, Ambravaneswaran V, Agrawal N, Bilodeau M, Toner M, Tompkins RG, Fagan S, Irimia D. Burn Injury Reduces Neutrophil Directional Migration Speed in Microfluidic Devices. *Plos One*. 2010;5(7):e11921.

74. Keenan TM, Hsu C-H, Folch A. Microfluidic "jets" for generating steady-state gradients of soluble molecules on open surfaces. *Appl Phys Lett*. 2006;89(11):114103.

75. Bhattacharjee N, Li N, Keenan TM, Folch A. A neuron-benign microfluidic gradient generator for studying the response of mammalian neurons towards axon guidance factors. *Integr Biol*. 2010;2(11-12):669.

76. Abhyankar VV, Lokuta MA, Huttenlocher A, Beebe DJ. Characterization of a membrane-based gradient generator for use in cell-signaling studies. *Lab Chip*. 2006;6(3):389.

77. Kim T, Pinelis M, Maharbiz MM. Generating steep, shear-free gradients of small molecules for cell culture. *Biomed Microdevices*. 2008;11(1):65–73.

78. Mosadegh B, Agarwal M, Tavana H, Bersano-Begey T, Torisawa Y, Morell M, Wyatt MJ, O'Shea KS, Barald KF, Takayama S. Uniform cell seeding and generation of overlapping gradient profiles in a multiplexed microchamber device with normally-closed valves. *Lab Chip*. 2010;10(21):2959.

79. VanDersarl JJ, Xu AM, Melosh NA. Rapid spatial and temporal controlled signal delivery over large cell culture areas. *Lab Chip*. 2011;11(18):3057.

80. Kawada J, Kimura H, Akutsu H, Sakai Y, Fujii T. Spatiotemporally controlled delivery of soluble factors for stem cell differentiation. *Lab Chip*. 2012;12(21):4508–4515.

81. Morel M, Galas J-C, Dahan M, Studer V. Concentration landscape generators for shear free dynamic chemical stimulation. *Lab Chip*. 2012;12(7):1340.

82. Kim C, Kreppenhofer K, Kashef J, Gradl D, Herrmann D, Schneider M, Ahrens R, Guber A, Wedlich D. Diffusion- and convection-based activation of Wnt/β-catenin signaling in a gradient generating microfluidic chip. *Lab Chip*. 2012;12(24):5186–5194.

83. Zengel P, Nguyen-Hoang A, Schildhammer C, Zantl R, Kahl V, Horn E. μ-Slide Chemotaxis: A new chamber for long-term chemotaxis studies. *Bmc Cell Biol*. 2011;12:21.

84. Taylor AM, Rhee SW, Tu CH, Cribbs DH, Cotman CW, Jeon NL. Microfluidic Multicompartment Device for Neuroscience Research. *Langmuir*. 2003;19(5):1551–1556.

85. Taylor AM, Blurton-Jones M, Rhee SW, Cribbs DH, Cotman CW, Jeon NL. A microfluidic culture platform for CNS axonal injury, regeneration and transport. *Nat Methods*. 2005;2(8):599–605.

86. Taylor AM, Berchtold NC, Perreau VM, Tu CH, Li Jeon N, Cotman CW. Axonal mRNA in uninjured and regenerating cortical mammalian axons. *J Neurosci*. 2009;29(15):4697.

87. Taylor AM, Dieterich DC, Ito HT, Kim SA, Schuman EM. Microfluidic Local Perfusion Chambers for the Visualization and Manipulation of Synapses. *Neuron*. 2010;66(1):57–68.

88. Hallfors N, Khan A, Dickey MD, Taylor AM. Integration of pre-aligned liquid metal electrodes for neural stimulation within a user-friendly microfluidic platform. *Lab Chip*. 2013;13(4):522–526.

89. Lee PJ, Hung PJ, Rao VM, Lee LP. Nanoliter scale microbioreactor array for quantitative cell biology. *Biotechnol Bioeng*. 2006;94(1):5–14.

90. Lee PJ, Ghorashian N, Gaige TA, Hung PJ. Microfluidic System for Automated Cell-based Assays. *Jala Charlottesv Va*. 2007;12(6):363–367.

91. Lee PJ, Hung PJ, Lee LP. An artificial liver sinusoid with a microfluidic endothelial-like barrier for primary hepatocyte culture. *Biotechnol Bioeng*. 2007;97(5):1340–1346.

92. Lee PJ, Helman NC, Lim WA, Hung PJ. A microfluidic system for dynamic yeast cell imaging. *BioTechniques*. 2008;44(1):91–95.

93. Lee PJ, Gaige TA, Hung PJ. Dynamic cell culture: a microfluidic function generator for live cell microscopy. *Lab Chip*. 2009;9(1):164–166.

94. Meyvantsson I, Vu E, Lamers C, Echeverria D, Worzella T, Echeverria V, Skoien A, Hayes S. Image-based analysis of primary human neutrophil chemotaxis in an automated direct-viewing assay. *J Immunol Methods*. 2011;374(1-2):70–77.

95. Barkefors I, Le Jan S, Jakobsson L, Hejll E, Carlson G, Johansson H, Jarvius J, Park JW, Li Jeon N, Kreuger J. Endothelial cell migration in stable gradients of vascular endothelial growth factor A and fibroblast growth factor 2: effects on chemotaxis and chemokinesis. *J Biol Chem*. 2008;283(20):13905–13912.

96. Thorslund S, Nguyen H, Läräng T, Barkefors I, Kreuger J. A disposable and multifunctional capsule for easy operation of microfluidic elastomer systems. *J Micromechanics Microengineering*. 2011;21(12):127001.

Chapter 2: Modular Microfluidic Design and Gradient Generation

2.1 Introduction

Well-characterized, stable, and reproducible generation of biochemical gradients is critical for the in vitro study of gradient sensing biology. A large variety of microfluidic devices offer this capability, yet there remain technical limitations and practical differences between common designs and conventional cell culture techniques. Despite the advantages of microfluidic technique, challenges with device operation and cell culture has impeded their widespread adoption into biology-centered laboratories. Limitations of interfacing with cell culture, shear stress from fluid flow, and difficulty with long-term maintenance of cell cultures are primary sources of concern. The ongoing challenge is to develop microfluidic platforms that provide a suitably benign and physiologically relevant environment for cell culture in a user-friendly format. Researchers have more recently utilized modularity, open-surface cell culture designs, and porous membranes in an effort to make devices more accessible. In this chapter, we present chronologically the development of several methods and devices for applying gradients to cell cultures:

1. An automated microfluidic device for controlling perfusion and gradients
2. A method for modular interfacing devices with cell culture modules
3. A modular gradient device for low-shear cell culture
4. A modular device for automated focal stimulation
5. A open cell culture device using porous membranes to generate gradients

2.2 A Multi-Purpose Microfluidic Perfusion System with Combinatorial Choice of Inputs, Mixtures, Gradient Patterns, and Flow Rates

This section is a brief summary of the paper:

Cooksey, Gregory A., Christopher G. Sip, and Albert Folch. "A Multi-purpose Microfluidic Perfusion System with Combinatorial Choice of Inputs, Mixtures, Gradient Patterns, and Flow Rates." *Lab on a Chip* 9, no. 3 (2009): 417.

In this paper we report an integrated microfluidic device for the automated control of perfusion for cell culture applications. On-chip elastomeric microvalves are used to selectively open or close microchannels through pneumatic actuation as shown in **Figure 2.1(a-b)**). Sets of microvalves are used to control perfusion conditions through the selection of chemicals, mixtures, gradients, and flow rate. Driving of the pneumatic valve pressure for the multiplexer, mixer, flow bypasses, and flow resistors (**Figure 2.1(c-d)**) is accomplished by computer controlled LabView program and a rack of solenoid switches. A multi-channel design enables the simultaneous rinsing of virtually all of the dead volume within the device to eliminate cross-contamination between sequentially perfused chemicals (**Figure 2.2(e)**). For demonstrative purposes, colored dyes were used to simulate different chemicals as shown in **Figure 2.2(f)**.

A critical element is the incorporation of 8-valve microfluidic multiplexer that is used to encode the selection of one of 16 inlets or one of 64 possible combinations that are delivered to a central flow chamber (**Figure 2.3**). In our design we have cut the number of off-chip connections in half through the use of the multiplexer design. Importantly, the multiplexer design offers increasing returns on scalability as the number of inlets increases (e.g. for 32 inlets only 10 microvalves are required). For example, in a seminal paper, Thorsen et al.[1] demonstrated that only 20 pneumatic control channels are required to specifically address 1024 flow channels. Additional microvalves are integrated to control the flow patterns, mixing, and flow rates as shown in **Figure 2.3**.

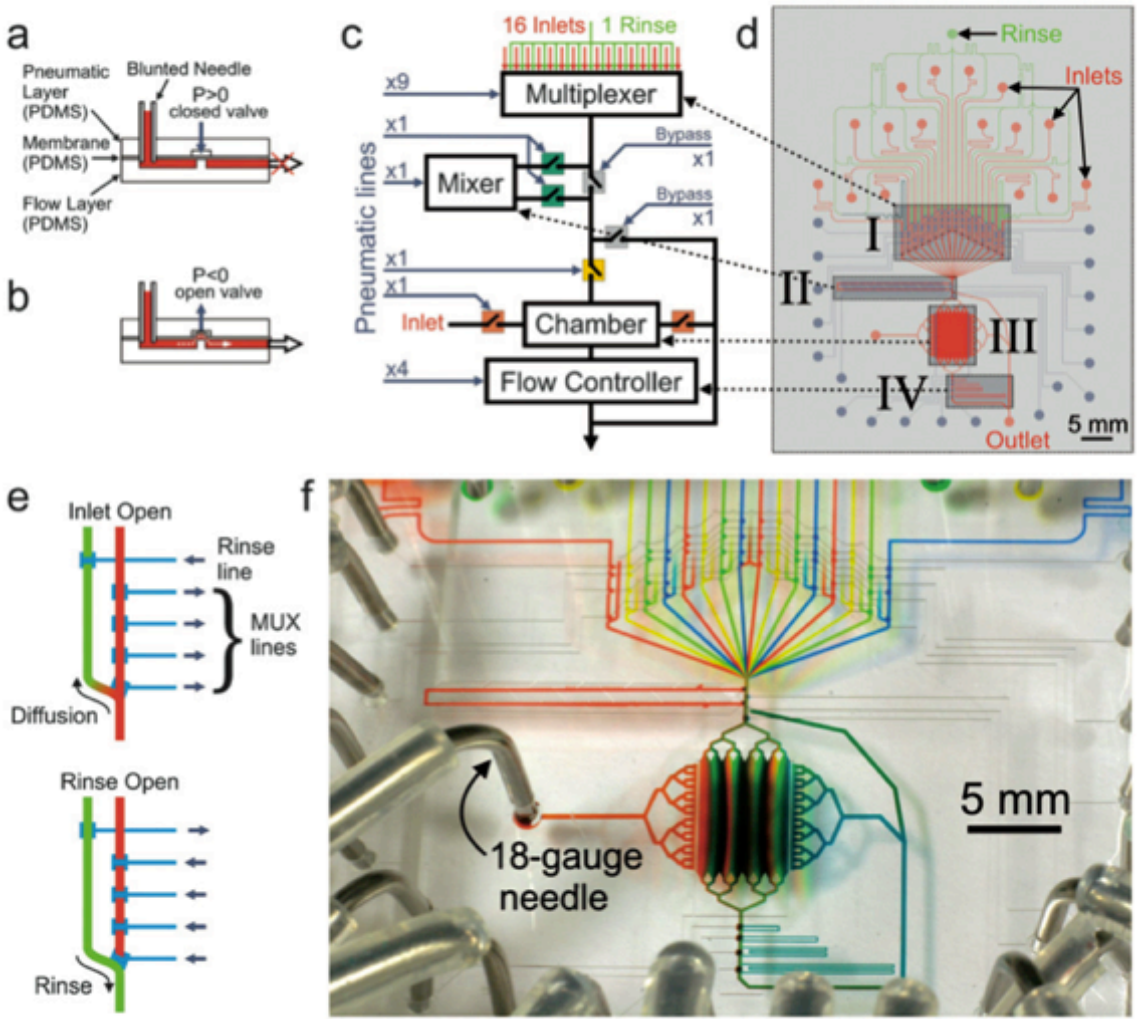

Figure 2.1: Overview of multi-purpose perfusion device design. (a-b) A cross-sectional schematic depicts the operation of normally closed microvalves through pneumatic operation. (c) A block diagram showing the major device components with the number of pneumatic valve lines. A multiplexer controls the selection of inlets through the activation of a subset of any 4 valves while the multi-rinse is controlled by an additional valve. Additional valves control the operation of the mixer, bypasses, side flows through the chamber, and the flow controller. (d) A schematic overview of the device layout indicates the multiplexer (I), mixer (II), chamber (III), and flow controller (IV). (e) The selection of an inlet requires 4 valves to be open simultaneously. The design of the multi-rinse channel network enables complete removal of solutions without dead volume. (f) A photograph of the device loaded with colored dyes and operated with all the inlets open and flowing through the central chamber. The 18-gauge needles that serve as off-chip connections to the valve and fluid inputs are shown.

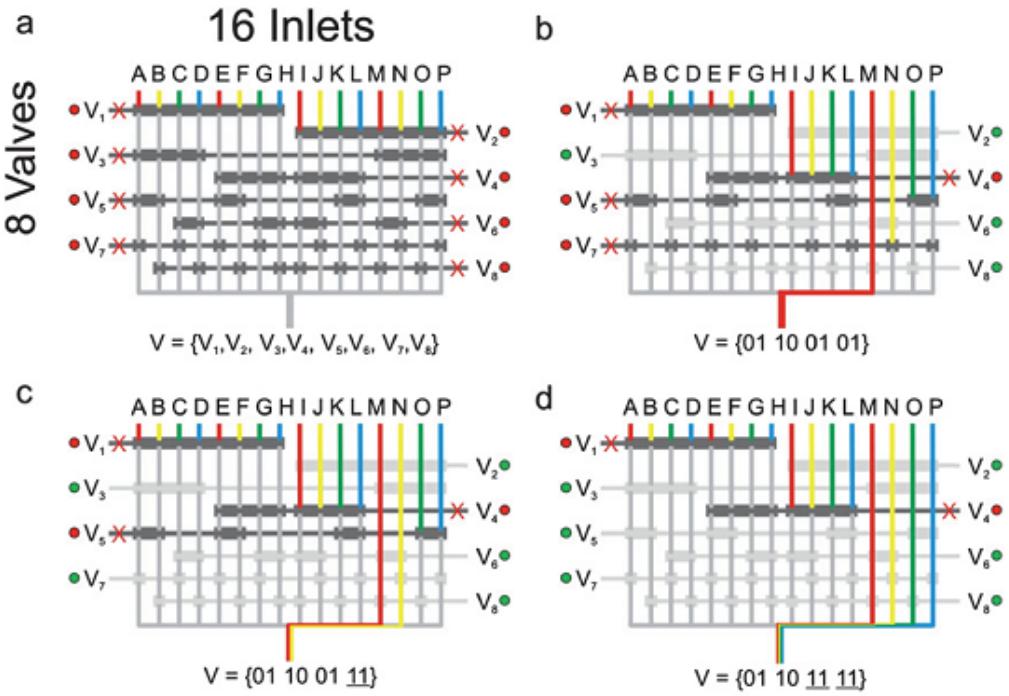

Figure 2.2: Operation of the multiplexer for selection of individual inlets. (a) Each pair of valves (e.g. V1 and V2) controls selection for half of the individual inlets. (b) The inlet M is selected by the operation of the valve combination V2-V3-V6-V8 or {01 10 01 01}. Any combination of valve pairs set to zero (e.g. {01 00 01 01} or {01 01 00 10}) will result in all inlets being closed. When a pair of valves are both open, inlet combinations can be selected such as for (c) 2 inlets with the sequence {01 10 01 11} or (d) 4 inlets with the sequence {01 10 11 11}.

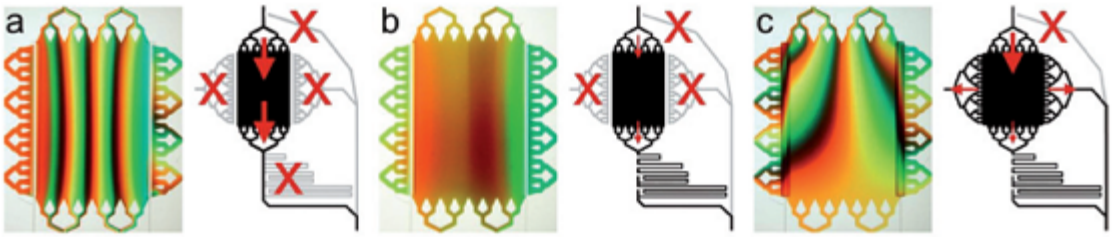

Figure 2.3: Control of gradient flow patterns in the central chamber. (a) A gradient generated with the side valves and the flow resistor deactivated at a flow rate of 44 μL min^{-1}. (b) With all elements of the flow resistor activated, the flow is reduced to 4 μL min^{-1} resulting in more diffusive mixing between inlets. (c) Operation of side valves can be used to redirect streams within the central chamber.

The perfusion system described in the paper offers great opportunities for spatiotemporally modulating the biochemical microenvironment of cells in culture (e.g. gradients over a large population of cells) and for analyzing cell behavior in well-defined conditions (medium compositions, flow shear, etc.). We have demonstrated several microfluidic tools integrated into a single perfusion system that have wide applicability in the automation of multi-parameter cell culture experiments. Combinatorial mixing strategies could benefit high-throughput studies needed in toxicology or drug development, where real-time assays of competition or synergy between multiple compounds could be easily automated. The switchable, discrete flow resistor design provides a robust method to control fluid flow (and thus, the shear forces exerted over the cells) over a wide range of flow rates using only a small number of channels. Last but not least, we have demonstrated complex, dynamic gradients not achievable before by combining inlets, controlling mixing, and regulating flow rate using variable flow resistances in the flow path.

2.3 Modular Microfluidic Systems Using Reversibly Attached PDMS Fluid Control Modules

This section is a brief summary of the paper:

Skafte-Pedersen, Peder, Christopher G. Sip, Albert Folch, and Martin Dufva. "Modular Microfluidic Systems Using Reversibly Attached PDMS Fluid Control Modules." *Journal of Micromechanics and Microengineering* 23, no. 5 (May 1, 2013): 055011. doi:10.1088/0960-1317/23/5/055011.

PDMS soft lithography with integrated elastomeric valves is the most prevalent approach for implementing fluid automation in microfluidic devices. These systems facilitate multiplexed flow control and throughput through means of large-scale integration[1]. However, a consequence of such integration is reduced flexibility in designs, materials, and increased cost per device. For cell culture applications special considerations for substrate preparation, cell seeding, and long-term maintenance

complicate the matter such that biologists still favor alternative materials such as polystyrene[2]. An alternative is the use of modularity to separate the fluid automation and cell culture components of a system. In this paper, we describe a method for fabricating PDMS modules with integrated valves and self-aligning O-rings that enable reversible coupling to poly(methyl methacrylate) (PMMA) devices. To interface the modules, 4 screws are simply hand tightened in a clamping apparatus. The apparatus is portable to facilitate cell culture for which transfer of samples between workstations such as laminar flow hoods, incubators and microscopes is routine. Furthermore, PMMA modules can be interchanged to provide flexibility for experimental design and facilitate cell culture.

2.3.1 A self-aligning modular system for fluid automation

For designs in which the fluid handling can be isolated from the cell culture components, modularity can improve experimental throughput and practical use. However, in order to create modular systems it is important to be able to interface the different components in an easy and reliable manner. To address this issue, we present a modular system featuring a universal soft lithography-based PDMS fluidic control module that feeds an externally attached hard passive polymeric chip (**Figure 2.4(a-b)**). The system is based on a reversible sealing between the PDMS fluid control module and the passive chip using self-aligning PDMS O-ring features (**Figure 2.4(c)**).

To demonstrate the concept, we have fabricated a PDMS fluid control module featuring pneumatically actuated valves leading to 32 central chip connections. The fabrication involves multi-layer soft lithography to embed elastomeric membranes and O-ring features in a double-sided molding process as described in **Figure 2.5**. By tightening four screws, the 32 fluidic chip-to-control module interconnections can be readily formed as shown in the schematic in **Figure 2.6**. Modularity enables interfacing of the PDMS control module with different cell culture modules as shown in **Figure 2.7**.

Finally, we demonstrate that control of microfluidic perfusion and gradient generation can be accomplished with the modular strategy (**Figure 2.8**).

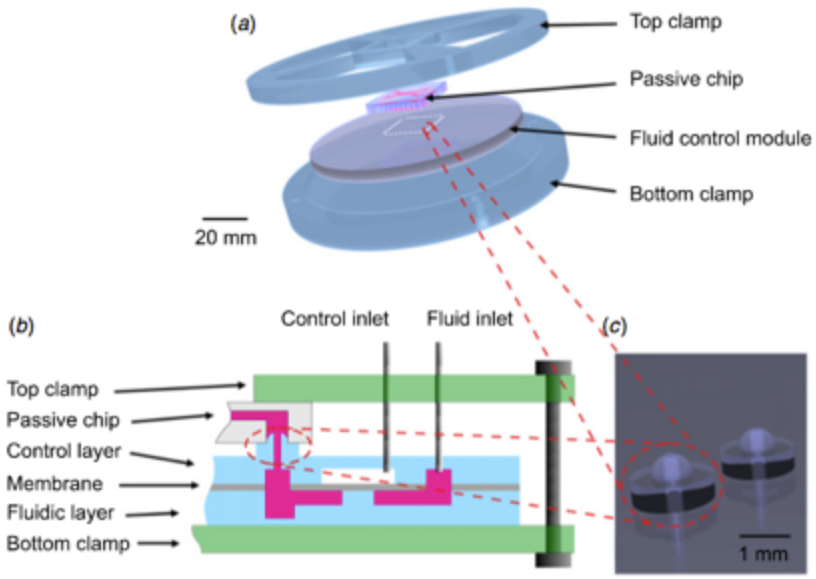

Figure 2.4: Overview of the modular microfluidic system. (a) An exploded perspective showing arrangement of the top clamp, passive PMMA chip, PDMS fluid control module, and bottom clamp. (b) A cross-sectional schematic shows the arrangement of layers for the assembled apparatus. Elastomeric microvalves are integrated into the PDMS fluid control module using multi-layer soft-lithography. Off-chip connections to fluid reservoirs and pneumatic inputs are made through standard needles press-fitted into the PDMS module. Self-aligning O-ring features embedded in the PDMS surface accomplish fluid connections to the PMMA module. Fluidic channel depth directly under the O-rings is increased to avoid pinching off channels upon compression. (c) A close-up image of two O-ring structures shows the O-ring on the topside of the fluid control module and through-hole leading to fluidic channels in the fluid control module.

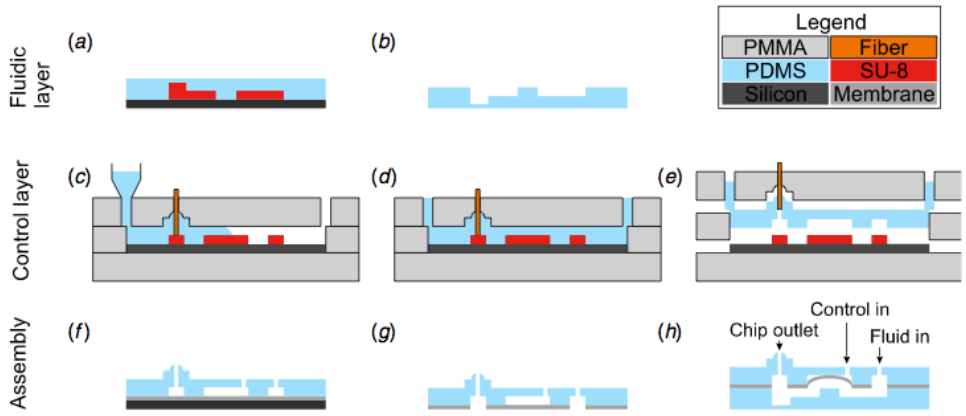

Figure 2.5: Soft-lithography fabrication of the PDMS control module. (a-b) Standard replica molding is used to produce the fluidic layer. (c-e) Control layers are produced using double sided injection molding. Fibers are manually placed at the location of O-ring features to produce through holes after de-molding. (f-h) The device is assembled using oxygen plasma to bond a spin-coated PDMS membrane and the fluid layer. Valves are actuated to prevent sticking of the membrane to the valve seats after plasma bonding.

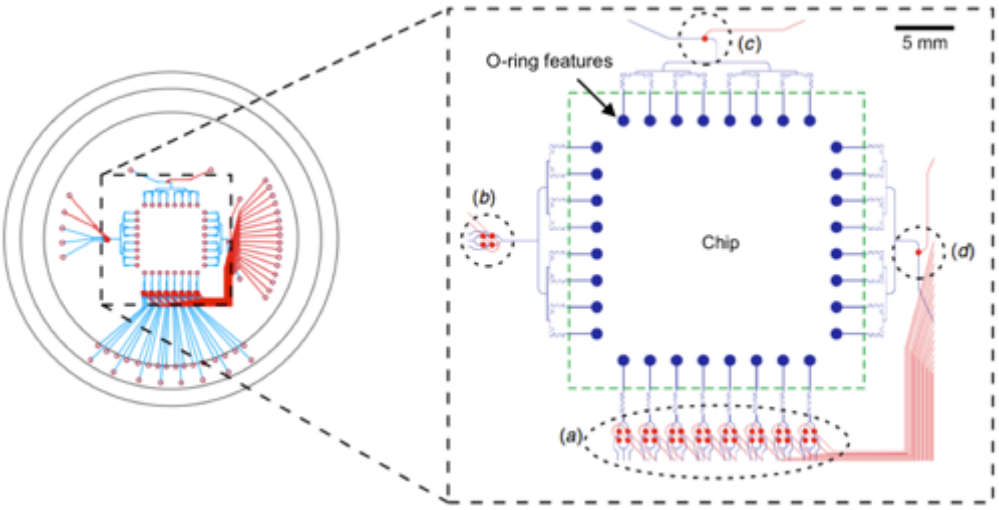

Figure 2.6: PDMS fluid control module layout. On the left an overview of the entire device with the locations of inlet, outlets, and valve control ports on the periphery. Flow channels are in shown in blue and valve control channels are shown in red. Flow to the chip is controlled by (a) 8 valve pairs for bottom inlets, (b) one valve pair for side inlets, and (c) and (d) single valves for controlling outlet direction. During assembly the PMMA chip is placed in the area designated by the dotted green box and interconnections are made with the fluid channels by the 32 O-ring features (blue circles).

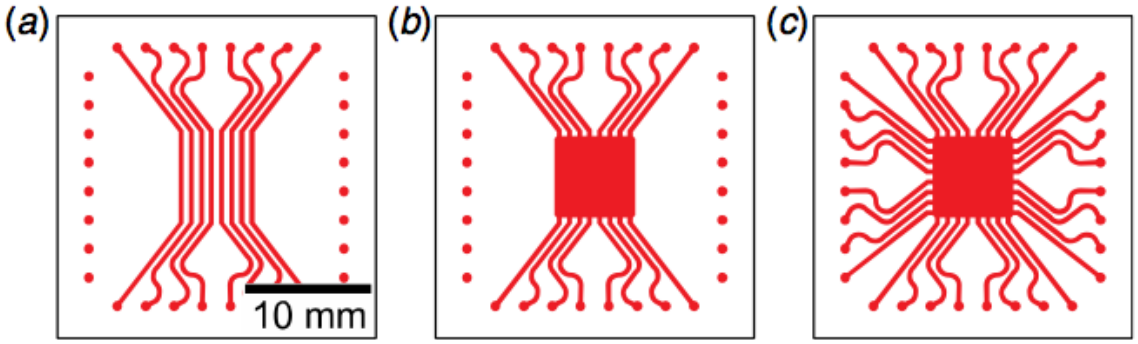

Figure 2.7: Examples of different designs for cell culture modules. (a) An array of individual channels and (b-c) different chamber designs.

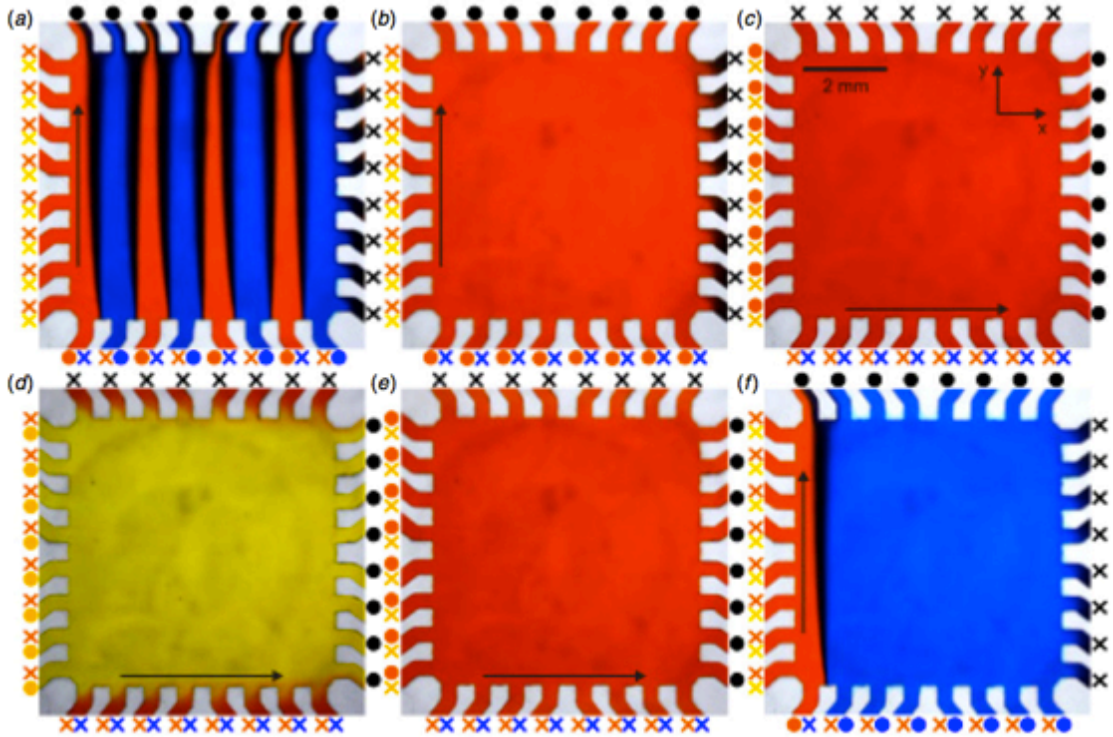

Figure 2.8: Demonstration of automated fluid handling in a PMMA chip used colored dyes. A PDMS flow control module (not shown) controls directionality and choice of inputs through integrated microvalves. Symbols on the periphery of each panel represent the state of valves controlling flow through the entrance or exit microchannels. (a) Flow enters from the bottom in an alternating configuration. (b) A uniform exposure. (c-e) A series of alternating wash steps. (f) A heterogeneous flow pattern.

2.3.2 Summary and assessment of the method

Microfluidics is developing to be a rich alternative to conventional high content screening methods predominantly used for drug discovery because it offers enhanced flow control, control of stimulus applied to cells, and benefits from automation, integration, and scaling[3]. With growing interest in using thermoset materials for microfluidic cell culture devices[2,4,5], a modular strategy for microfluidic automation is beneficial to device development. Designs such as ours presented here, offer the capability to study a large number of cell culture conditions through automation of perfusion and generation of gradients. The modular format enables interfacing of different modules and portability to facilitate cell culture**.** This could be useful for studies that require a large number of cell culture conditions for screening applications[6]. For example, one can envision extending this design to interface with arrays of individually addressable cell culture channels similar to the format developed by Beebe et al.[7,8]. Many designs utilize manual or robotic fluid handling to interface with arrayed microchannels for high content screening[8–12]. One could argue that manual pipetting is sufficient for testing a reasonable number of conditions such as with a 96-well plate; however, if control of variable timing is desired, a degree of automation is necessary. To study their effects on cell differentiation, the sequence, timing, and concentrations of factors could be varied more easily using a system of automated fluid handling like ours. Future studies could benefit from our modular design to achieve flexible and cheap automation for arrayed cell cultures and microfluidic high content screening.

2.4 A Modular Cell Culture Device for Generating Arrays of Gradients Using Stacked Microfluidic Flows

The content of this section has been published in the following paper:

Sip, Christopher G., Nirveek Bhattacharjee, and Albert Folch. "A Modular Cell Culture Device for Generating Arrays of Gradients Using Stacked Microfluidic Flows." *Biomicrofluidics* 5, no. 2 (June 2011)

In this paper, we describe a modular microfluidic gradient generator that can be reversibly sealed onto pre-existing cell cultures. The device utilizes a vacuum sealing strategy for reversible application to pre-established cell cultures. The device features extremely low shear forces, tunable large-area gradients, and simple interfacing with cultures. We apply this device to an existing culture of breast cancer cells to demonstrate the negligible effect of its shear flow on migratory behavior. Lastly, we extend the stacked-flow design to demonstrate a scalable architecture with a device for generating an array of combinatorial gradients.

An effective solution to produce modular microfluidic devices has been to implement reversible sealing techniques such as clamping[13,14] or vacuum sealing[15–18] which simplify integration of cell cultures with "add-on" microfluidic devices. None of the previously presented devices has an architecture that is amenable to combinatorial testing of gradients, which would be beneficial in screening for subtle or bimodal cell behaviors. For our device, gradient generation is based on the principle of stacked laminar flows to produce stable gradients of diffusible molecules over a 4 mm^2 area for long-term with negligible shear forces (~6×10^{-3} dyn/cm^2) (see **Figure 2.9**). We integrate a vacuum sealing feature for reversible application of the device to pre-established cell cultures, so cells do not need to be introduced into the device through a dedicated inlet. We demonstrate the long-term stability and dynamic tunability of gradients produced using the stacked-flow device. We also show that the application of this device to pre-existing cultures of breast cancer cells is straightforward. Furthermore, our microfluidic

architecture is designed for generating arrays of combinatorial gradients, which we demonstrate as a proof of concept.

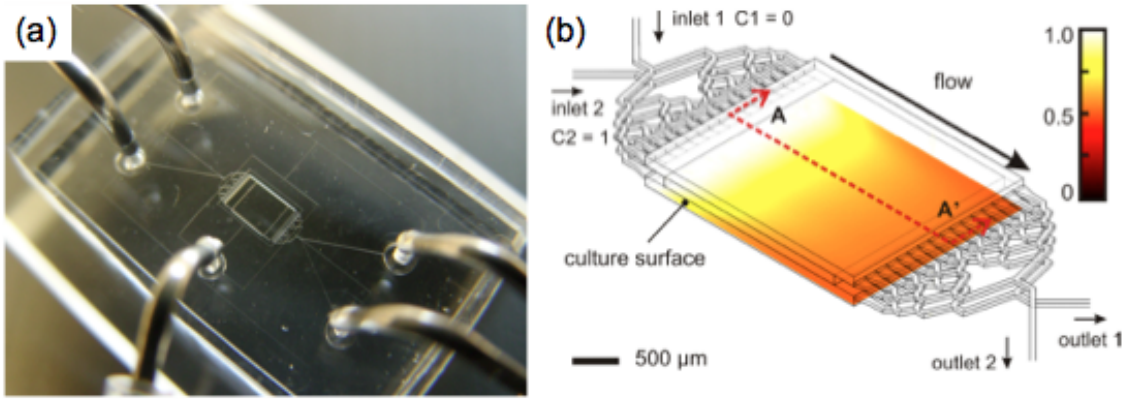

Figure 2.9: The stacked flow device and gradient simulation. (a) A photograph of the device with connections for the pair of inlets, outlets, and the vacuum-sealing network inserted. (b) An isometric 3D finite-element model of the flows through the stacked flow device. A 2D cross-sectional model is shown for the cross section along the line A-A' in (c). A 2D model is shown here with a representative gradient generated from diffusive mixing of the stacked laminar flows. The model shown here is solved with fluorescein as the diffusing species (MW: 332.31 and D ~ 6.4×10^{-6} cm^2/s) delivered via the bottom inlet. The shear stress predicted for 10 µm above the surface is ~6×10^{-3} dyn/cm^2, two orders of magnitude below the threshold for inducing neutrophil migration bias (~0.7 dyn/cm^2)[19].

2.4.1 Methods and results

Fabrication of the stacked flow device

SU-8 2000 series photoresists were obtained from MicroChem (Newton, MA). Dow Corning Sylgard 184 PDMS was purchased from KR Anderson, Inc. (Kent, WA). Fluorosilane [(Tridecafluoro-1, 1, 2, 2, tetrahydrooctyl)-1 trichlorosilane] was obtained from United Chemical Technologies Inc. (Horsham, PA). Orange-G dye, fluorescein sodium salt, bovine serum albumin (BSA), poly-D-lysine, and Collagen type IV were purchased from Sigma-Aldrich (St. Louis, MO). RPMI 1640 medium was obtained from Invitrogen (Carlsbad, CA). MDA-MB-231 breast cancer cells were obtained from

American Type Cell Culture Collection (Manassas, VA). Polyester liner sheets (Scotchpacktm 9744 Release Liner) were generously donated by 3M (St. Paul, MN). 3-aminopropyltriemethoxysilane (APTES) and 3-Glycidyloxypropyl-trimethoxysilane (GPTMS) were purchased from Sigma-Aldrich.

Fabrication of the vacuum sealing stacked-flow device follows the principles of soft-lithography and the layer-by-layer assembly scheme outlined in **Figure 2.10 (a-h).** Fabrication of the device begins with the preparation of a set of three multilayer SU-8 patterned master molds using two-step photolithography. Each device is assembled from replicas of these molds produced in poly(dimethylsiloxane) (PDMS). The top flow layer is defined by casting a thick replica with PDMS several millimeters thick. The bottom flow and vacuum sealing layers were each produced by "exclusion molding" PDMS between the masters and a polyester liner sheet by applying force with a clamp[18]. The tallest SU-8 features exclude PDMS completely from the liner sheets thereby resulting in perforated and patterned membranes. Inlets, outlets, and vacuum ports are cored into the top flow layer using a biopsy punch (Harris Uni-core, Ted-Pella, Redding, CA). Each layer is aligned and bonded in two subsequent plasma oxidation steps to complete the device.

To produce arrays of stacked-flow gradient generators, we used a similar fabrication scheme with a few exceptions. Instead of vacuum sealing, this particular device was produced with enclosed channels for the purpose of demonstrating the 3-D microfluidic plumbing and the generation of multiple combinatorial gradients. For this device, the layers were bonded using a room temperature chemical bonding technique involving amino-epoxy reactive chemistry[20,21]. To functionalize the PDMS surfaces with either amino- or epoxy- reactive groups, plasma oxidized layers were immersed for 20 min in solutions of either 1% APTES in water or 1% GPTMS in ethanol respectively.

Complementary pairs of treated PDMS layers were then rinsed with distilled water, air dried, and brought into conformal contact to achieve bonding after several hours at room temperature. This method enables careful alignment and construction of large multilayer devices because the bonding is not instantaneous like with pure oxidative plasma bonding technique.

Stacked flow device operation

The vacuum sealing feature of the device enables the straightforward preparation of substrates and cell seeding as shown in **Figure 2.10(i)**. The device contains a rectangular open chamber 300 μm-deep and 4 mm^2 in area that interfaces directly with cell culture substrates through vacuum sealing as shown in **Figure 2.10(j)**. By reversible application of the device, we can introduce soluble gradients at any time point to pre-established cell cultures given a flat substrate suitable for sealing. During operation of the device, as shown in **Figure 2.10(k)**, two stacked-flows are generated in the square cell culture chamber with each flow serving as a source or a sink for a soluble factor. A concentration gradient is formed simply by diffusion between the laminar streams as they flow through the chamber and towards the outlets. This produces a steady-state and large-area concentration gradient at the cell substrate surface. In essence, the gradient generator's primary feature is the reliance on the slow diffusive broadening (in the direction orthogonal to the surface) of the concentration boundary formed by the two adjacent streams. Incidentally, diffusive broadening is a significant limiting factor for typical laminar flow based designs of the style demonstrated by Dertinger et al.[22]

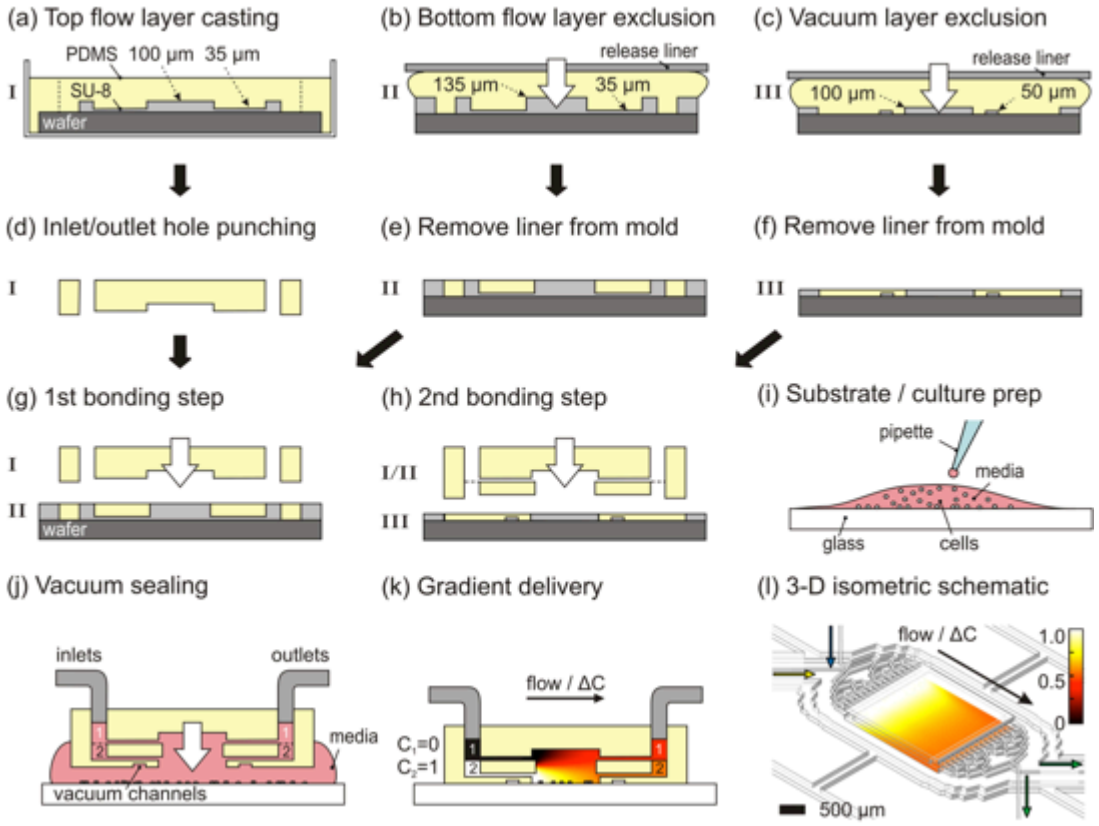

Figure 2.10: Schematic illustration of fabrication process and operation of the vacuum-sealing stacked-flow gradient device. (a) For the top flow layer a thick replica mold is cast by curing PDMS over a multi-layer SU-8 patterned mold. [(b)–(c)] The bottom flow and vacuum layers are exclusion-molded by clamping PDMS between a patterned wafer and a polyester liner. The tallest SU-8 features exclude PDMS completely from the layer resulting in a perforated and patterned membrane. (d) Inlets are bored in the top flow layer for fluidic access. [(e)-(f)] The liners are removed from the molds to expose the top side of the PDMS membranes. [(g)–(h)] Layer-by-layer bonding is achieved with two plasma oxidation steps. (i) Substrates are prepared on glass for cell seeding and culture prior to application of the device. (j) Integrated vacuum sealing channels enable the wet application of the device to an established cell culture. (k) Stacked-flow is delivered to generate a gradient at the cell culture surface. (l) A 3-D isometric schematic shows the structure of the device with a simulated gradient for fluorescein (MW: 332.31 and diffusivity D ~ 6.4×10-6 cm2/s) superimposed at the cell culture surface.

Finite-element modeling of stacked flows

We used finite-element modeling (FEM) software (COMSOL Multiphysics 3.3, COMSOL Inc., Burlington, MA) in order to predict the microfluidic behavior of the stacked-flow device. The device was modeled in 2-D as an infinite slit using previously described methods[23]. The driving pressure of the model has to be reduced by a factor to compensate for the lower fluidic resistance of the infinite slit. Using experimental data gathered for gradient shape, the scaling factor can be estimated in order provide an appropriate driving pressure for the model. The model provides knowledge of the fluid flow and the shear forces at the surface in the cell culture chamber.

Surface gradient detection

In order to quantify the gradients generated by the device we utilized an epi-fluorescence surface imaging technique to collect intensity data from an approximately ~4.9 μm optical slice[24]. Concentrated solutions of 45 mM Orange-G were introduced into the device in both flow channels with one channel containing 1 mM fluorescein. The fluorescein source channel was configured at either the top or bottom flow levels to generate directionally different gradients. Data was collected at various driving pressures while equilibration times and stability was evaluated with time-lapse imaging.

Cell culture and time-lapse imaging

Cell culture medium was prepared from fresh RPMI 1640 supplemented with 2.05 mM L-glutamate, 1% penicillin-streptomycin, and 25 mM HEPES buffer. Cell culture substrates were prepared from clean glass slides coated with poly-D-lysine at 10 μg/ml for 1 hour at 37°C, rinsed thoroughly with PBS, and then coated with Collagen type IV at 2 μg/ml overnight at 37°C. MDA-MB-231 breast cancer cells were dissociated in cell dissociation buffer then plated at ~70,000 cells/slide in 300 μL on the substrates. Seeded substrates were cultured for 24 hours in a 37°C and 5% CO2 controlled incubator before

application of the vacuum sealing device. In preparation for applying to cell cultures, the device was vacuum sealed to a blank substrate and primed by flowing 2% BSA solution through the channels for several hours then replaced with medium containing 0.1% BSA and de-bubbled. The device is then released from its loading substrate and allowed to form a droplet of medium at the open surface of the cell culture chamber. Next, the device is carefully lowered onto the cell culture substrate while the droplet ensures that no air bubbles remain trapped within the chamber or contact with the cells. It is critical to allow flow through the device at a low driving pressure (0.2 psi) to prevent depressurization of the cell culture compartment when the vacuum channels seal against the substrate. The vacuum sealing operation is conducted under wet conditions thereby maintaining the supportive environment for the cells. Phase-contrast images were collected every 5 minutes over the course of 12 hours to track migration of the cells. Metamorph (Molecular Devices, Inc., Sunnyvale, CA) was used to threshold, segment and register the centroid of the cells in all the frames and MATLAB (Mathworks, Natick, MA) was used to analyze the data and track the trajectories of the centroids. The tracking algorithm started with the centroids registered in the last frame and worked recursively backwards to identify the nearest centroid in the previous frame, which belonged to a cell with similar attributes (area, and perimeter). This ensured that we analyzed only the cells, which remained in the frame for the entire 12-hour window.

2.4.2 Results and discussion

FEM predicts wide-area gradients and low shear forces at the surface

The 2-D simulation shown in **Figure 2.11(a-b)** predicts fluid transport and diffusive mixing for the stacked flows. The model is solved with fluorescein as the diffusing species (MW: 332.31 and diffusivity D ~ 6.4×10^{-6} cm^2/s) delivered via the

bottom inlet. In practice, the device is operated near driving pressures at which the stacked-flows evolve into a homogenous or fully mixed solution when they pass through the outlet of the gradient chamber; therefore the driving pressures for the model were chosen to mimic this condition. Using this guideline, simulations were produced to predict the fluid shear stresses for gradients generated with different diffusing species at a distance of 10 μm above the cell culture surface. With fluorescein, the model predicts shear stresses of ~6×10^{-3} dyn/cm^2 for 70% of the chamber length. At already two orders of magnitude below the reported threshold for inducing migration bias (~0.7 dyn/cm^2), the device is expected to be suitable for sensitive chemotaxis experiments[19]. In practice, for most proteins which diffuse slowly (e.g. the diffusivity of albumin is D ~ 6.4×10^{-7} cm^2/s), the gradient is generated at very small flow rates, so the shear stresses involved are another order of magnitude smaller.

Large-area surface gradients can be dynamically tuned

Surface-level gradients were quantified using an imaging technique for adapting regular epi-fluorescence microscopy to collect surface-level intensity[24]. We can limit the penetration length of the excitation light into our sample by flowing a mixture of non-fluorescent and fluorescent dyes, Orange-G and fluorescein respectively. The dyes are chosen because Orange-G absorbs strongly at the excitation wavelength (490 nm) and weakly at the emission wavelength of fluorescein (540 nm). In combination, the fluorescein dye competes with the Orange-G in solution for a finite amount of excitation energy. At a concentration of 45 mM for Orange G with a 0.6 NA objective, the characteristic penetration length is approximately 4.9 μm (for which the excitation light intensity is 1/e times the incident intensity of the excitation light)[25]. Since the intensity of the excitation light decays exponentially the farther it penetrates the solution, 95% of the collected emission light (1-1/e^3) is from within ~15 μm of the surface of the device as

shown in the example of **Figure 2.11(c)**. Using this technique, we characterized the stacked-flow gradients at different driving pressures and orientations of the source and sinks using fluorescein and Orange G as shown in **Figure 2.11(d)**. We found the surface gradients produced to be stable over 24 hours and reach equilibrium quickly (less than 5 min). Across the width, the gradients were highly uniform as demonstrated by the overlapping profiles of the intensity plots in each panel of **Figure 2.11(d)**. Furthermore, the gradients are dynamically tunable with the shape responding to the applied driving pressure as a result of the competing nature of the convection and inter-diffusion of the laminar flows. Additional flexibility in the gradient profiles can be achieved by independently controlling the driving pressures applied at the inlets to modify the gradient slope as shown in **Figure 2.12**.

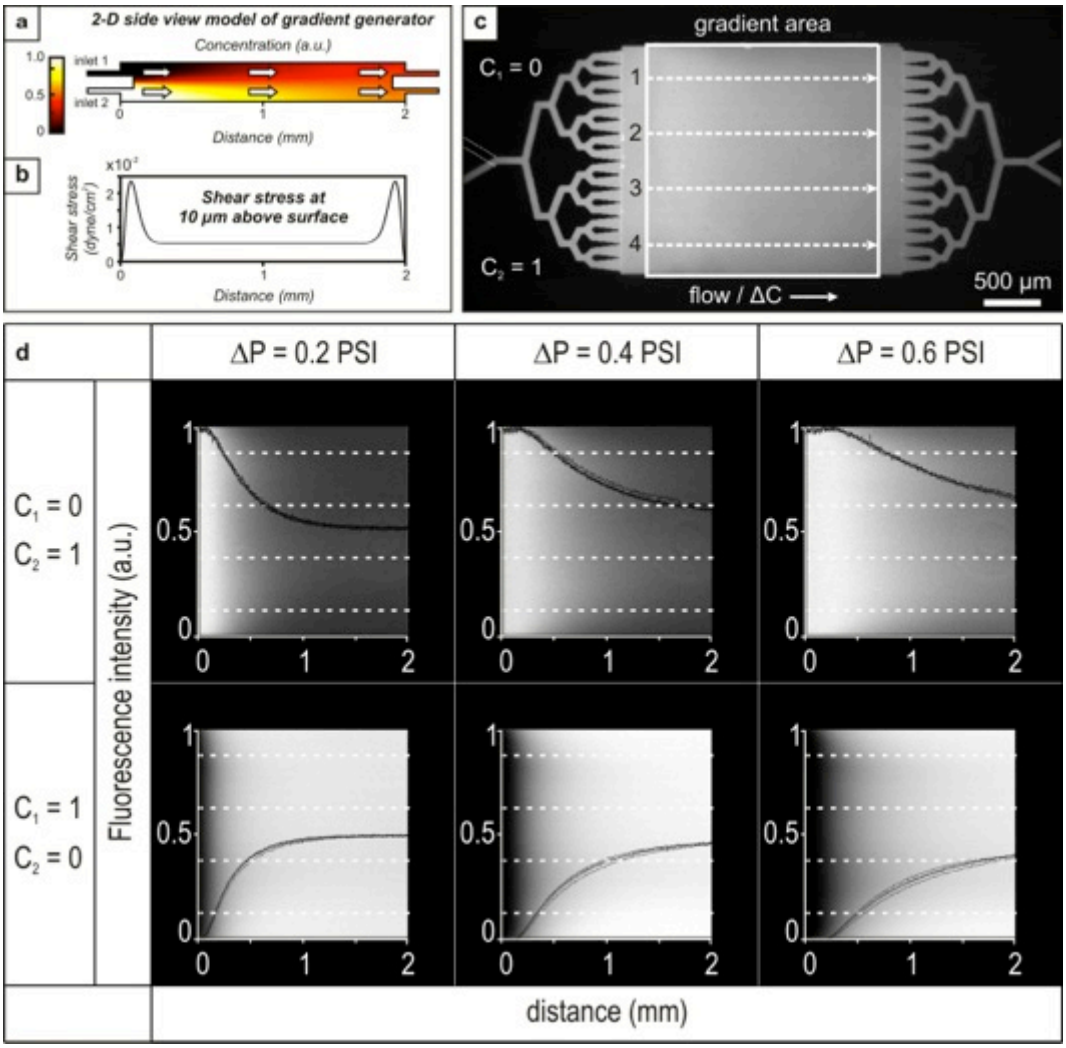

Figure 2.11: Finite-element modeling and fluorescence characterization of surface gradients. (a) A 2D model of the stacked-flow device is shown here with a representative gradient simulated with COMSOL using fluorescein as the diffusing species (D = 6.4×10^{-10} m^2 s^{-1}) (b) The simulate shear stress at a distance of 10 µm above the cell culture surface is ~6×10^{-3} dyne cm^{-2}, 2 orders of magnitude below the reported threshold for inducing a bias in neutrophil migration[19]. (c) A typical surface-level fluorescence micrograph of the device highlights the gradient area (box) and the locations of the intensity profile analysis (dotted lines). (d) In each of the six panels a fluorescence micrograph of the surface gradient area is superimposed with four corresponding intensity profiles (taken across the dashed horizontal white lines) in order to demonstrate lateral uniformity. The gradient can be dynamically tuned by the driving pressure, ΔP, and the direction of the gradient is dependent on the inlet configuration.

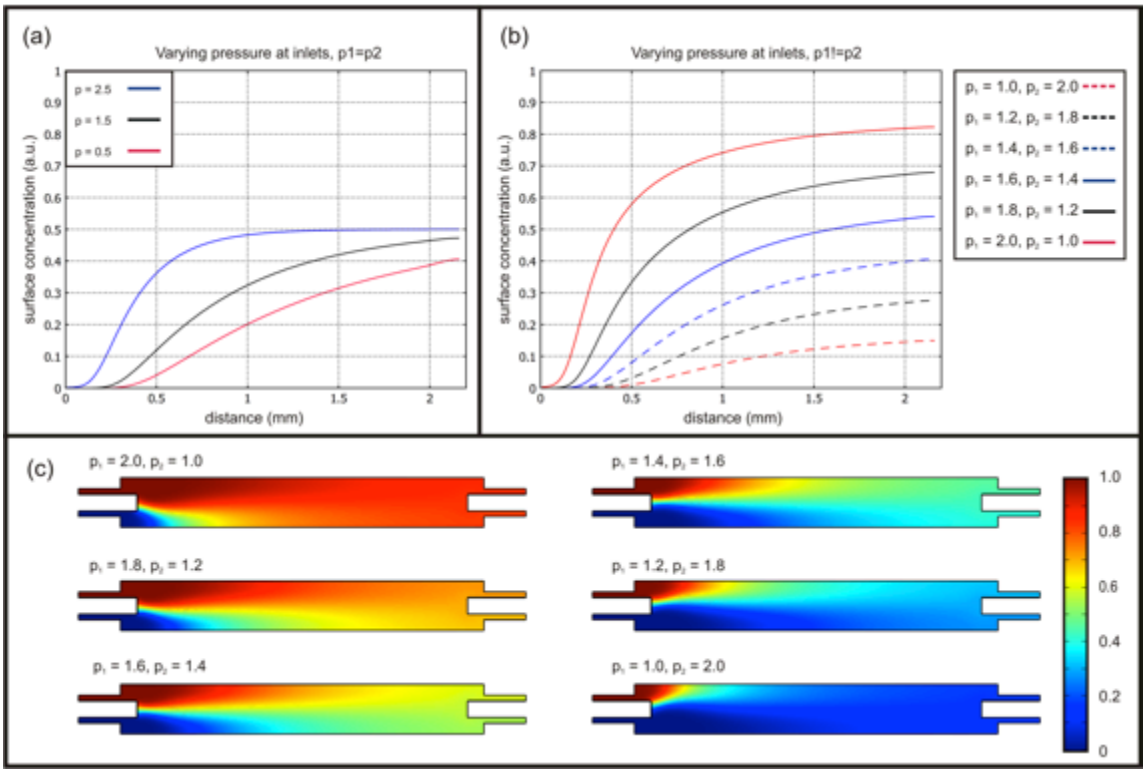

Figure 2.12: Finite-element modeling of surface gradients generated using stacked flows demonstrates dynamic tunability. Each of the series of plots were generated using fluorescein as the diffusing species (MW: 332.31 and D ~ 6.4×10-6 cm2/s). Driving pressures are unadjusted values from the 2-D simulation. In all simulations shown here the inlets were configured as C1 = 1, C2 = 0. (a) A plot of surface concentration profiles generated for different driving pressures applied equally to each inlet. See Fig.2d for comparison to experimentally acquired results. (b) A plot of surface concentration profiles generated with driving pressures applied differentially to each inlet. Notice that differential driving pressures enables further flexibility in the maximum concentration range imposed across the surface. (c) Cross-sectional plots are shown with a thermal map of the concentration profile throughout the microchannel for various pressure configurations.

Vacuum sealing operation and stacked-flow is benign to cell culture preparations

A prevailing drawback of other gradient generator devices is the required adaptation of cell culture protocols for enclosed microchannel designs. Optimizing culture conditions is increasingly difficult for sensitive cell types such as primary cultures which has led to the popularity of open-access designs[26,27]. However, a salient feature of

our device is the reversible sealing design that foregoes the adaptation of cell culture protocols. Importantly, the design enables the temporary application of the device and continued culture after gradient application. After removing the device to continue cell culture, we found that rinsing the substrate with fresh culture medium was adequate to remove the cells damaged beneath the sealing surface of the device. We think that these cells are either crushed or sheared away by the vacuum-sealing action, and therefore can be easily detached from the surface. Replenishing the cell culture with fresh medium removes any harmful factors that can potentially be released from the damaged or dead cells. Likewise, during application of the device, the continuous flow of fresh medium negates the possible effects of the damaged cells around the edge of the chamber boundary. The vacuum sealing operation was tested for pre-established cultures of MDA-MB-231 breast cancer cells. We chose this cell type in order to quantify the effects of shear flow on the random migration behavior. Cells were plated at low density on collagen-coated glass slides 24 hours prior to application of the device. We show in **Figure 2.13** that the application of the device does not interfere with the random migratory (chemokinesis) behavior of the cells over long-term application for 12 h. Additionally, the application of stacked-flow did not introduce migratory bias for these cells because it exerts negligible shear forces. Importantly, what we demonstrate is that our stacked-flow microchannel design is benign to cell culture preparations through the careful consideration of fluid flows and interfacing methods.

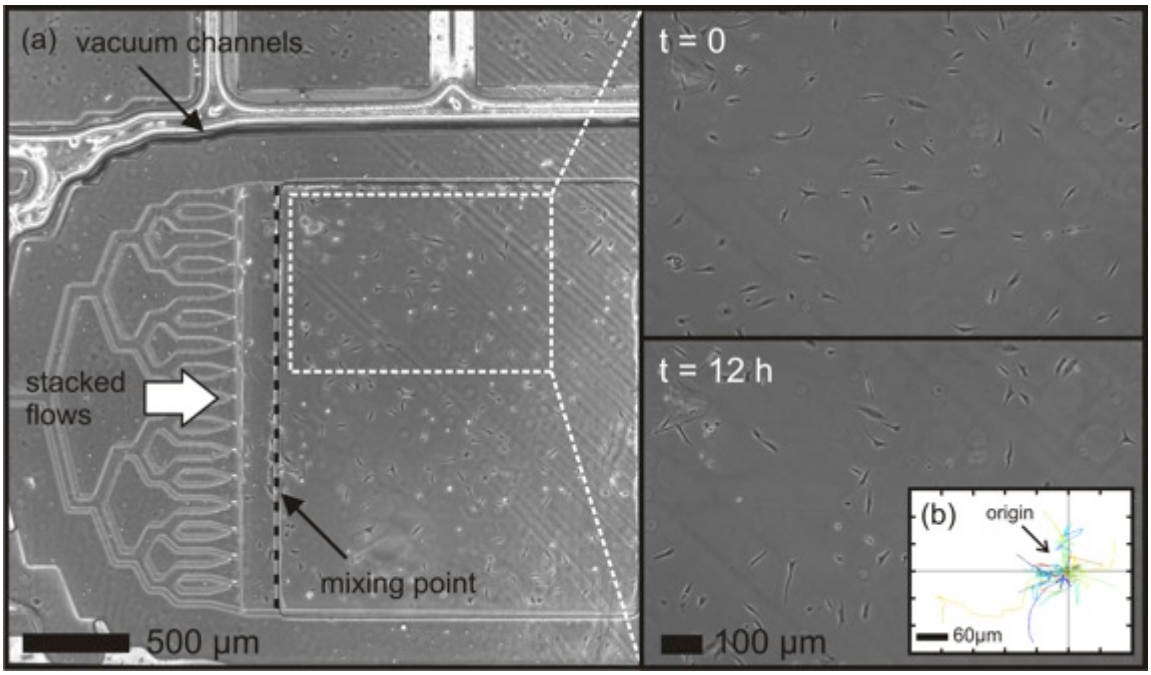

Figure 2.13: Vacuum sealing of the stacked-flow device to an established culture of MDA-MB-231 breast cancer cells. A phase-contrast micrograph of the device is shown on the left at low magnification to display the geometry of the device in relation to the cell culture. During application of the device the vacuum channels apply suction to the substrate in order to actively seal the open surface of the device against the substrate. After sealing, the cell culture is compartmentalized into the microfluidic channel. Our method of reversible sealing is notably benign with evidence of healthy breast cancer cells in the device for 12 hours as shown in the inset (enhanced). The lower right inset shows the trajectories of 26 cells, over 12 hours, with their initial positions collapsed onto the origin. It clearly shows that the flow through the chamber does not introduce any migrational bias in the cells. Phase-contrast images were collected every 5 minutes over the course of 12 hours to track migration of the cells. The resulting movie is shown at 7 fps with 140 total frames.

Scalable architecture enables arrays of multiple gradients

To demonstrate the scalable architecture of our design, we fabricated devices with 2x2 and 4x4 arrays of stacked-flow gradient generators. In the 2x2 array design shown in **Figure 2.14(a)**, blue and yellow dyes were introduced to visualize flow. One can imagine assays where the dyes represent different chemical titrations of the same

molecule, producing different gradient combinations at each element of the array. Across the diagonal of the array, equal concentrations would flow into the chambers to serve as controls for baseline concentrations; meanwhile, different concentrations intersect to produce complementary pairs of stacked-flow gradients. To further demonstrate scalability, we extended this design to produce a 4x4 array device as shown in **Figure 2.14(b)**. To highlight the 3-D microfluidic architecture, blue and yellow dyes were introduced at the row and column inlets, respectively. Careful design of the microchannel network with binary branching was used to ensure that each fluidic path from any inlet to the outlets is equivalent. These proof-of-concept devices show that our platform can be adapted for assaying of a wide range of gradients simultaneously. This feature would have particular utility when biologically relevant concentrations of a chemical cue are unknown; with high-throughput screening of gradients we could pinpoint the critical concentrations that elicit a response from cells.

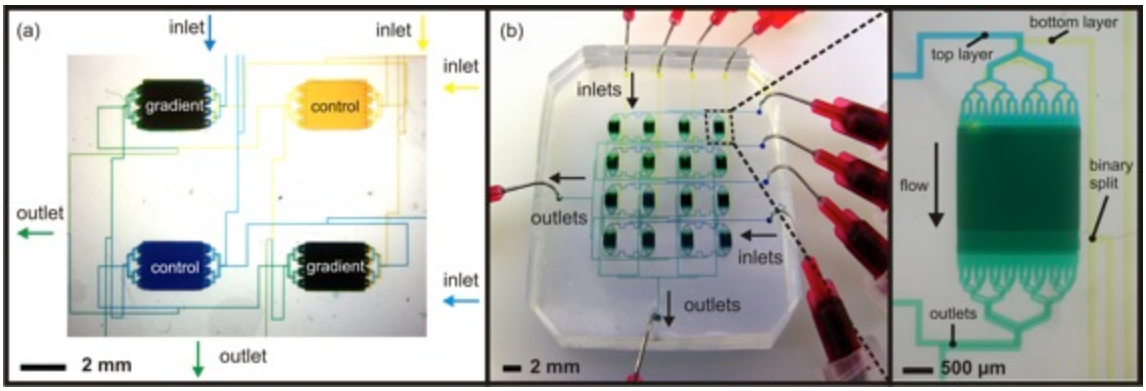

Figure 2.14: The scalable stacked-flow architecture enables arrays of gradient generators for high-throughput screening. (a) A 2x2 array of gradient generators is shown with yellow and blue dye representing different concentrations of a gradient molecule. Across the diaganol of the array, these elements serve as controls for different baseline concentrations (yellow and blue), whereas the remaining elements are complementary pairs of gradients (green). (b) A wide-field image of a 4x4 array device highlights the inherent scalability of the microchannel architecture. To visualize the overlapping flow, blue and yellow dyes are introduced into the row and column inlets (top and bottom layers) respectively. At each gradient chamber the top and bottom flows combine to produce a green solution at the outlets. In the inset on the right, a single gradient generator is shown to highlight the architecture of the individual elements.

2.4.3 Summary and assessment of the method

We have demonstrated a low-shear gradient generator design with vacuum sealing for straightforward interfacing with cell cultures. The modular nature of our device can allow for more advanced preparation of substrates and cell cultures such as patterning or long-term cell culture because it does not interfere with standard protocols. The device sealing is reversible which allows for handling of the cell cultures after exposure to the gradient. We have demonstrated quantifiable gradients that are highly stable over 24 hours and impart low fluid shear stress, which are critical for analysis of cell responses. With the scalability of the stacked-flow design, we can generate arrays of gradients from few inputs that are amenable to high-throughput screening. Further development of the arrayed devices to incorporate vacuum sealing could allow for such experiments. We

believe that the design principles demonstrated here are important to microfluidic community interested in the development of user-friendly devices. However, the device is not without limitations: for vacuum-sealing portability is reduced and shear forces applied at the moment of application are poorly defined. The requirement of an active source of vacuum limits portability; an important concern when sterility must be maintained and transport is required between laminar flow hoods and microscopy stations. In our experiments, the application of the device onto the pre-existing cell culture substrate was a source of user error. It was necessary to finely tune the vacuum pressure and flow through the device in order to prevent a negative pressure from being abruptly applied to the cells when the device made contact with the cell culture substrate. While featuring low shear stresses and large-area gradients, the stacked flow principle is fundamentally limited for live monitoring of the gradient status due to overlapping flows in the z-direction for standard fluorescence. Without surface-level or confocal imaging technique, it is impossible to know the exact state of the gradient over the course of a cell culture experiment. Overall, the method offers stable, well-characterized gradients, yet its requirement for a vacuum source and non-traditional image modalities limits its practical use.

2.5 An Open-Surface Micro-Dispenser Valve for the Local Stimulation of Conventional Tissue Cultures

The content of this section has been published in the conference proceeding:

Sip, C. G., and A. Folch. "An Open-surface Micro-dispenser Valve for the Local Stimulation of Conventional Tissue Cultures." MicroTAS 2010. Proceedings of the 14th International Conference on Miniaturized Systems for Chemistry and Life Sciences. Groningen, The Netherlands (2010).

This paper reports a novel microdevice for locally delivering biochemical stimuli to conventional, non-microfluidic cell cultures. The device is lowered by hand onto a cell culture surface where it is self-supported. A "micro-dispenser" valve mechanism controls the release of stimuli by the occlusion of micro-apertures. Flow released from the apertures generates concentration gradients similar to those generated by the micropipette assay. Surface gradient profiles were characterized by collecting surface-level fluorescence. A principle feature of our platform is that by positioning our microvalve directly beneath the point of stimulation we have low dead volume, rapid response time, and efficiently utilized device real estate in a manner well suited for multiplexing and high-throughput applications.

While microfluidic systems are often touted as having higher throughput with parallelization, there are significant challenges to interfacing with biological samples such as cells and tissue slices. Cell culture protocols that are based on static culture conditions do not translate immediately to enclosed systems with microfluidic conduits, flows, and small volumes. Therefore, microfluidic systems that offer straightforward integration with conventional tissue culture technique have an important advantage. A few designs satisfy this criteria: a microfluidic add-on allows for standard integration with electrophysiology chambers[28]; the "microjets" device simplifies cell seeding for microfluidic chemotaxis assays[23,25,29]; the axon isolation device simplifies neuron culture[30–33]; and the "microfluidic probe" separates the cell culture substrate from the

microfluidic device entirely[34–36]. The design presented here shares similar fundamentals as the "microfluidic probe" (modularity, flow through apertures); however it utilizes a new type of microvalve to enable temporal control of the delivered biochemical stimuli.

2.5.1. Micro-dispenser device design for controlled stimulation

The device consists of a flat surface (parallel to the cell culture surface) that features apertures, each of which directs flow from embedded microchannels. A "micro-dispenser" valve controls the release of fluid through apertures and into the fluidic environment external to the device. An isometric schematic is shown **Figure 2.15** highlighting the multi-layer architecture of the device. A brightfield micrograph of a 2x2 array micro-dispenser device loaded with dyes for visualization is shown in **Figure 2.16(a)**. A bolus of "stimulant" is delivered to the external environment of the device by actuation of the valve pads directly beneath the surface aperture (75-100 μm diam.). The operation of the micro-dispenser valves (see schematic in **Figure 2.16(b)**) provides spatial and temporal control over stimulation that distinguishes it from other devices lacking microvalves[28,34–37]. During stimulation, the valve pad is relaxed allowing flow from the embedded microchannels through the apertures and into the external medium. A pressure differential drives the stimulating solution through the apertures. To stop stimulation the device can be operated to purge the local environment. The pressure differential is reversed in order to redirect flow from the external environment back through the aperture and through the microchannels to a waste outlet. To seal the surface aperture, the valve control channel is pressurized in order to deform the valve membrane against the inner surface. The balance of pressures and pulsing frequency are used to control the temporal evolution of the stimulant bolus and effectively limit the stimulation diameter. The device can be operated cyclically to deliver pulses of stimuli, or adjacent

apertures can be configured to continuously perfuse and aspirate, generating a steady-state jet of stimuli similar in performance to the "microfluidic probe" device[34,35].

For cell culture applications, we developed an inverted version of our device for positioning of the aperture surface 200 μm above a conventional cell culture substrate. In practice, the device is lowered by hand onto the cell culture surface where it is self-supported by microfabricated features. For tissue culture applications, we developed an upright version of our device that allows for a tissue slice preparation to be placed in direct contact.

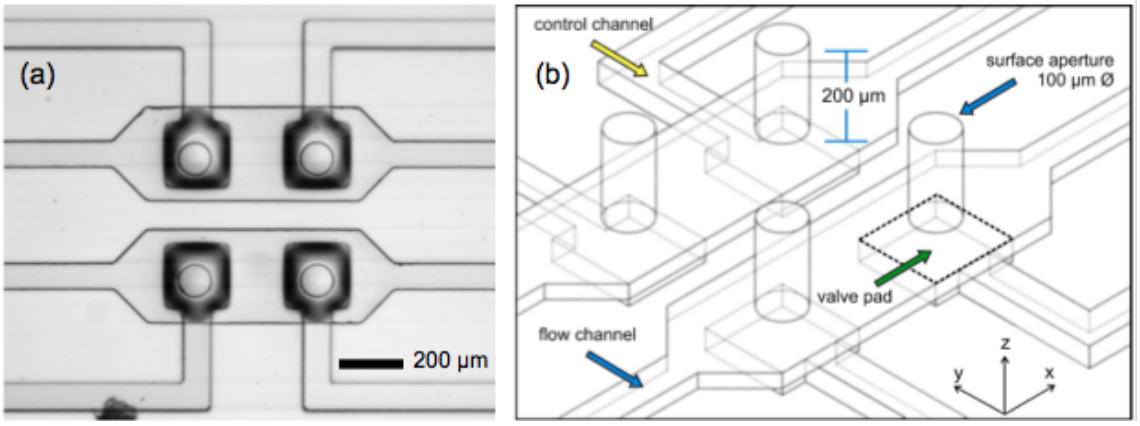

Figure 2.15: Micro-dispenser device design. (a) A brightfield microscope image of a device with a 2x2 array of stimulation apertures. (b) An isometric schematic of the device. A flow channel layer, elastomeric membrane, valve control layer, and apertures are arranged in a multilayer architecture.

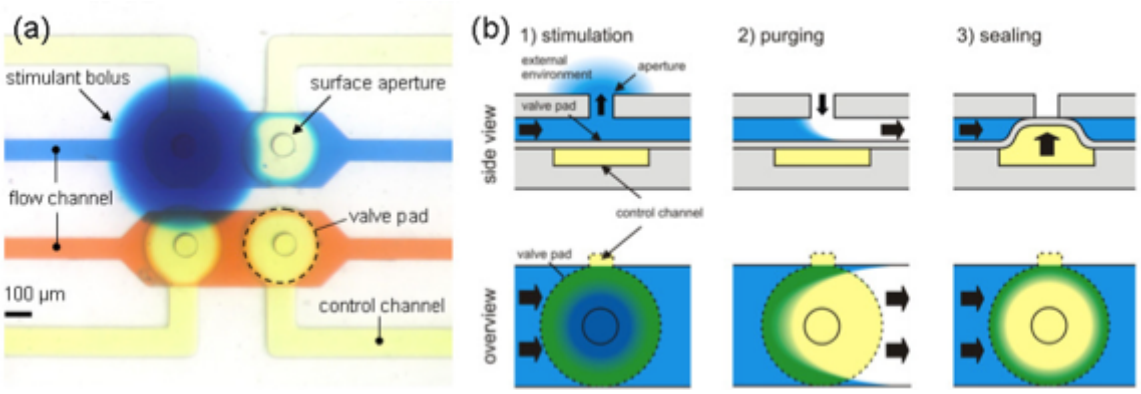

Figure 2.16: The principle of operation for the micro-dispenser stimulation device. (a) A color brightfield micrograph showing stimulation channels loaded with red and blue dyes, and valves with yellow dye. The 2x2 array of apertures are selectively sealed or unsealed by the actuation of the valves and deformation of the membrane in the reagion of the valve pad. In this image, the valve in the top left position is relaxed and pressure driving flow through the blue flow channel causes a bolus to be released radially into the external medium. (b) The sequence of operation for stimulation, purging, and sealing is shown in side and overview schematics. During stimulation, the valve is relaxed and flow through the channel escapes through the aperture. During purging, the pressure differential is greater towards the outlet, so flow reverses direction to clear the stimulus from the external environment. During sealing, the valve channel is pressurized greater than the driving channel and the valve membrane occludes the aperture.

2.5.2. Methods and Results

Fabrication

Our fabrication method uses plasma bonding assembly of 3 layers of polydimethylsiloxane (PDMS), made from SU-8 patterned masters with standard replica molding, spin-casting, and exclusion molding processes[38]. The characteristic feature of the micro-dispenser valve mechanism is an integrated elastomeric membrane coupled to open-surface apertures (75 μm diam.). As shown in **Figure 2.17**, the layer-by-layer composition of the upright and inverted configurations of the device is similar. Each device consists of 3 monolithic layers: the valve layer (I), the flow layer (II), and the aperture layer (III). The valve layer is replica molded as a slab several millimeters thick

from 75 μm tall features. The flow layer and membrane are formed simultaneously by directly spin-casting a 3:1 mixture of PDMS to hexane at 3000 rpm over 35 μm tall features. The valve layer is produced by exclusion molding PDMS pre-polymer against 200 μm tall features[38]. Each layer is sequentially bonded using plasma oxidation starting with layer I. To configure a device as upright or inverted, the punching of inlets is either done in the valve layer or in additional inlet/outlet slabs of PDMS.

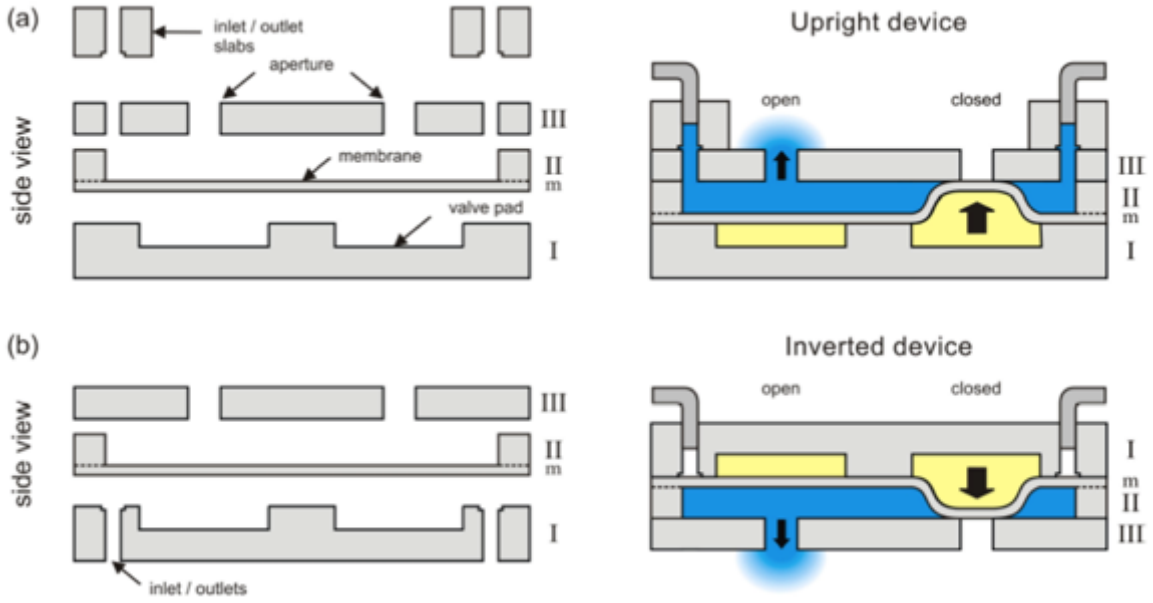

Figure 2.17: Multilayer soft-lithography fabrication of the micro-dispenser. Fabrication and operation of (a) upright and (b) inverted versions of the micro-dispenser device. The valve layer (I) is cast as a PDMS replica several mm thick. The flow layer (II) and membrane (m) is produced simultaneously by spin-coating liquid PDMS directly over the SU-8 features on the master mold. The aperture layer (III) is fabricated using exclusion molding technique[38]. The inlets and outlets are either cored into additional slabs of PDMS or into the valve layer for the upright or the inverted versions of the device.

Micro-dispenser valve sealing pressure

The micro-dispenser device flows were controlled by switching pressure states applied to the inlets, outlets, and valve control channels. The operation of the device was automated by controlling a rack of miniature solenoid switches with a custom LabView

program. Valve sequences were scripted to toggle the state of individual valves or driving pressures with 100 ms resolution. In order to determine reliable operating parameters for the device, several designs were fabricated with varying membrane thickness and separation gap between the valve and the sealing surface of the aperture. The separation gap is controlled by the thickness of the SU-8 layer for the master mold to generate the flow layer (II) (see **Figure 2.17**). The membrane thickness is controlled by the PDMS spin-coating parameters. A survey of sealing pressures was measured for a series of devices made with different parameters as shown in **Figure 2.18**. Generally, the thicker membrane (3000 RPM) and the taller the SU-8 features required more sealing pressure. For further experiments, the device was fabricated with 35 μm tall features for the flow layer and using a membrane spin-coated at 3000 RPM. These features produced robust valves as a result of the thicker membrane and lower required sealing pressures.

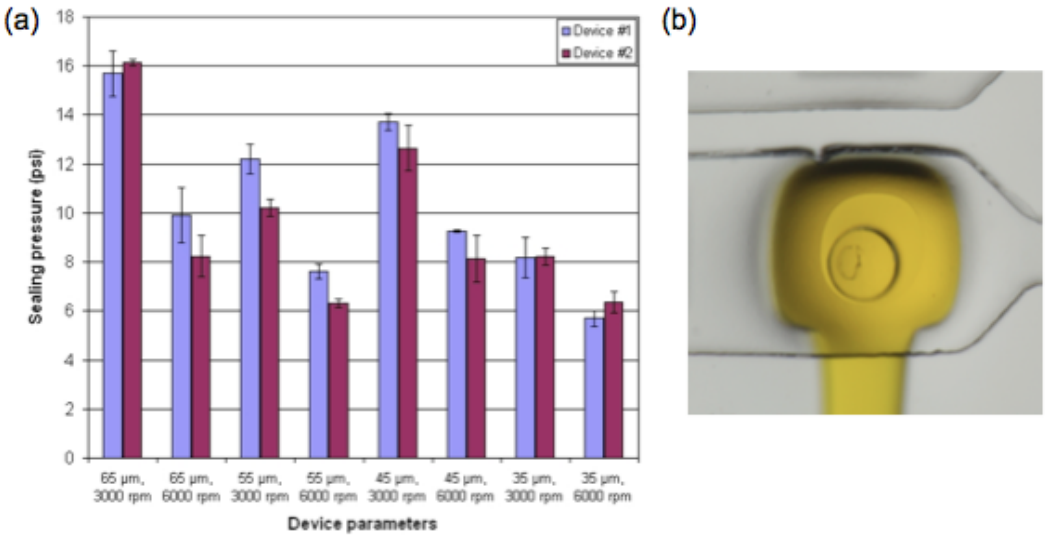

Figure 2.18: Sealing pressures for varying device parameters of the micro-dispenser device. (a) The membrane thickness as defined by the spin-coating speed and the thickness of the SU-8 layer for the flow channels were varied to determine the required pressures to seal the apertures. (b) An image of irregular deformation that occurs at high sealing pressures.

Surface-fluorescence characterization

For the inverted device, the surface gradient profile of the stimulated area was characterized by delivering a mixture of fluorescein (M.W. 376.27, 490/540 nm) and Orange G, a non-fluorescent dye that absorbs strongly at 490 nm and weakly at the 540 nm, to collect surface-level fluorescence using an inverted epi-fluorescence microscope[24]. Using this technique we were able to image an approximately 5 μm thick optical slice and characterize the profiles of the stimulated region for a variety of parameters and operation modes (pulsing, jets, frequencies, and pressures).

Shown in **Figure 2.19** is a series of surface-level epi-fluorescence micrographs (~5 μm optical slice) of a fluorescein solution delivered to an external surface separated by 200 μm from the aperture of the device. The surface area of the simulated region can be dynamically tuned as shown by the fluorescence profiles given for several driving pressures in **Figure 2.19(a)**. Representative of this data, in **Figure 2.19(b)** a plot of the cross-sectional profiles is shown corresponding to a 1 second stimulant pulse delivered in 2 second intervals for various driving pressures. Cross-sectional profiles were measured horizontally for 880 μm across the fluorescence images and through the center of the aperture. In **Figure 2.19(c)** the micro-dispenser was operated in "jetting" mode with adjacent apertures flowing or aspirating to demonstrate a steady state gradient.

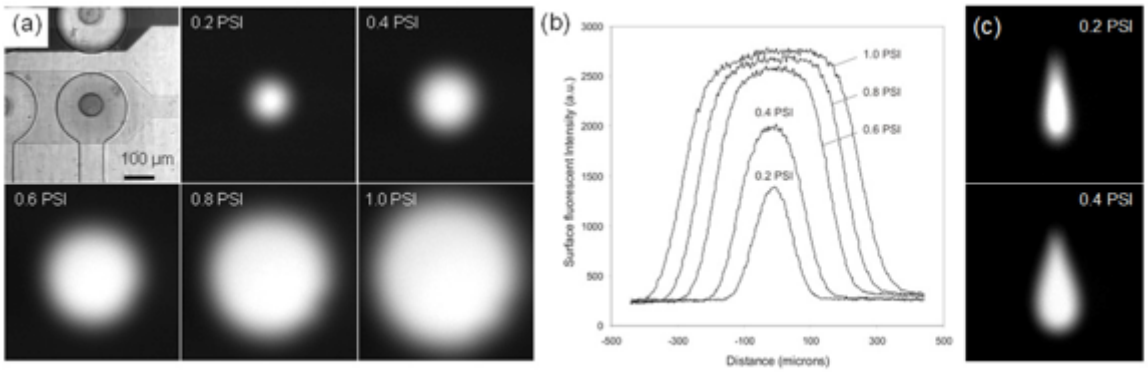

Figure 2.19: Surface-level fluorescence characterization of micro-dispenser stimulation. (a) In the first panel a brightfield image corresponds to the scale and position of the device for the following surface-fluorescence micrographs taken with different driving pressures after delivering a 1 sec stimulus. (b) A plot of the cross-sectional profiles characteristic of the driving pressures in (a). (c) An example of the gradients possible while operating the device in "jetting" mode using constant delivery and aspiration from adjacent apertures to generate a steady state gradient.

2.5.3. Summary and assessment of the method

A 2x2 array of micro-dispenser apertures was demonstrated, but the valve design is scalable and could, in principle, be used for larger arrays of stimulation sites. The valve design offers flexibility spatial and temporal control of stimulation that could be controlled by on-chip multiplexing to increase the density of apertures[1,39]. The micro-dispenser device was designed to interface with existing cell cultures or tissue slices in order to simplify culture conditions. In order to fabricate devices for stimulation in larger arrays, we required more reliable methods of fabricating the apertures layer. The following section details a fabrication method for integrating layers made of SU-8 to address this issue.

2.6 Irreversible Bonding of SU-8 Microstructures onto PDMS devices

The content of this section has been published in the conference proceeding:

Sip, C. G., and A. Folch. "Irreversible Integration Of SU-8 Microstructures Into PDMS Devices." In MicroTAS 2010. Proceedings of the 14th International Conference on Miniaturized Systems for Chemistry and Life Sciences. Groningen, The Netherlands.

In an effort to increase the density and shrink the diameter of apertures for the micro-dispenser device, a method of integrating SU-8 microstructures with PDMS was developed. The method begins with the treatment of silicon wafer substrates to render the central region non-adherent for SU-8. Standard SU-8 processing is followed to produce photo-patterned and dry releasable SU-8 components after the solvent development step. The integration of SU-8 microstructures into PDMS devices is achieved by chemical bonding through an amine–epoxide silane coupling reaction as previously described[20]. Here, we have demonstrated hybrid PDMS/SU-8 devices that withstand pressures of 15 psi after 48 hours in water immersion.

SU-8 is a commonly used epoxy-based negative photoresist that capable of producing high aspect ratio microstructures with thicknesses on the order of nanometers to 1 mm. Its characteristics of high optical transparency, chemical resistance, and biocompatibility make it attractive for integration into microfluidic devices. Typically, releasing of cross-linked SU-8 structures after development is done by either degradation of a sacrificial layer or dry release from a non-adherent substrate[40–43]. The sacrificial layer technique has limitations with the etching rate and increased surface roughness, while the dry release methods suffer from lower substrate wettability as described in Cheng et al.[43]. In general, a surface for dry SU-8 release must be a compromise between an adhesion high enough for spin-coating and an adhesion low enough to be peeled off after exposure and post-bake processing[42]. Typically when spin-coating SU-8 on a non-adhesive surface such as polystyrene or PDMS, the mismatched surface energy results in

de-wetting during when the solvent is evaporating in the pre-baking step. As a result the spin-coated SU-8 layer is highly uneven. In the method presented here, we avoid the negative aspects of an anti-adhesion layer by partitioning our substrate into adherent and non-adherent regions. The method enables dry release and standard spin-coating without the drawbacks of low surface wettability. The releasable SU-8 microstructures can be readily integrated with PDMS using a chemical bonding strategy to fabricate multilayer microfluidic devices. Overall, this process has a higher yield of useful polymer layers in comparison to PDMS based exclusion molding[38], and suffers only from the constraints of standard SU-8 processing and the normal sources of defect that occur during spin-coat processing (e.g. dust particles).

2.6.1. Methods and results

SU-8 dry release method

The method begins with the partial treatment of a silicon substrate with a fluorinated trichlorosilane to render the central region non-adherent for SU-8. As shown in **Figure 2.20(a)**, a portion of the wafer surface near the edge remains adherent towards SU-8 in order to prevent reflow of spin-coated polymer during the solvent evaporation step. With this technique, standard processing is followed to produce SU-8 components that can be released from the substrate after development. The substrates can be reused in contrast to methods that make use of a sacrificial layer for SU-8 release[40,41]. Typically, a fully non-adherent substrate would suffer from severe reflow due to low surface wettability. In our method reflow is avoided by excluding the outer region of the wafer from the surface modification; limitations appear at thinner spin-coatings (< 12.5 μm) due to contamination of the surface with particulates and air bubbles that can nucleate pockets of reflow. Traditionally, integration of PDMS with other materials has been

difficult; however, an amine–epoxide silane coupling reaction has been recently demonstrated for integrating PDMS and various plastic materials[20]. Our technique provides the framework for the layer-by-layer fabrication of microdevices in which 3-D microchannels, or large arrays of interconnections or apertures are typically limited by PDMS only designs.

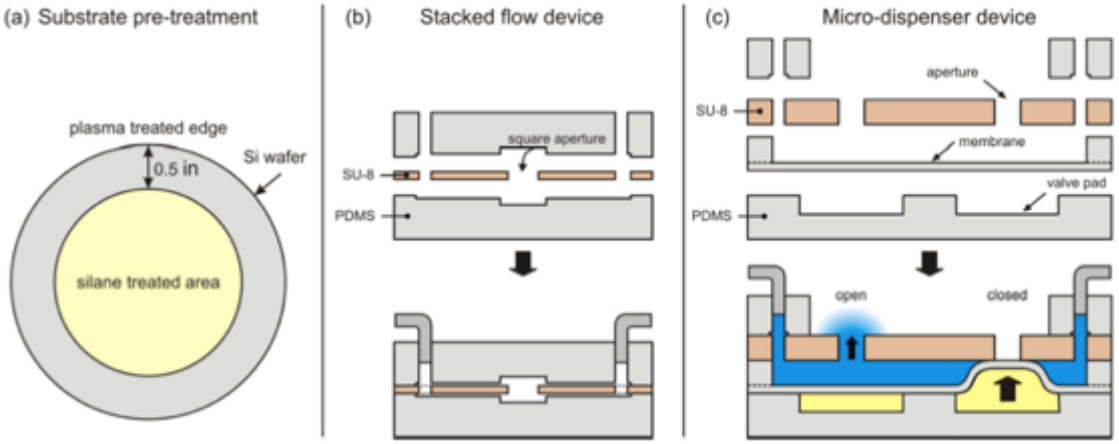

Figure 2.20: SU-8 dry release substrate treatment and method. (a) Substrate pre-treatment for SU-8 release and multi-layer fabrication of hybrid SU-8/PDMS devices. (b) Integration of an SU-8 layer as a replacement for the exclusion molded layer of a stacked flow device. (c) Integration of an SU-8 layer for high-density apertures in a version of the micro-dispenser device.

Fabrication and pressure testing of PDMS-SU-8 hybrid devices

A bare 4" silicon wafer is first vapor treated with (Tridecafluoro-1,1,2,2-Tetrahydrooctyl)-1Trichlorosilane (United Chem. Tech.) to render the surface hydrophobic and non-adherent for SU-8. Next, a 3" diameter PDMS slab is pressed against the center of the wafer to mask the central region. After O_2 plasma treatment, the hydrophobic silane modification remains only in the masked area and the outer 0.5" edge returns to a native hydrophilic Si/SiO_2 surface as depicted in **Figure 2.20(a)**. Shown in **Figure 2.20(b)** is a cross-sectional schematic of a version of the stacked flow device[44] used for pressure testing. Shown in **Figure 2.20(c)** is a cross-sectional schematic of the

fabrication process for a version of the micro-dispenser device[45] in which the surface apertures were fabricated from a released SU-8 layer to improve the density and shrink the diameter. PDMS layers were prepared from SU-8 patterned masters with replica molding, spin-casting, and exclusion molding as described in the previously. Next, each PDMS layer was plasma oxidized and modified using a condensation reaction of 5% 3-aminopropyltriethoxysilane (APTES) (Sigma) in water solution at 80°C. After solvent development of a releasable SU-8 layer, the structure can be removed by gently initiating delamination with a sharp razor before or after bonding to PDMS layers as preferred. Layer-by-layer construction of devices is then accomplished by room temperature bonding with conformal contact between APTES-modified PDMS layers and epoxy groups inherent to the SU-8 structures.

Releasable SU-8 layers were reliably produced in the range of 12.5-200 μm with the success of thinner layers limited by the contamination of our substrates by dust particles or air bubbles trapped in the photoresist. Pressure testing of a hybrid PDMS/SU-8 stacked flow device demonstrated burst pressures greater than 15 psi after 48 hours of water immersion. In **Figure 2.21(a)**, the stacked flow device is shown at a pressure of 15 psi with dye loaded for visualization. **Figure 2.21(b)** shows a micro-dispenser device that combines PDMS-based microvalves with a SU-8 layer containing 98 surface apertures (50 μm diam.). The microvalves exploit the elastomeric properties of the PDMS to seal the SU-8 apertures from the underlying flow channels

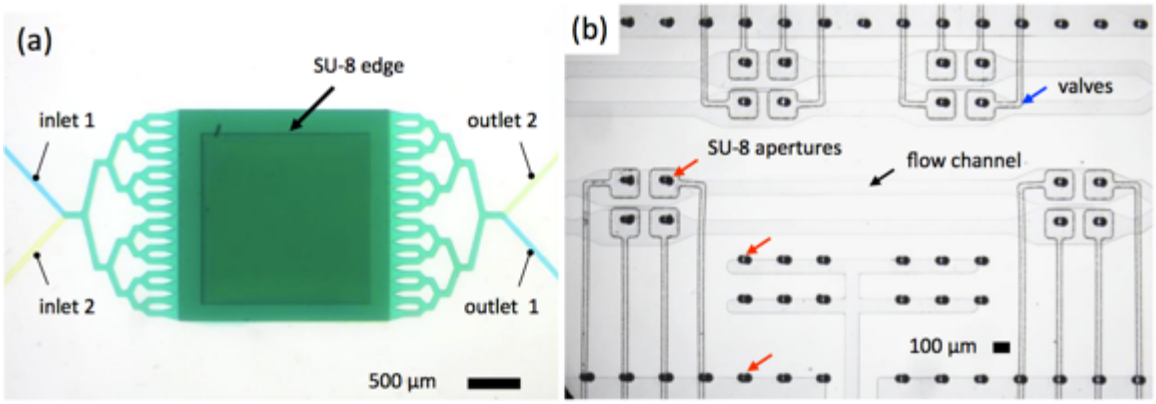

Figure 2.21: Hybrid PDMS/SU-8 devices with high-resolution and large arrays of apertures. (a) A stacked flow device used for pressure testing (shown here at 15 psi after 48 hours of water immersion. (b) A micro-dispenser device designed with higher-density of surface apertures and smaller diameter (50 µm) for application to cultured brain tissue slices.

2.6.2 Summary and assessment of the method

In comparison to other methods for SU-8 release, this strategy employs a simple substrate modification to enable dry release using chemicals and processes commonly found in microfabrication labs. SU-8 is a desirable material for fabricating devices with thin layers of small apertures because the photolithography process can be exploited to produce features with finer resolution and higher fidelity than produced by typical PDMS methods such as exclusion molding[38]. The examples shown here were designed to increase the density of apertures for the micro-dispenser device to enable stimulation across larger areas. Overall, this process can make possible more complex 3-D microfluidic devices by relaxing traditional design constraints imposed by PDMS fabrication.

2.7 A MICROFLUIDIC PLATFORM FOR GENERATION OF SHARP GRADIENTS IN OPEN-ACCESS CULTURE

Cate, David M., Christopher G. Sip, and Albert Folch. "A Microfluidic Platform for Generation of Sharp Gradients in Open-access Culture." *Biomicrofluidics* 4, no. 4 (2010): 044105. doi:10.1063/1.3490784.

This paper reports a microfluidic device for delivering gradients of soluble molecules to cells in an open reservoir without exposing the cells to flow. The cells are cultured on a polyethylene terephthalate (PET) track-etched membrane through which underlying flows delivery a concentration gradient. At the time of this work, existing methods for fabricating PDMS/PET devices were lacking. In order to achieve reliable sealing and leak-free device operation, a fabrication strategy was developed that does not require adhesives to bond the PET membrane and PDMS layers. Micromolded features in the PDMS layers seal the PET membrane within the device after assembly with standard oxygen plasma bonding. Surface gradients were characterized with epi-fluorescence microscopy; image analysis verified that sharp gradients (~33 μm wide) could be reproducibly generated. We show that heterogeneous laminar flow patterns of fluorescent live-cell stains applied beneath the membrane reach cells cultured on the other side; fluorescent profile scans show that the extent of reagent diffusion between adjacent flows is 10–20 μm indicating flow is restricted by the membrane. The device is improves upon preceding works[46], because the cell culture surface is readily accessible. With an open well, cells are accessible to physical manipulation (e.g., pipette access), the medium is in direct contact with the incubator atmosphere (i.e., no special protocols for ensuring proper equilibration of gas concentrations are required). Additionally, the membrane ensures that cells are not subjected to flow-induced shear forces that is a common limitation of flow-based microfluidic designs.

There are several microfluidic designs that rely on restriction of flow by isolating cells[26,47,48]. Designs with high-resistance microchannels have been developed that

significantly reduce shear stress on cells during gradient generation without compromising gradient stability[23,25,29,49–51]. In some of these designs, fluidic channels of only a few microns in height and width restrict flow such that diffusion is the dominant mode of transport in regions adjacent to cells. Integrating a semipermeable barrier, such as a hydrogel[52,53] or high-resistance membrane[54–56], between the cell chamber area and the fluid channels has also been explored for producing gradients of negligible flow. Hydrogels can be selectively formed inside a microfluidic device through gelation of a precursor liquid, however image contrast of cells is reduced. Incorporating commercially available polymer membranes into devices for gradient generation has also been investigated[57,58]. The advantages that prefabricated membranes have over hydrogels are that (a) they can be made thin (10-20 μm), responding quickly to fast-changing gradients or to gradients of small, rapidly diffusing molecules, and that (b) their surface chemistry and rigidity are more amenable for bonding and integration into devices. Additionally, track-etched membranes area available in transparent material with well-defined pore size, pore sizes, and porosity. With pores sizes of 0.4-1.0 μm these membranes are typically used as cell culture supports for assessing endothelial transport. We describe here a fabrication technique for the incorporation of transparent PET track-etched membrane in devices and demonstrate stimulating cells with sharp, shear-free gradients.

2.7.1. Methods and results

The goal of this study was to develop a microfluidic gradient generating platform capable of exposing cells to fast-changing gradients under shear-free conditions. To avoid shear stress, we cultured the cells on a transparent PET track-etched membrane and heterogeneous laminar flow patterns were applied below the membrane. The membrane inhibits potentially cell-damaging shear stress while permitting transport through high resistance pores. Restriction of flow through the membrane does not favor lateral diffusion of streams, because pores are of high aspect ratio and aligned orthogonal to the surface of the membrane. The device consists of a very simple gradient generator interfaced with an open well; the design is amenable for straightforward cell culture, preconditioning, or experimental treatment of cells using conventional cell culture technique. A simple gradient design was demonstrated; however this approach is scalable to a variety of gradient shapes.

Adhesive-free fabrication of PDMS devices with integrated membranes

The device is comprised of 4 micromolded PDMS layers, a top layer, two middle layers, and a bottom layer. A large opening in the uppermost layer constitutes a well for plating cells on the track-etched membrane (pore diameter of 0.4 μm) that is positioned below and is sandwiched between the middle PDMS layers. Microchannels located in the bottom layer deliver fluid from the device's inlets to the main reservoir where molecules freely diffuse through the membrane to cells on the other side. The fabrication of the device is shown schematically in **Figure 2.22**. The PDMS layers (layers I–IV) are made using standard replica molding or exclusion-molding technique to produce thin layers.[38] The two middle layers (layers II and III) sandwich the membrane to prevent leakage between the cell culture well and underlying microchannels. A micromolded recess in layer II helps to position and align the membrane. The bonding the "lid", layer

III, seals the perimeter of the membrane. Additional measures were not required to fortify the seal around the membrane using adhesive agents.

Characterization of laminar flow stability and gradient shape

We first characterized the stability of a gradient formed by a Y-configuration of two fluid streams at the bottom channel (**Figure 2.23**). The extent of surface-level mixing at the gradient interface over a 4 h time course was quantified using gradient of fluorescein dye in homogenous solution of the non-fluorescent dye Orange G[24]. This method of measuring surface-level concentration profiles at the bottom of the fluid channel (surface closest to objective) allowed us to predict what the diffusion profile of the gradient looked like directly beneath the cells, assuming little mixing occurs within the membrane due to the geometry of the track-etched pores.

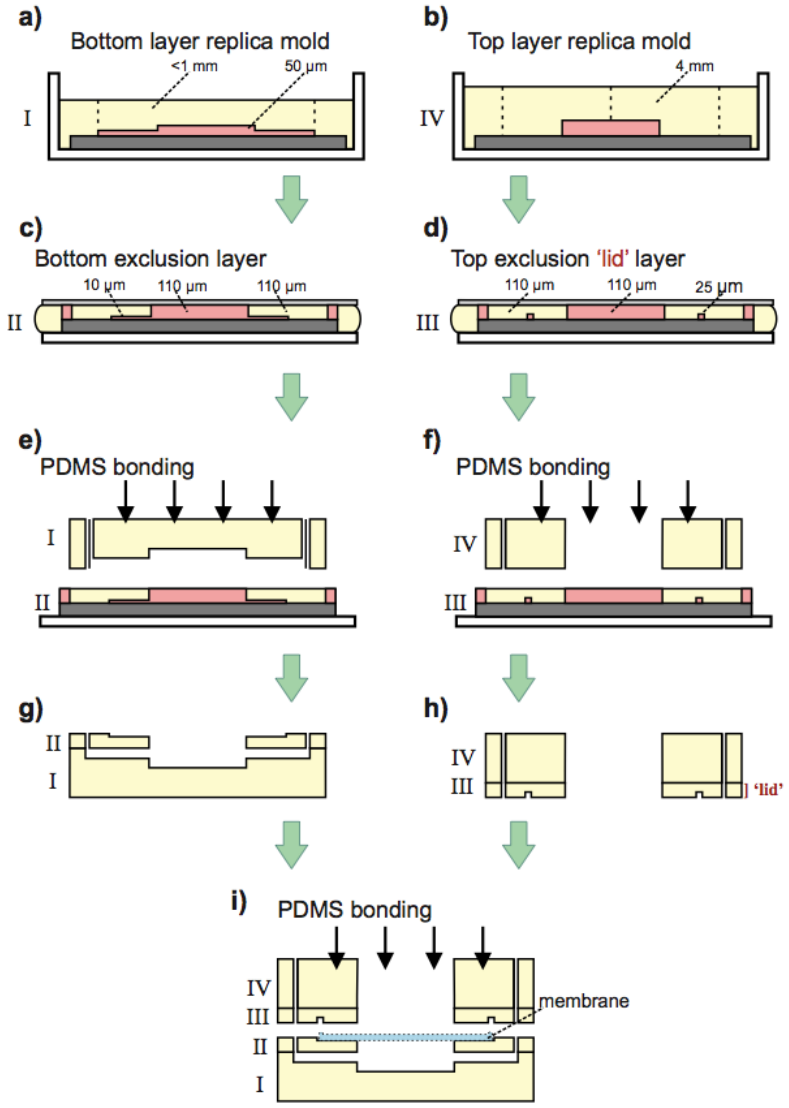

Figure 2.22: Fabrication schematic for the open-surface gradient device using an integrated track-etched membrane. (a-b) Replica molds are cast against SU-8 photopatterned silicon wafers for the top and bottom layers. (c-d) Thin PDMS layers are exclusion molding[38]. (e-f) Oxygen plasma bonding is used to assemble top and bottom components (g-h). (i) A final oxygen plasma bonding step seals a track-etched membrane within the device. The "lid" and features in layers II serve to embed the membrane between PDMS.

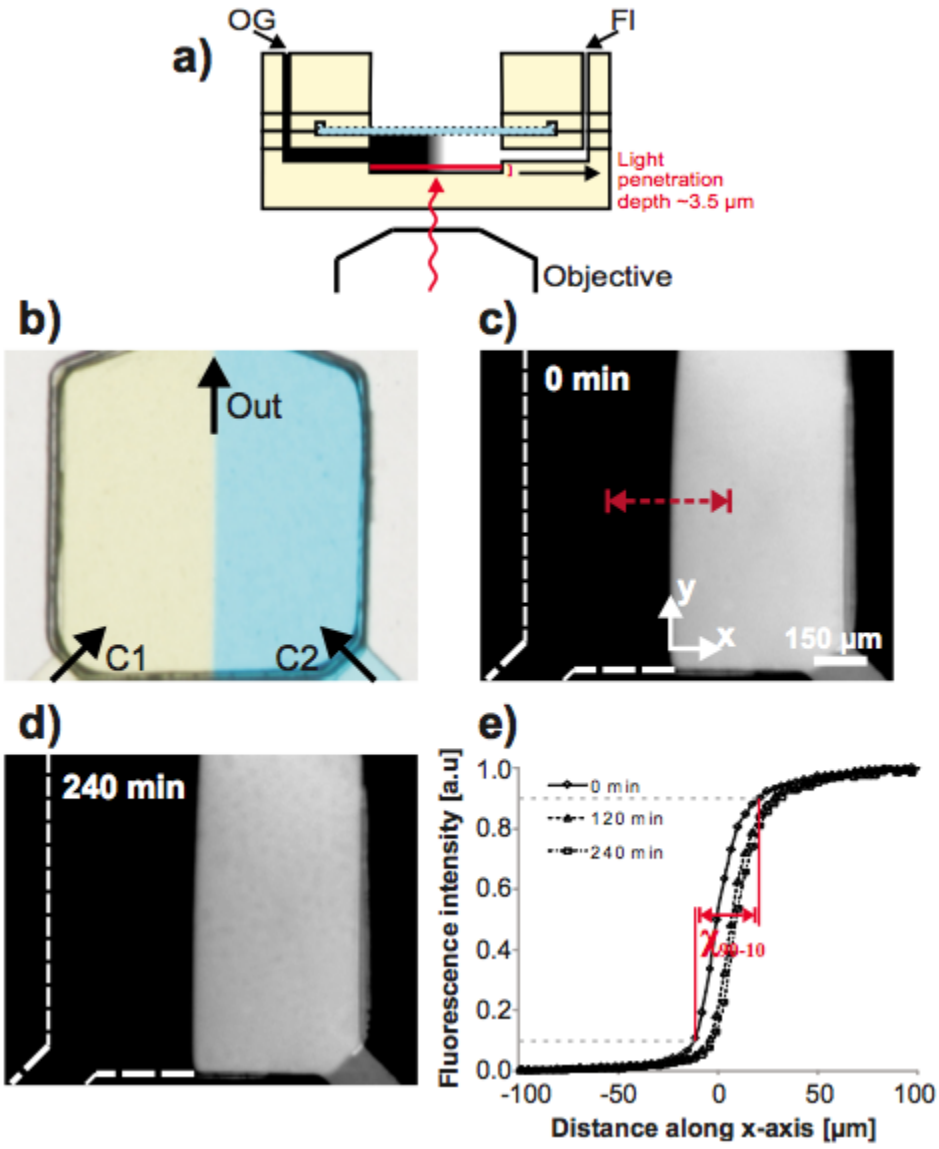

Figure 2.23: Gradient stability analysis using surface-fluorescence microscopy. (a) A cross-sectional schematic showing the configuration of our device and imaging method. The excitation light is attenuated by the addition of a non-fluorescent dye, Orange G. Emission light from fluorescein is collected from approximately 3.5 µm to gain a surface-fluorescence image at the base of the microchannels[24]. (b) A photograph showing the configuration of laminar streams flowing beneath the membrane. Surface-fluorescence images at t = 0 and t = 240 min demonstrate stability in the location of the gradient. (e) Fluorescence intensity profiles of the surface fluorescence gradient show a gradient with of ($X_{90\text{-}10}$ = 33 µm).

Application of a sharp gradients to cells using live-cell florescent stains

Live-cell fluorescent dyes Cell Tracker Green (CMFDA) and Cell Tracker Orange (CMRA) were used in laminar flows to demonstrate a gradient of uptake in the cell-permeable dyes. Cell Tracker dyes are non-fluorescent until they enter cells after which they react with intracellular esterases to produce fluorescent and cell impermeable products. By pressurizing both inlets equally, we attempted to create two symmetric, but distinct fluorescent regions beneath the membrane, eliciting a sharp gradient in the center of the channel parallel to the direction of flow (**Figure 2.24(a)**). For the experiment, fibroblasts suspended in phenol red-free media were plated on the membrane in the open well of the device. Cells were allowed 3-4 h to attach and spread (**Figure 2.24(b)**). Cell Tracker gradients were applied for 30 min to the cells via the underlying microfluidic channels. **Figure 2.24(c)** shows the result of staining cells with a gradient of Cell Tracker Green. Fluorescence intensity profile scans along the numbered lines demonstrate that the underlying gradient region containing Green Cell Tracker was delivered across the membrane to attached cells; no fluorescence attributable to green tracer was observed above the background in the unlabeled region (**Figure 2.24(d)**). The complementary pattern was for the Cell Tracker Orange gradient (**Figure 2.24(e)**). An overlay of the two images highlights a narrow band of yellow colored (inset of **Figure 2.24(e)**) representing the sharp gradients of both fluorescent dyes. The observed diffusion distance, or gradient width, corresponds to 10–20 μm, approximately 1–2 cell diameters. This experiment demonstrates that sharp gradients can be precisely delivered onto cultured cells across a membrane boundary.

The width of the uptake gradient (10–20 μm) agrees well with our experiments with fluorescein ($X_{90\text{-}10}$ = 33 μm), which is a faster-diffusing molecule than Orange or Green Cell Tracker (the media, the device, and the inlet pressurization were the same in

both experiments). These results can be partially explained by considering that fluorescein (376 Da) is smaller than either Orange (550 Da) or Green (464 Da) Cell Tracker and should diffuse further in the same amount of time. In addition, when fibroblasts are seeded and spread, they flatten and should partially or completely block membrane pores, limiting or eliminating fluorescent probe diffusion. To validate this model, the diffusion distance of a single Green Cell Tracker molecule was estimated using δ, the free-diffusion distance $\left(\delta = (2Dt)^{1/2}\right)$, where D is the diffusion coefficient of the Green Cell Tracker[59] ($D = 3.4\times10^{-8}$ cm^2 s^{-1}) and t equals 30 min (duration of the flow applied). From the equation, the diffusion distance of a single molecule is approximately 110 μm, well above the width observed in the cell staining gradient (10–20 μm). This can be explained by the fact that the pores of the track-etched membrane are vertical to the direction of the gradient and inhibit lateral diffusion through the membrane. Therefore the observed cell staining gradient width is a result of the mixing in the laminar flows before transport through the pores. Additionally, this result suggests that the fibroblast cell layer seals the pores and limits lateral diffusion of reagents in the cell culture bath over time.

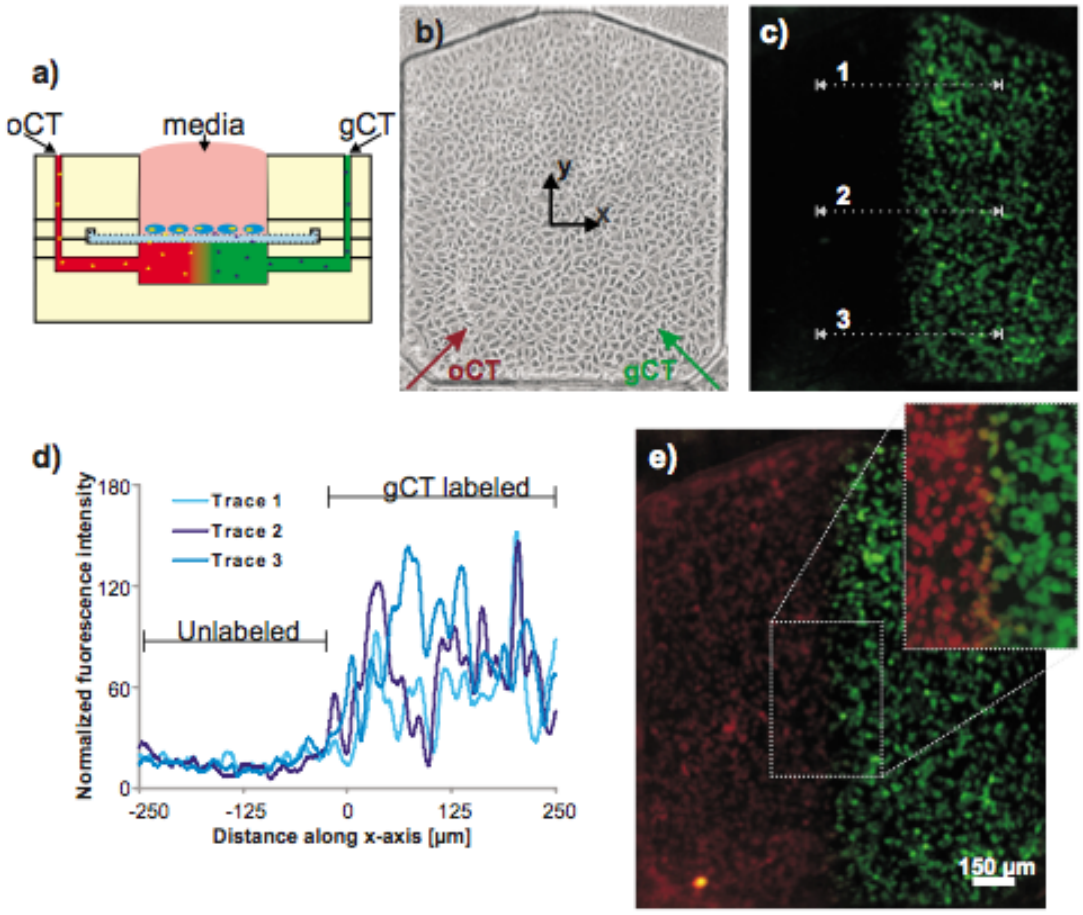

Figure 2.24: Staining of fluorescent gradients in an open cell culture device. (a) A cross-sectional schematic of the device with an accessible open well for cell culture and underlying microfluidic channels. Microchannels were used to deliver a opposing gradients of orange Cell Tracker (oCT) and green Cell Tracker (gCT) (b) A phase-contrast microscopy image of fibroblasts cultured on the surface of a track-etched PET membrane in the well. (c) A epi-fluorescence image of fibroblasts showing the staining with gCT after 30 min. (d) Fluorescence intensity profiles taken from the corresponding locations in (c). (e) A composite image showing the uptake of both oCT and gCT dye delivered by laminar flow beneath the cells cultured on the membrane. The insert is an enlargement of the narrow region between streams in which diffusive mixing produces a sharp 10-20 µm gradient between complimentary dyes.

2.7.2 Summary and assessment of the method

In summary, we have demonstrated that our device is capable of delivering stable gradients with steep interfaces to the basal surface of cultured cells. The device design also facilitates conventional cell culture through an accessible open well. Lastly, we have demonstrated the successful uptake of live-cell fluorescent dyes by cells cultured atop a membrane interface. Although in these experiments we used a two-channel system for gradient generation, more complex arrays can be easily integrated, including 3D networks capable of delivering multiple signaling factors simultaneously. At the time of publication, this work demonstrated the first example of an open-access microfluidic device utilizing a track-etched membrane for delivery of gradients.

2.8 SUMMARY

2.8.1 Microfluidic automation: from integrated systems to modular design

Microfluidic large scale integration describes the use of monolithic PDMS fabrication to generate devices with a high-density of elastomeric microvalves for high-throughput and combinatorial assays[1,60–62] . While this approach (demonstrated in **Section 2.2**) has received much attention by the microfluidics community, its complexity of fabrication and operation has led to an alternative school of thought in which designs are more inspired by multi-well plate methods that are familiar to biologists[8–10,12,63]. These designs have the advantage of a standardized format[8,63], compatibility with existing tools[9], and simplified operation with manual[7] or automated pipetting[10]. However, these designs lack the precise spatial and temporal control possible with microvalves such as demonstrated by the multi-purpose perfusion device[39] (**Section 2.2**) and our micro-dispenser device[45] (**Section 2.5**).

A significant disadvantage of fully integrated systems is the complexity of device apparatus and micro-to-macro connectivity as shown in **Figure 2.25**. Typical devices

like these are cumbersome when they must travel between laminar flow hoods, incubators, and microscopy stations for cell culture studies. To address this problem we developed a modular PDMS microvalve controller[64] (**Section 2.4**) in order to separate the cell culture and fluid handling components. Additionally, we were able to demonstrate interfacing between PDMS and other hard thermoset materials that are more commonly found in cell culture vessels. Further work could extend the modular platform to interface microvalve controllers with cell culture microchannels that are configured in standardized arrays as demonstrated by Beebe et al.[11]. Further work ongoing in the Folch lab, aims to merge the multi-well plate format with automated microvalve systems for facilitating portability and user operation.

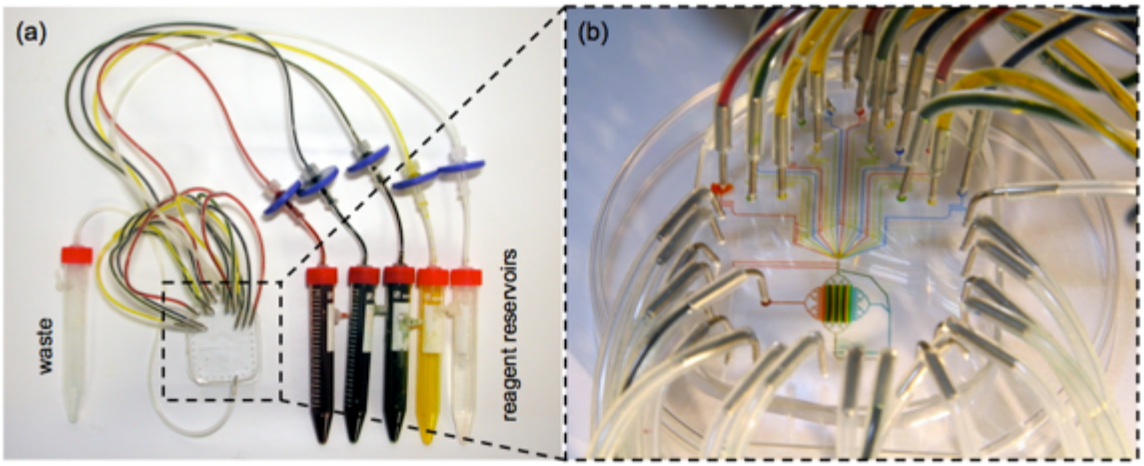

Figure 2.25: Micro-to-macro interfacing of integrated microfluidic devices. (a) While the microfluidic device is compact, the off-chip apparatus includes many interconnections between tubing, reservoirs, and valve controllers (not shown). (b) A close-up of the device showing the connectivity of the valve control lines and perfusion inlets.

2.8.2 Interfacing microfluidics with cell cultures

The vacuum-sealing stacked flow device (**Section 2.6**) demonstrated how modularity could facilitate conventional cell culture technique. The stack flow principle also exerts minimal shear stress making it well suited for unbiased studies of chemotaxis.

The membrane-based device (**Section 2.7**) facilitated cell culture with an open well and reduced shear stress by isolating cells from microfluidic flow. In comparison to the stacked-flow device, the membrane-based device is simpler to operate because the vacuum source is eliminated. However, by integrating the cell culture, the membrane-based device loses modularity. The image-contrast is also reduced because cells are grown on the membrane as shown in **Figure 2.26**.

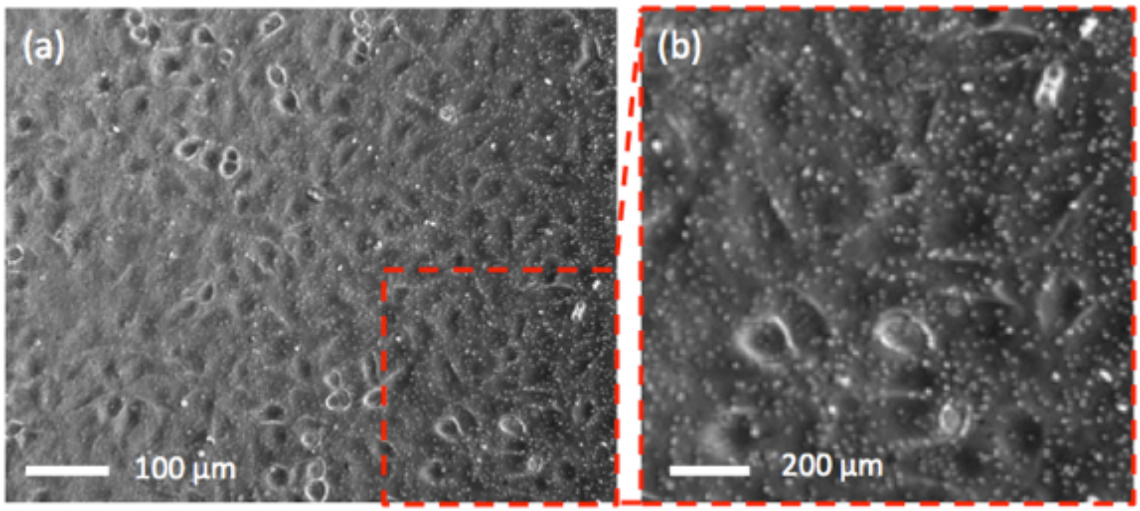

Figure 2.26: Image contrast of cells grown on a track-etched membrane. (a) A large-area and (b) close-up view of the cell culture taken with phase-contrast imaging. The individual pores are visible and contribute to poor contrast.

2.8.3 Conclusions

In this chapter, we explored several microfluidic designs to generate gradients for cell culture. Modular and membrane-based methods were investigated to reduce shear stress and facilitate conventional cell culture technique. In the following chapter, the development of a robust silane coupling method will be described for integrating porous membranes with PDMS. The devices described here were attempts to solve the technical limitations inherent to microfluidic devices and interfacing with cell cultures. Ultimately, the insight gained from these endeavors led to the development of the device

described **Chapter 4** in which we combine modular microfluidics with porous membranes-based gradient generation.

2.9 REFERENCES

1. Thorsen T, Maerkl SJ, Quake SR. Microfluidic Large-Scale Integration. *Science*. 2002;298(5593):580–584.

2. Berthier E, Young EWK, Beebe D. Engineers are from PDMS-land, Biologists are from Polystyrenia. *Lab Chip*. 2012;12(7):1224.

3. Cheong R, Paliwal S, Levchenko A. High content screening in microfluidic devices. *Expert Opin Drug Discov*. 2010;5(8):715–720.

4. Young EWK, Berthier E, Guckenberger DJ, Sackmann E, Lamers C, Meyvantsson I, Huttenlocher A, Beebe DJ. Rapid Prototyping of Arrayed Microfluidic Systems in Polystyrene for Cell-Based Assays. *Anal Chem*. 2011;83(4):1408–1417.

5. Wang Y, Balowski J, Phillips C, Phillips R, Sims CE, Allbritton NL. Benchtop micromolding of polystyrene by soft lithography. *Lab Chip*. 2011;11(18):3089–3097.

6. Meyvantsson I, Beebe DJ. Cell Culture Models in Microfluidic Systems. *Annu Rev Anal Chem*. 2008;1(1):423–449.

7. Walker GM, Beebe DJ. A passive pumping method for microfluidic devices. *Lab Chip*. 2002;2(3):131.

8. Berthier E, Surfus J, Verbsky J, Huttenlocher A, Beebe D. An arrayed high-content chemotaxis assay for patient diagnosis. *Integr Biol*. 2010;2(11-12):630–638.

9. Yu H, Alexander CM, Beebe DJ. A plate reader-compatible microchannel array for cell biology assays. *Lab Chip*. 2007;7(3):388–391.

10. Meyvantsson I, Warrick JW, Hayes S, Skoien A, Beebe DJ. Automated cell culture in high density tubeless microfluidic device arrays. *Lab Chip*. 2008;8(5):717–724.

11. Puccinelli JP, Su X, Beebe DJ. Automated High-Throughput Microchannel Assays for Cell Biology: Operational Optimization and Characterization. *J Assoc Lab Autom*. 2010;15(1):25–32.

12. McKenna BK, Evans JG, Cheung MC, Ehrlich DJ. A Parallel Microfluidic Flow Cytometer for High Content Screening. *Nat Methods*. 2011;8(5):401–403.

13. Diao J, Young L, Kim S, Fogarty EA, Heilman SM, Zhou P, Shuler ML, Wu M, DeLisa MP. A three-channel microfluidic device for generating static linear gradients and its application to the quantitative analysis of bacterial chemotaxis. *Lab Chip*. 2006;6(3):381.

14. Cheng S-Y, Heilman S, Wasserman M, Archer S, Shuler ML, Wu M. A hydrogel-based microfluidic device for the studies of directed cell migration. *Lab Chip*. 2007;7(6):763.

15. Bang H, Lee WG, Park J, Yun H, Lee J, Chung S, Cho K, Chung C, Han DC, Chang JK. Active sealing for soft polymer microchips: method and practical applications. *J Micromechanics Microengineering*. 2006;16:708.

16. Chung BG, Park JW, Hu JS, Huang C, Monuki ES, Jeon NL. A hybrid microfluidic-vacuum device for direct interfacing with conventional cell culture methods. *Bmc Biotechnol*. 2007;7(1):60.

17. Schaff UY, Xing MMQ, Lin KK, Pan N, Jeon NL, Simon SI. Vascular mimetics based on microfluidics for imaging the leukocyte?endothelial inflammatory response. *Lab Chip*. 2007;7(4):448.

18. Barkefors I, Thorslund S, Nikolajeff F, Kreuger J. A fluidic device to study directional angiogenesis in complex tissue and organ culture models. *Lab Chip*. 2009;9(4):529.

19. Walker GM, Sai J, Richmond A, Stremler M, Chung CY, Wikswo JP. Effects of flow and diffusion on chemotaxis studies in a microfabricated gradient generator. *Lab Chip*. 2005;5(6):611–618.

20. Zhang Z, Zhao P, Xiao G. The fabrication of polymer microfluidic devices using a solid-to-solid interfacial polyaddition. *Polymer*. 2009;50(23):5358–5361.

21. Lee NY, Chung BH. Novel Poly(dimethylsiloxane) Bonding Strategy via Room Temperature “Chemical Gluing.” *Langmuir*. 2009;25(6):3861–3866.

22. Dertinger SKW, Chiu DT, Jeon NL, Whitesides GM. Generation of gradients having complex shapes using microfluidic networks. *Anal Chem*. 2001;73(6):1240–1246.

23. Keenan TM, Hsu C-H, Folch A. Microfluidic “jets” for generating steady-state gradients of soluble molecules on open surfaces. *Appl Phys Lett*. 2006;89(11):114103.

24. Bancaud A, Wagner G, Dorfman KD, Viovy JL. Measurement of the surface concentration for bioassay kinetics in microchannels. *Anal Chem*. 2005;77(3):833–839.

25. Bhattacharjee N, Li N, Keenan TM, Folch A. A neuron-benign microfluidic gradient generator for studying the response of mammalian neurons towards axon guidance factors. *Integr Biol*. 2010;2(11-12):669.

26. Keenan TM, Folch A. Biomolecular gradients in cell culture systems. *Lab Chip*. 2008;8(1):34.

27. Ahmed T, Shimizu TS, Stocker R. Microfluidics for bacterial chemotaxis. *Integr Biol*. 2010;2(11-12):604.

28. Mohammed JS, Caicedo HH, Fall CP, Eddington DT. Microfluidic add-on for standard electrophysiology chambers. *Lab Chip*. 2008;8(7):1048.

29. Keenan TM, Frevert CW, Wu A, Wong V, Folch A. A new method for studying gradient-induced neutrophil desensitization based on an open microfluidic chamber. *Lab Chip*. 2010;10(1):116.

30. Taylor AM, Rhee SW, Tu CH, Cribbs DH, Cotman CW, Jeon NL. Microfluidic Multicompartment Device for Neuroscience Research. *Langmuir*. 2003;19(5):1551–1556.

31. Taylor AM, Blurton-Jones M, Rhee SW, Cribbs DH, Cotman CW, Jeon NL. A microfluidic culture platform for CNS axonal injury, regeneration and transport. *Nat Methods*. 2005;2(8):599–605.

32. Taylor AM, Berchtold NC, Perreau VM, Tu CH, Li Jeon N, Cotman CW. Axonal mRNA in uninjured and regenerating cortical mammalian axons. *J Neurosci*. 2009;29(15):4697.

33. Taylor AM, Dieterich DC, Ito HT, Kim SA, Schuman EM. Microfluidic Local Perfusion Chambers for the Visualization and Manipulation of Synapses. *Neuron*. 2010;66(1):57–68.

34. Juncker D, Schmid H, Delamarche E. Multipurpose microfluidic probe. *Nat Mater*. 2005;4(8):622–628.

35. Queval A, Ghattamaneni NR, Perrault CM, Gill R, Mirzaei M, McKinney RA, Juncker D. Chamber and microfluidic probe for microperfusion of organotypic brain slices. *Lab Chip*. 2010;10(3):326.

36. Qasaimeh MA, Gervais T, Juncker D. Microfluidic quadrupole and floating concentration gradient. *Nat Commun*. 2011;2:464.

37. Ainla A, Jansson ET, Stepanyants N, Orwar O, Jesorka A. A Microfluidic Pipette for Single-Cell Pharmacology. *Anal Chem*. 2010;82(11):4529–4536.

38. Hsu C-H, Chen C, Folch A. Microcanals for micropipette access to single cells in microfluidic environments. *Lab Chip*. 2004;4(5):420.

39. Cooksey GA, Sip CG, Folch A. A multi-purpose microfluidic perfusion system with combinatorial choice of inputs, mixtures, gradient patterns, and flow rates. *Lab Chip*. 2009;9(3):417.

40. Metz S, Jiguet S, Bertsch A, Renaud P. Polyimide and SU-8 microfluidic devices manufactured by heat-depolymerizable sacrificial material technique. *Lab Chip*. 2004;4(2):114–120.

41. Luo C, Govindaraju A, Garra J, Schneider T, White R, Currie J, Paranjape M. Releasing SU-8 structures using polystyrene as a sacrificial material. *Sensors Actuators Phys*. 2004;114(1):123–128.

42. Abgrall P, Charlot S, Fulcrand R, Paul L, Boukabache A, Gué A-M. Low-stress fabrication of 3D polymer free standing structures using lamination of photosensitive films. *Microsyst Technol*. 2008;14(8):1205–1214.

43. Cheng MC, Gadre AP, Garra JA, Nijdam AJ, Luo C, Schneider TW, White RC, Currie JF, Paranjape M. Dry release of polymer structures with anti-sticking layer. *J Vac Sci Technol Vac Surfaces Films*. 2004;22(3):837.

44. Sip CG, Bhattacharjee N, Folch A. A modular cell culture device for generating arrays of gradients using stacked microfluidic flows. *Biomicrofluidics*. 2011;5(2):022210–9.

45. Sip CG, Folch A. An open-surface micro-dispenser valve for the local stimulation of conventional tissue cultures. In: *MicroTAS 2010. Proceedings of the 14th International Conference on Miniaturized Systems for Chemistry and Life Sciences. Groningen, The Netherlands*.; 2010.

46. Kim T, Pinelis M, Maharbiz MM. Generating steep, shear-free gradients of small molecules for cell culture. *Biomed Microdevices*. 2008;11(1):65–73.

47. Kim S, Kim HJ, Jeon NL. Biological applications of microfluidic gradient devices. *Integr Biol*. 2010;2(11-12):584.

48. Ahmed T, Shimizu TS, Stocker R. Microfluidics for bacterial chemotaxis. *Integr Biol*. 2010;2(11-12):604.

49. Li C-W, Chen R, Yang M. Generation of linear and non-linear concentration gradients along microfluidic channel by microtunnel controlled stepwise addition of sample solution. *Lab Chip*. 2007;7(10):1371–1373.

50. Shamloo A, Ma N, Poo M, Sohn LL, Heilshorn SC. Endothelial cell polarization and chemotaxis in a microfluidic device. *Lab Chip*. 2008;8(8):1292.

51. Atencia J, Morrow J, Locascio LE. The microfluidic palette: A diffusive gradient generator with spatio-temporal control. *Lab Chip*. 2009;9(18):2707.

52. Mosadegh B, Huang C, Park JW, Shin HS, Chung BG, Hwang S-K, Lee K-H, Kim HJ, Brody J, Jeon NL. Generation of Stable Complex Gradients Across Two-Dimensional Surfaces and Three-Dimensional Gels. *Langmuir*. 2007;23(22):10910–10912.

53. Abhyankar VV, Toepke MW, Cortesio CL, Lokuta MA, Huttenlocher A, Beebe DJ. A platform for assessing chemotactic migration within a spatiotemporally defined 3D microenvironment. *Lab Chip*. 2008;8(9):1507–1515.

54. Abhyankar VV, Lokuta MA, Huttenlocher A, Beebe DJ. Characterization of a membrane-based gradient generator for use in cell-signaling studies. *Lab Chip*. 2006;6(3):389.

55. Chueh B, Huh D, Kyrtsos CR, Houssin T, Futai N, Takayama S. Leakage-Free Bonding of Porous Membranes into Layered Microfluidic Array Systems. *Anal Chem*. 2007;79(9):3504–3508.

56. De Jong J, Lammertink RGH, Wessling M. Membranes and microfluidics: a review. *Lab Chip*. 2006;6(9):1125.

57. Kim T, Pinelis M, Maharbiz MM. Generating steep, shear-free gradients of small molecules for cell culture. *Biomed Microdevices*. 2008;11(1):65–73.

58. Aran K, Sasso LA, Kamdar N, Zahn JD. Irreversible, direct bonding of nanoporous polymer membranes to PDMS or glass microdevices. *Lab Chip*. 2010;10(5):548.

59. Wartenberg M, Dönmez F, Ling FC, Acker H, Hescheler J, Sauer H. Tumor-induced angiogenesis studied in confrontation cultures of multicellular tumor spheroids and embryoid bodies grown from pluripotent embryonic stem cells. *Faseb J*. 2001;15(6):995–1005.

60. King KR, Wang S, Irimia D, Jayaraman A, Toner M, Yarmush ML. A high-throughput microfluidic real-time gene expression living cell array. *Lab Chip*. 2006;7(1):77–85.

61. Melin J, Quake SR. Microfluidic Large-Scale Integration: The Evolution of Design Rules for Biological Automation. *Annu Rev Biophys Biomol Struct*. 2007;36(1):213–231.

62. Kamei K, Takahashi H, Shu CJ, Wang X, He GW, Silverman R, Radu CG, Witte ON, Lee K-B, Tseng H-R. Integrated microfluidic devices for combinatorial cell-based assays. *Biomed Microdevices*. 2009;11(3):547–555.

63. Irimia D, Toner M. Spontaneous migration of cancer cells under conditions of mechanical confinement. *Integr Biol*. 2009;1(8-9):506–512.

64. Skafte-Pedersen P, Sip CG, Folch A, Dufva M. Modular microfluidic systems using reversibly attached PDMS fluid control modules. *J Micromechanics Microengineering*. 2013;23(5):055011.

Chapter 3: Stable chemical bonding of porous membranes and PDMS devices for long-term cell culture

3.1 INTRODUCTION

The integration of commercially available track-etched membranes in microfluidic devices has experienced growing interest because these materials offer well-defined nano- or micro-pore structures in a monolithic material[1–3]. Poly (ethylene terephthalate) (PET) track-etched membranes are available in a transparent format that is especially useful for microscopy and live-cell observation. A variety of cell-based devices have been designed to spatially control delivery of reagents to cells, e.g., to apply gradients for chemotaxis[4], control differentiation[5,6], or compartmentalize cell co-cultures[7,8]. Across these studies a variety of techniques have been reported for integrating track-etched membranes with microfluidic layers. Techniques include sandwiching between plasma bonded PDMS layers[4,9–11], using adhesives[12–14], PDMS gluing[8,15,16], SiO_2 sputtering[5,17], and silane coupling[7,18].

Silane coupling is an attractive technique because the process uses commercially available reagents, works well with polymers whose surfaces can be hydroxylated, is uniformly applied to surfaces (thus tends to be feature-independent), and is compatible with familiar oxygen plasma-bonding steps. In contrast to the sandwiching technique[4,9–11], silane coupling permits open-surface devices through bonding of only one side of a membrane. Furthermore, PDMS gluing and the use of adhesives pose limitations on feature-size due to problems with leakage or contamination of high-resolution structures. SiO_2 sputtering relies on expensive and specialized equipment that limits its widespread use. Silane coupling has an extensive history for the coupling of dissimilar materials[19] and several groups have reported on methods using (3-Aminopropyl)triethoxysilane (APTES) modification of plastics to achieve bonding with PDMS[20–22]. Similarly, Lee and

Ram demonstrated the enhanced stability of plastic-PDMS bonding using thick layers of dipodal silane[23]. The Zahn group first reported the modification of porous polymer membranes with APTES for integration with PDMS device layers[18]. Encouraged by these reports, we evaluated bonding methods for the fabrication of cell culture devices incorporating porous membranes. We found that while APTES modification yields immediate bond formation and stability when stored in water, rapid bond degradation occurs when immersed in a common cell culture medium. This failure in cell culture medium can be explained by the salt cations having a catalytic effect on the dissociation of Si-O bonds within the silane interface[24].

To find a solution, we tested a variety of silane preparations for their ability to bond PET track-etched membranes and PDMS. We tested formulations of a variety of trialkoxysilanes and dipodal silanes to determine a combination of organofunctional group, cross-link density, solvent, and catalyst for effective bond stability in cell culture medium. From this testing we have found a robust silane modification process and applied this method to demonstrate unique functionality of integrated track-etched membranes and PDMS devices for cell culture.

3.2 Materials and Methods

3.2.1 Materials

The silanes bis[3-(trimethoxysilyl)propyl]amine (bis-amino silane), bis[3-(triethoxysilyl)propyl] tetrasulfide (bis-sulfur silane), 1,2-Bis(trimethoxysilyl)ethane (bis-ethane), (3-Aminopropyl)triethoxysilane (APTES), (3-Glycidyloxypropyl)-trimethoxysilane (epoxy silane), and tetrabutyl titanate (TBT) and diisopropylamine were purchased from Sigma-Aldrich (St. Louis, MO). Transparent PET track-etched membranes with 0.4 μm pore diameter and 2×10^6 pores cm^{-2} in either 13 mm or 25 mm

diameters were purchased from AR Brown-US (Pittsburgh, PA). DMEM cell culture medium (11995), fetal bovine serum (10082), penicillin-streptomycin (10378016), Hank's balanced salt solution (HBSS, 14025), and calcein AM (C3100MP) were obtained from Life Technologies (Grand Island, NY). Matrigel (356234) was purchased from BD Biosciences (San Jose, CA).

3.2.2 Silane treatment of PET track-etched membranes

We assayed various silane formulations in order to determine their effectiveness for bonding PET membranes with PDMS. In general, membranes were secured by their edge using a PDMS block and positioned upright when treated with oxygen plasma for 60 sec at 60 W, 670 mTorr, and 40 kHz (Zepto plasma system, Diener Electronic, Germany). After plasma oxidation membranes were then submerged in prepared silane mixtures for 20 min at 80 °C on a hotplate. After treatment with silane, the membranes were rinsed with copious IPA and cured for 30 min at 70 °C in a convection oven. Membranes were then immersed in 70% ethanol for 30 min to render the surface hydrophilic. PDMS slabs were treated with oxygen plasma then bonded to membranes by conformal contact. Bonded pieces were then allowed to cure for 1 hour at 70 °C. A generalized reaction scheme for the optimal bonding strategy with 2% bis-amino silane and 1 % water in IPA is shown in **Figure 3.1**. To evaluate bond stability, bonded PDMS-PET samples were prepared in quadruplicate for each silane formulation and submerged in DMEM at 37 °C. Delamination was observed by gently lifting the membrane out of the DMEM after 1 day and 2 weeks.

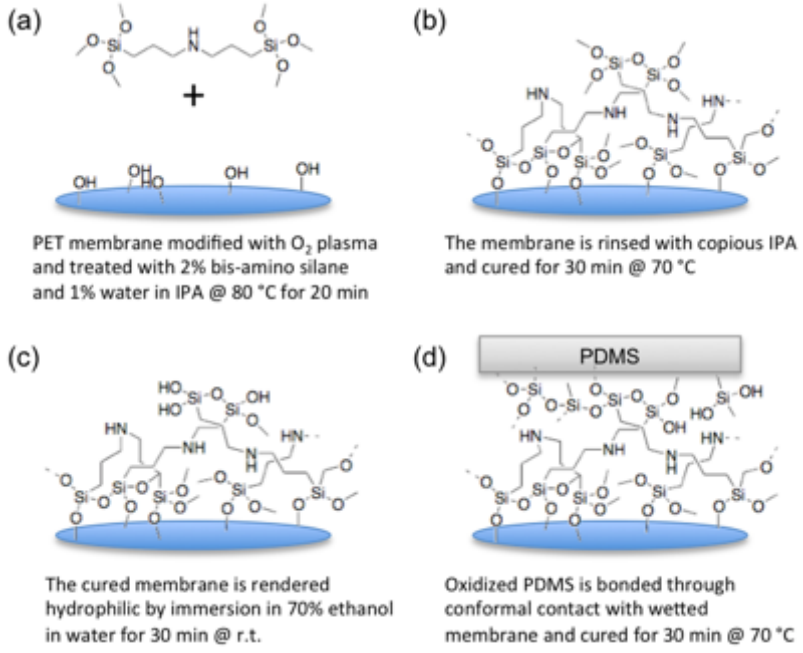

Figure 3.1: Schematic of the idealized surface modification reaction between PET membranes and bis-amino silane. (a) An oxidized PET membrane is a substrate for the condensation of bis-amino silane at elevated temperature. (b) After the condensation reaction, residual unbound silane is rinsed and the substrate is cured in order to further cross-link the silane layer. (c) The modified membrane is submerged in a 70% ethanol in water solution to hydrate the surface and expose hydroxyl groups. (d) Oxidized PDMS bonds readily to the wetted membrane. Complete bonding occurs when the surface is dried and baked.

3.2.3 X-ray photoelectron spectroscopy analysis

Samples of untreated, oxygen plasma treated, freshly silane-modified, and degraded silane-modified membranes were analyzed with XPS (Kratos Axis Ultra DLD, Kratos Analytical Inc., NY) to determine the average elemental compositions. 3 spots of 700 × 300 μm^2 area per sample were analyzed with survey scans to quantify the C 1s and O 1s peaks at a resolution of 1 eV. Detailed scans were used for analysis of the N 1s and Si 2p spectra at a resolution of 0.3 eV. Samples were analyzed at an angle of 0° with respect to the normal of the surface. Photoelectrons were detected from a depth of

approximately 10 nm. Silane modification of membranes with 2% bis-amino, 1% water, in IPA or 2% APTES in water was done as previously described. For freshly prepared samples, membranes were modified with silane, dried, and then analyzed with XPS. For degraded silane-modified samples, membranes were modified then submerged in water, HBSS, or DMEM for 18.5 hours before rinsing, drying, and analysis with XPS.

3.2.4 Fabrication of open-surface PDMS-PET membrane device

For proof-of-concept we designed a simple open-surface PDMS-PET membrane device for the basal-side stimulation of cell cultures as shown in **Figure 3.4(a-b)**. In order to achieve high quality imaging of cells, the device was fabricated using 400 μm thick PDMS replicas that were micromolded from SU-8 patterned silicon masters by exclusion molding technique[25]. The PDMS replicas were plasma-bonded to cover glass-bottom 55 mm dishes (#60-30-1-N, In Vitro Scientific, Sunnyvale, CA) for a self-contained cell culture format. Plasma-oxidized track-etched PET membranes were treated with 2% bis-amino silane in 1% water and IPA as previously described. After treatment, curing, and soaking in 70% ethanol and water solution, the silane-modified membranes were brought into conformal contact with the device consisting of the PDMS replica and 55 mm dish. Bonding while the membranes are slightly wetted with 70% ethanol solution enhances wrinkle-free assembly. After drying with an air gun, the assembly was baked for 30 min at 70 °C to complete the bonding. Vias were produced by removing the membrane with dissection tweezers at the location of the inlets and outlets of the underlying microchannels. Finally, inlet and outlet ports were plasma bonded to complete the device assembly.

3.2.5 C2C12 cell culture and calcein AM stimulation

Assembled PDMS-PET membrane devices were coated with a 1:50 dilution of Matrigel for 30 min at 37 °C. C2C12 myoblasts (American Type Culture Collection, Manassas, VA) were uniformly seeded onto the coated devices and maintained in DMEM with 20% fetal bovine serum and 1% penicillin-streptomycin until they achieved confluence after approximately 1 week in culture. "Serum starvation" (changing the serum conditions to 2% horse serum) induced myotube differentiation over the course of an additional week of culture[26]. Calcein AM was prepared in Hank's Balanced Salt Solution at 0.5 μM concentration and loaded into cells through the microchannels for 15 min before imaging.

3.3 Results and Discussion

3.3.1 Evaluation of different silanes treatment for bond stability in DMEM at 37 °C

In order to determine an effective strategy for bonding PET membranes with PDMS we assayed different formulations of 2% silane while varying the following parameters of the silane formulations: (1) trialkoxysilanes or dipodal silanes, (2) catalyst, (3) organofunctional group, and (4) reaction solvent. For the first set of silane formulations shown in **Table 3.1**, we tested formulations using APTES and the dipodal silane bis[3-(trimethoxysilyl)propyl]amine (referred to herein as bis-amino silane) with polar protic solvents and different catalysts. For treatments **1**-**3** we used 100% water as choice of solvent and catalyst to compare the classic APTES and amine-epoxy methods with the bis-amino silane. None of the formulations with 100% water as a solvent produced stable bonds in DMEM after 2 weeks. In addition, the bis-amino formulation for treatment **2** was unstable and rapidly polymerized. The instability can be explained by the difference in number of alkoxysilane groups per molecule of silane. Compared to APTES, the bis-amino silane has twice the number of reactive groups and a flexible

C_3H_6-NH-C_3H_6 chain that promotes crosslinking. While hydrolysis of the alkoxysilane to Si-OH must occur before the condensation of a silane molecule on the PET surface, too many hydrolyzed Si-OH groups can result in polymerization or precipitation for a dipodal silane. Similarly, too much water present can inhibit the growth of the silane layer by hydrolysing the C-O-Si bonds before the silane molecules and the substrate can generate a stable layer. Therefore, we assayed solution stability for the bis-amino silane and APTES in different concentrations of water and isopropyl alcohol (IPA). We found that solutions of 2% bis-amino silane were stable in IPA with up to 1% water. Greater concentrations resulted in bulk gelation or precipitation. 2% APTES solutions were stable at all concentrations of water and IPA tested.

For treatments **4**-**9** we compared 1% water, 0.5% titanate catalyst (TBT), and no catalyst with either 2% APTES or 2% bis-amino silane. None of the APTES treated samples remained bonded after 1 day of immersion in DMEM at 37 °C. For the bis-amino formulations there was partial bonding of the samples for the TBT catalyzed or un-catalyzed formulations after 2 weeks. Full bonding was realized after 2 weeks in DMEM for treatment **5** with 2% bis-amino silane in 1% water and IPA. Interestingly, treatment **10** also realized full bonding through an amine-epoxy bonding mechanism in which the PET membrane was treated with a solution 2% APTES and 0.5% TBT in IPA and the PDMS sample that was treated with 2% epoxy-silane and 0.5% TBT in IPA. Upon comparison to treatment **3** in which 100% water was used in order to replicate amine-epoxy bonding as reported in the literature, the result of treatment **10** suggests that the amount and type of catalyst used is critical for the silane modification process. While 100% water-based silane treatments may work well for PDMS or glass substrates, the lower concentration of hydroxyl groups on an oxidized PET surface could limit the condensation and surface coverage of the silane layer. The amine-epoxy method was not

improved by the addition of bis-amino silane to promote cross-linking, as demonstrated by the bond failure at 2 weeks for treatment **11**.

Table 3.1: Comparison of APTES and bis-amino silane in polar aprotic solvent

No.	Solvent	Silane	Catalyst	Bond	DMEM 1 day	DMEM 2 weeks
1	water	APTES	100% water	2	0	-
2	water	bis-amino	100% water	2	0	-
3	water	APTES or epoxy	100% water	2	0	-
4	IPA	APTES	1% water	2	0	-
5	IPA	bis-amino	1% water	2	2	2
6	IPA	APTES	0.5% TBT	2	0	-
7	IPA	bis-amino	0.5% TBT	2	2	1
8	IPA	APTES	none	2	0	-
9	IPA	bis-amino	none	2	2	1
10	IPA	APTES or epoxy	0.5% TBT	2	2	2
11	IPA	1:1 bis-amino with APTES or epoxy	0.5% TBT	2	2	0

2: bonded, 1: partial bond failure, 0: total bond failure

A second set of silane formulations was assayed as shown in **Table 3.2** in order to determine if other dipodal silanes could yield stable bonding in the same manner as bis-amino silane. We examined two different dipodal silanes in a variety of reaction conditions meant to determine the influence of catalyst and solution pH. To account for catalytic effects of the amine group the solution was made basic with the addition of 1% diisopropylamine (amine). Surprisingly for treatments **12**-**21** we found delamination after 1 day in DMEM in all samples except for treatment **20**. In some cases there was no bonding even before immersion in DMEM which points to poor condensation or solution reactivity of these silane formulations. These results suggest that the C_3H_6-NH-C_3H_6 organofunctional group of the bis-amino silane is essential to promote condensation of

the silane at the PET surface. Similar findings were reported by Howarter and Youngblood using anhydrous deposition of APTES and other silanes to determine the influence of the amine group; they determined that the amine group must be integral to the silane molecule for the surface reaction to occur[27]. We also tested APTES or bis-amino silane with anhydrous reaction conditions as shown in **Table 3.3**. None of the treatments demonstrated complete bonding after 1 day of immersion in DMEM. Comparing treatments **7** and **9** of Table 1 with their complementary treatments **23** and **25** of Table 2 suggests that a non-polar solvent limits the condensation of the silanes onto the PET surface.

Table 3.2: Comparison of other dipodal silane bonding

No.	Solvent	Silane	Catalyst	Bond	DMEM 1 day	DMEM 2 weeks
12	IPA	bis-ethane	1% water	2	0	-
13	IPA	bis-sulpho	1% water	0	0	-
14	IPA	bis-ethane	0.5% TBT	2	0	-
15	IPA	bis-sulpho	0.5% TBT	2	0	-
16	IPA	bis-ethane	1% amine	2	0	-
17	IPA	bis-sulpho	1% amine	2	0	-
18	IPA	bis-ethane	1% amine, 1 % water	0	0	-
19	IPA	bis-sulpho	1% amine, 1 % water	2	0	-
20	IPA	bis-ethane	1% amine 0.5% TBT	2	1	1
21	IPA	bis-sulpho	1% amine, 0.5% TBT	1	0	-

2: bonded, 1: partial bond failure, 0: total bond failure

Table 3.3: Comparison of APTES and bis-amino silane bonding with anhydrous solvent

No.	Solvent	Silane	Catalyst	Bond	DMEM 1 day	DMEM 2 weeks
22	toluene	APTES	none	2	0	-
23	toluene	bis-amino	none	2	1	0
24	toluene	APTES	0.5% TBT	2	0	-
25	toluene	bis-amino	0.5% TBT	2	0	-

2: bonded, 1: partial bond failure, 0: total bond failure

3.3.2 XPS analysis of surface composition of silane modified PET and degradation of silane layer

The chemical composition of the untreated, oxygen plasma treated, and silane modified PET membranes were determined using XPS analysis (Fig. 2a). The atomic concentration of the untreated PET samples was measured to be 75.4% C and 24.4% O with negligible Si or N content. The oxygen plasma treatment resulted in an increase to 30.3% O with 2% N and 0.5% Si. The slight presence of Si can be attributed to PDMS contamination from within the plasma oven chamber. Notably, samples treated with bis-amino silane resulted in greater than 2 fold increase in the concentrations of silicon and nitrogen when compared to the APTES treatment (Fig. 2a). The effects of different aqueous solutions on the degradation of silane treatments was analysed by measuring the chemical composition with XPS after 18.5 h of immersion at 37 °C. The results in Fig. 2b show that while APTES loses silicon and nitrogen after exposure to DMEM, bis-amino silane treated samples remain relatively unchanged. Example XPS spectra and full elemental composition data is included in supplemental materials **Figure 3.3** and **Table 3.4** and **Table 3.5**

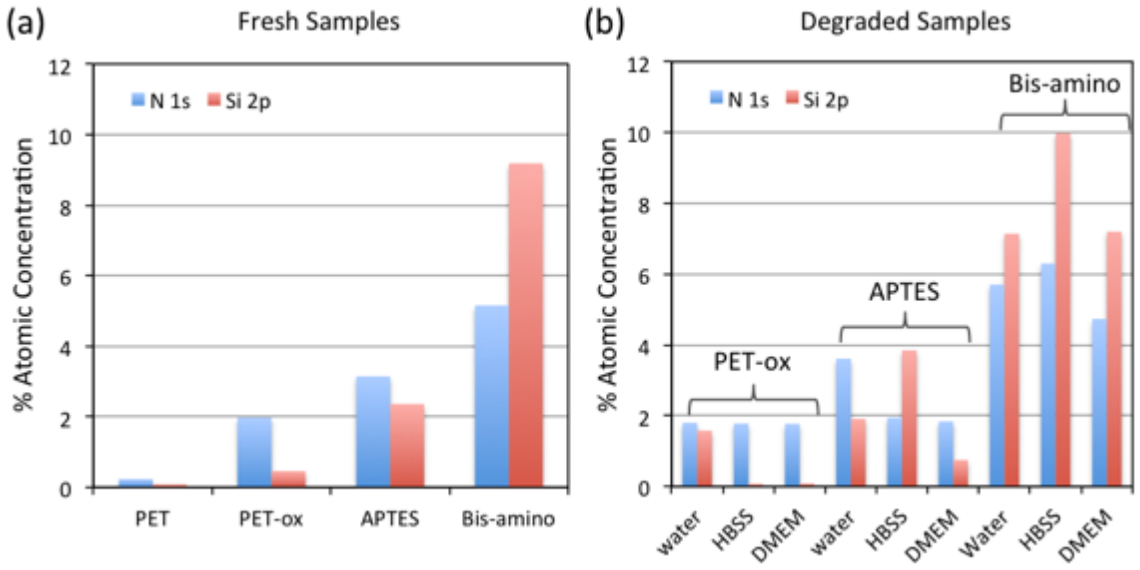

Figure 3.2: XPS elemental composition analysis for silane treated PET samples. (a) Comparison of the nitrogen and silicon atomic concentration derived from XPS analysis of untreated PET track-etched membranes, oxygen plasma treated (PET-ox), APTES treated, and bis-amino treated samples. (b) Comparison of nitrogen and silicon atomic concentration of oxygen plasma treated, APTES, and bis-amino silane treated membranes after degradation by immersion in water, HBSS, or DMEM for 18.5 hours.

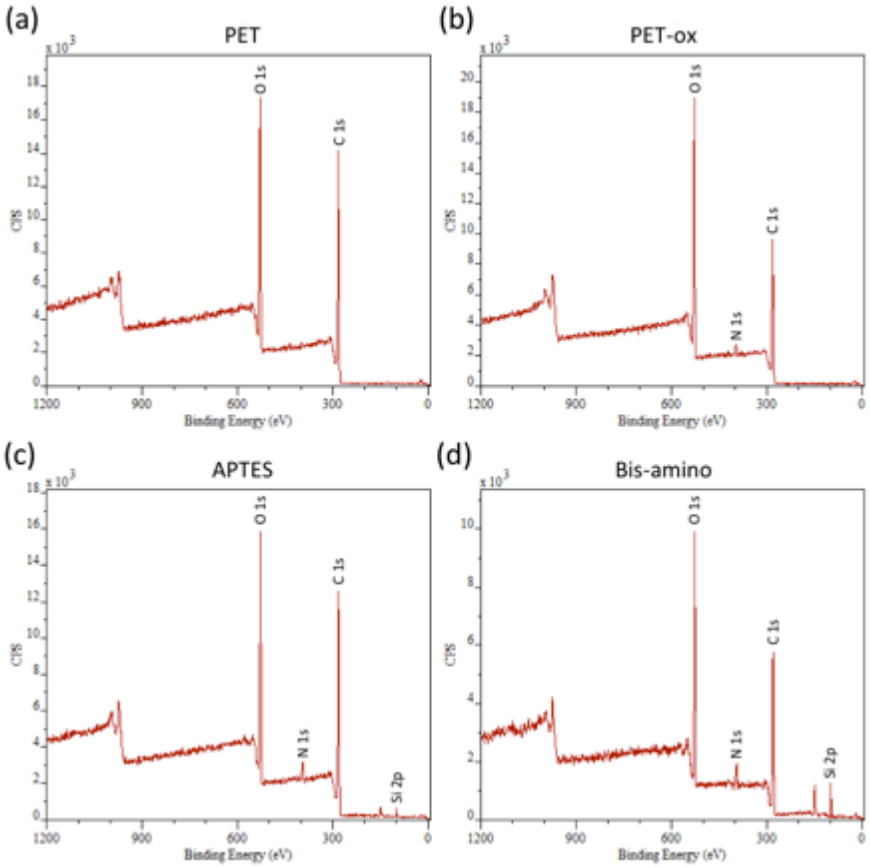

Figure 3.3: Example XPS survey spectra for PET track-etched membranes. (a) untreated, (b) oxygen plasma treated, (c) APTES treated, and (d) bis-amino silane treated PET track-etched membranes.

Table 3.4: Elemental composition for freshly silane treated samples

% At. Conc.	PET	PET-ox	APTES	Bis-amino
C 1s	75.2	67.3	71.1	59.0
O 1s	24.4	30.3	23.4	26.7
N 1s	0.2	2.0	3.1	5.2
Si 2p	0.1	0.5	2.4	9.2

Table 3.5: Elemental composition for freshly silane treated samples

% At. Conc.	PET-ox			APTES			Bis-amino		
	water	HBSS	DMEM	water	HBSS	DMEM	Water	HBSS	DMEM
C 1s	73.0	74.9	74.3	71.4	69.4	74.4	62.4	56.7	61.7
O 1s	23.7	23.2	23.9	23.0	24.8	23.0	23.8	25.1	26.3
N 1s	1.8	1.8	1.8	3.6	1.9	1.8	5.7	6.3	4.7
Si 2p	1.6	0.1	0.1	1.9	3.8	0.7	7.1	10.0	7.2
S 2p	0	0	0	0	0	0	1.0	0.0	0
Cl 2p	0	0	0	0	0	0	0	1.9	0

3.3.3 Demonstration of long-term culture and basal-side stimulation of differentiated myotubes

The optimal treatment of PET membranes with 2% bis-amino silane in 1% water and IPA was used to fabricate an open-surface device for long-term cell culture. We used a simple microfluidic design for the basal-side stimulation of cell cultures as shown in Fig. 3. C2C12 cells were seeded at low density onto the PET membrane surface and allowed to propagate to confluence for 1 week. The cells were differentiated into mytotubes by culturing in differentiating medium for an additional week. To demonstrate stable bonding and operation of the track-etched pores, we operated the device by loading a calcein-AM solution into the microfluidic channel. Cells grown above the microchannels were locally stained as shown in **Fig. 3.4(c-e).**

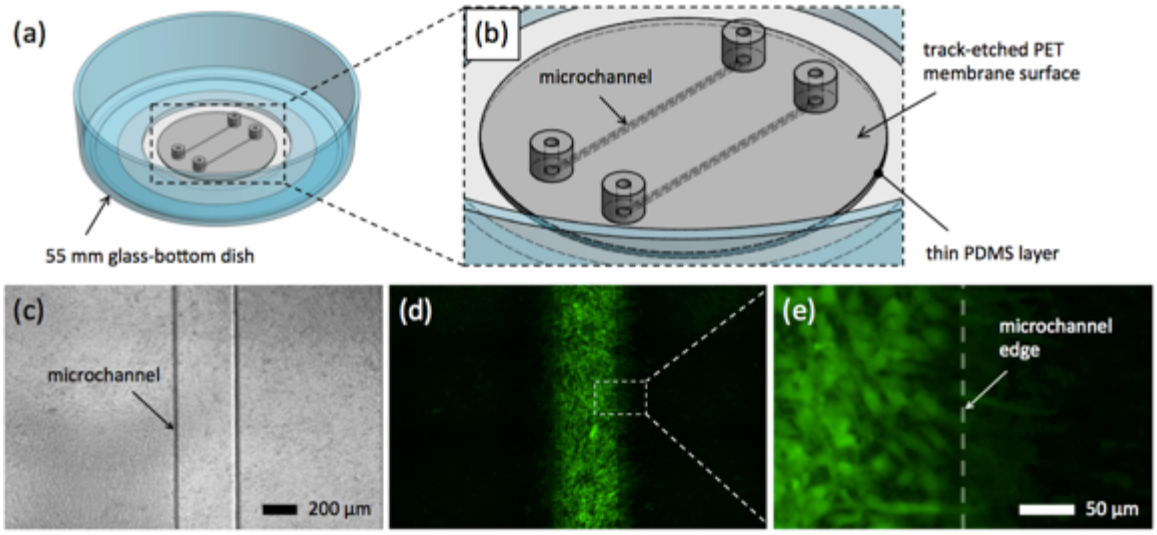

Figure 3.4: An open-surface basal-side stimulation device using track-etched membranes. (a) An isometric schematic of the open-surface basal-side stimulation device. The device is integrated into a cover-glass bottom 55 mm dish. (b) A track-etched PET membrane comprises the cell culture substrate and seals the underlying PDMS microchannels. (c) A phase contrast image of differentiated C2C12 myotubes grown on the surface of the device after 2 weeks in culture. (d) A fluorescent image showing the targeted basal-side delivery of calcein-AM to a region of the cell layer. (e) A close-up view shows individual myotubes and the diffusive broadening near the edge of the microchannel

3.3.4 Rapid delamination is predicted for devices with a porous surface in contact with medium

In our testing we have investigated bonding to open-surface devices in which one surface of the porous membrane is entirely exposed to the surrounding medium during immersion. Initially we were surprised to find that the existing methods using APTES[18,28] or amine-epoxy bonding[22] resulted in rapid delamination after immersion in DMEM for 1 day at 37 °C (see Table 1). In order to explain the difference between our results and those reported in the literature we must consider the effect of our open-surface geometry on the delamination rate.

A porous membrane has a much higher perimeter available for hydrolytic attack when only one side is sealed with PDMS. Each individual pore presents an interface at which the surrounding medium can begin hydrolysis of the interfacial silane layer. For example, a membrane sandwiched between two PDMS slabs of 4 mm in radius has a perimeter of 25.1 mm (Fig. 4a). For a membrane bonded on only one side in an open-surface configuration (Fig. 4b) the effective perimeter can be expressed by

$$P = \varepsilon A_0 \pi 2r + \pi 2R \tag{1}$$

where ε is the porosity, $A_0$is the area of the membrane, r is the radius of a single pore, and R is the radius of the slab. For a porosity of 2×10^{10} pores m^{-2} and a pore diameter of 0.4 μm the effective perimeter is approximately 1.28 m due to the large contribution of the exposed pores. This amounts to a nearly 50-fold difference in the perimeter available for hydrolytic degradation. Now, if we also account for the increase in the pore size as a result of delamination, Eq. (1) becomes

$$P = \varepsilon A_0 \pi 2(r + \Delta) + \pi(d - 2\Delta) \tag{2}$$

where Δ is the delamination radius for a given unit of time as shown in Fig. 4(c-d). Similarly, we can describe the area of delamination as a function of time for a sandwiched sample configuration using the expression

$$A(t) = A_0 - \pi[R - r(t)]^2 \tag{3}$$

where $r(t)$ is the delamination radius as a function of time. For the open-surface configuration we must account for the area of delamination contributed by each individual pore with the expression

$$A_{open}(t) = \varepsilon A_0 \pi[r + r(t)]^2 - \varepsilon A_0 \pi r^2 + A(t) \tag{4}$$

Therefore the area of delamination for each condition is expressed by a quadratic function of $r(t)$. Comparing the coefficients for $r(t)^2$ for the open-surface and sandwiched configuration we have

$$\varepsilon A_0 \pi \text{ vs. } \pi \tag{5}$$

The product of εA_0 is the total number of pores for the surface area of the bonded sample; therefore the rate of delamination depends heavily on the porosity of the membrane used in our sample. For a comparison between the delamination of open-surface and sandwiched samples see Fig. 4e. This analysis predicts a rate of delamination that is $\varepsilon A_0 = 1.0 \times 10^6$ times faster for an open-surface sample compared to a sandwiched sample. This rapid degradation at first appears to be a fundamental limitation of the method, however, individual bonds can re-associate under equilibrium. In theory, the strength of a silane interfacial layer is due to the number of bonds and the continual reorganization of the bonds to minimize the stress at the interface between the two substrates[19]. However, with the contamination of this interface by cations from the medium, the equilibrium process could be disrupted to favour hydrolysis of the layer. The cation induced hydrolysis can explain the difference in stability of sandwiched and open-surface samples bonded using APTES. Our solution is to employ a dipodal silane in which the individual silane molecule has 6 alkoxysilane functional groups available for bonding. Studies have shown that dipodal silanes are more effective anti-corrosion treatments for metals exposed to harsh salt solutions[29]. According to a leading manufacturer of silanes, Gelest, Inc., the use of a dipodal silane can theoretically improve bond strength by 100,000 times at equilibrium since the number of bonds increases from 3 to 6 per silane molecule[24]. By considering the theoretical bond strength of the dipodal silanes it is possible to reconcile the difference in the predicted rate of delamination and the improved bond strength we have observed with our silane modification method.

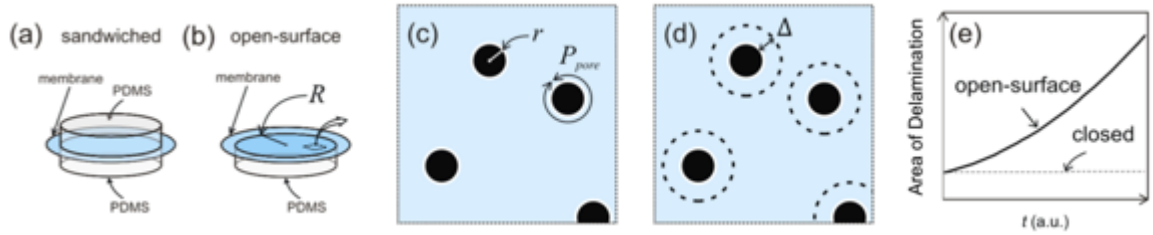

Figure 3.5: Rapid delamination is predicted membranes bonded with an open-surface. (a) Schematic of a sandwiched configuration in which both side of the membrane are bonded to PDMS slabs. The perimeter available to hydrolytic attack is determined by the radius of the sample. (b) Schematic of an open-surface configuration in which the membrane is bonded to only one side of a PDMS slab. Samples were tested with the open-surface configuration in order to determine an effective silane bonding strategy. (c) A schematic of the surface of the membrane depicts the pore radius and perimeter available to hydrolytic attack. Each individual pore contributes to the total perimeter available to attack. (d) The effective perimeter in contact with the medium grows as the radius increases during delamination. (e) Plotting the theoretical area of delamination for an arbitrary growth rate as described in eq. 5 predicts that the open-surface configuration would decay 1.0×10^6 times faster than a closed configuration under the same conditions.

3.4 CONCLUSIONS

We initially observed rapid delamination of open-surface devices fabricated using APTES bonding methods when immersed in DMEM. Our theoretical analysis of the rate of delamination offers an explanation to the mechanism of degradation. Following the assay of a variety of formulations, we determined that the 2% bis-amino silane in 1% water and IPA offered the most straightforward method for producing stably bonded open-surface devices. Using XPS analysis we confirmed changes in the elemental composition for silane-treated membranes and found that bis-amino silane results in greater and more stable introduction of silicon and nitrogen than APTES. We demonstrated the long-term bond stability of this silane treatment with operation of a simple device for the basal-side stimulation of differentiated C2C12

3.5 REFERENCES

1. Torisawa Y, Chueh B, Huh D, Ramamurthy P, Roth TM, Barald KF, Takayama S. Efficient formation of uniform-sized embryoid bodies using a compartmentalized microchannel device. *Lab. Chip*. 2007;7(6):770–776.

2. Kim T, Pinelis M, Maharbiz MM. Generating steep, shear-free gradients of small molecules for cell culture. *Biomed. Microdevices*. 2008;11(1):65–73.

3. Cate DM, Sip CG, Folch A. A microfluidic platform for generation of sharp gradients in open-access culture. *Biomicrofluidics*. 2010;4(4). Available at: http://www.ncbi.nlm.nih.gov/pmc/articles/PMC2994924/. Accessed November 14, 2012.

4. Abhyankar VV, Lokuta MA, Huttenlocher A, Beebe DJ. Characterization of a membrane-based gradient generator for use in cell-signaling studies. *Lab. Chip*. 2006;6(3):389.

5. Kawada J, Kimura H, Akutsu H, Sakai Y, Fujii T. Spatiotemporally controlled delivery of soluble factors for stem cell differentiation. *Lab. Chip*. 2012;12(21):4508–4515.

6. Kim C, Kreppenhofer K, Kashef J, Gradl D, Herrmann D, Schneider M, Ahrens R, Guber A, Wedlich D. Diffusion- and convection-based activation of Wnt/β-catenin signaling in a gradient generating microfluidic chip. *Lab. Chip*. 2012;12(24):5186–5194.

7. Epshteyn AA, Maher S, Taylor AJ, Holton AB, Borenstein JT, Cuiffi JD. Membrane-integrated microfluidic device for high-resolution live cell imaging. *Biomicrofluidics*. 2011;5(4):046501.

8. Achyuta AKH, Conway AJ, Crouse RB, Bannister EC, Lee RN, Katnik CP, Behensky AA, Cuevas J, Sundaram SS. A modular approach to create a neurovascular unit-on-a-chip. *Lab. Chip*. 2012;13(4):542–553.

9. Ismagilov RF, Ng JMK, Kenis PJA, Whitesides GM. Microfluidic Arrays of Fluid–Fluid Diffusional Contacts as Detection Elements and Combinatorial Tools. *Anal. Chem*. 2001;73(21):5207–5213.

10. Kuo T-C, Cannon, Chen Y, Tulock JJ, Shannon MA, Sweedler JV, Bohn PW. Gateable Nanofluidic Interconnects for Multilayered Microfluidic Separation Systems. *Anal. Chem*. 2003;75(8):1861–1867.

11. Zhang Y, Timperman AT. Integration of nanocapillary arrays into microfluidic devices for use as analyte concentrators. *Analyst*. 2003;128(6):537–542.

12. Flachsbart BR, Wong K, Iannacone JM, Abante EN, Vlach RL, Rauchfuss PA, Bohn PW, Sweedler JV, Shannon MA. Design and fabrication of a multilayered polymer microfluidic chip with nanofluidic interconnects via adhesive contact printing. *Lab. Chip*. 2006;6(5):667–674.

13. Masand SN, Mignone L, Zahn JD, Shreiber DI. Nanoporous membrane-sealed microfluidic devices for improved cell viability. *Biomed. Microdevices*. 2011;13(6):955–961.

14. Morel M, Galas J-C, Dahan M, Studer V. Concentration landscape generators for shear free dynamic chemical stimulation. *Lab. Chip*. 2012;12(7):1340.

15. Chueh B, Huh D, Kyrtsos CR, Houssin T, Futai N, Takayama S. Leakage-Free Bonding of Porous Membranes into Layered Microfluidic Array Systems. *Anal. Chem*. 2007;79(9):3504–3508.

16. VanDersarl JJ, Xu AM, Melosh NA. Rapid spatial and temporal controlled signal delivery over large cell culture areas. *Lab. Chip*. 2011;11(18):3057.

17. Kimura H, Yamamoto T, Sakai H, Sakai Y, Fujii T. An integrated microfluidic system for long-term perfusion culture and on-line monitoring of intestinal tissue models. *Lab. Chip*. 2008;8(5):741–746.

18. Aran K, Sasso LA, Kamdar N, Zahn JD. Irreversible, direct bonding of nanoporous polymer membranes to PDMS or glass microdevices. *Lab. Chip*. 2010;10(5):548.

19. Plueddemann EP. *Silane Coupling Agents*. Springer; 1982.

20. Vlachopoulou ME, Tserepi A, Pavli P, Argitis P, Sanopoulou M, Misiakos K. A low temperature surface modification assisted method for bonding plastic substrates. *J. Micromechanics Microengineering*. 2009;19:015007.

21. Zhang Z, Zhao P, Xiao G. The fabrication of polymer microfluidic devices using a solid-to-solid interfacial polyaddition. *Polymer*. 2009;50(23):5358–5361.

22. Tang L, Lee NY. A facile route for irreversible bonding of plastic-PDMS hybrid microdevices at room temperature. *Lab. Chip*. 2010;10(10):1274.

23. Lee KS, Ram RJ. Plastic–PDMS bonding for high pressure hydrolytically stable active microfluidics. *Lab. Chip*. 2009;9(11):1618.

24. Gelest, Inc. Difficult Substrates. *http://www.gelest.com/goods/pdf/faq/question%208.pdf*. 2006. Available at: http://www.gelest.com/goods/pdf/faq/question%208.pdf.

25. Hsu C-H, Chen C, Folch A. Microcanals for micropipette access to single cells in microfluidic environments. *Lab. Chip*. 2004;4(5):420.

26. Yaffe D, Saxel O. Serial passaging and differentiation of myogenic cells isolated from dystrophic mouse muscle. *Nature*. 1977;270(5639):725–727.

27. Howarter JA, Youngblood JP. Surface Modification of Polymers with 3-Aminopropyltriethoxysilane as a General Pretreatment for Controlled Wettability. *Macromolecules*. 2007;40(4):1128–1132.

28. Sunkara V, Park D-K, Hwang H, Chantiwas R, Soper SA, Cho Y-K. Simple room temperature bonding of thermoplastics and poly(dimethylsiloxane). *Lab. Chip*. 2011;11(5):962.

29. Zhu D, Ooij WJ va. Enhanced corrosion resistance of AA 2024-T3 and hot-dip galvanized steel using a mixture of bis-[triethoxysilylpropyl]tetrasulfide and bis-[trimethoxysilylpropyl]amine. *Electrochimica Acta*. 2004;49(7):1113–1125.

Chapter 4: Microfluidic Transwell Inserts

4.1 Introduction

The generation of well-characterized, stable, and quantifiable biochemical gradients is important for in vitro studies of gradient sensing biology. A variety of microfluidic devices offer these capabilities[1–3], but there remain practical limitations in implementation of these devices to conventional cell culture techniques impeding their adoption by the biological community. One of the important limitations is that most existing microfluidic platforms do not provide simple methods for interfacing with cell cultures. In typical designs, proteins and cells are injected into tiny microchannels requiring special technique for substrate preparation and cell culture. For sensitive cell types, such as primary neurons, long-term culture within microchannels can be challenging due to the shear stress created by microfluidic flow conditions. To address these issues we have developed a modular microfluidic gradient device, which we refer to as a 'microfluidic transwell insert', that interfaces with standardized 6-well plates, which are routinely employed in cell cultures. This device allows for the generation of long-term stable gradients over large areas while exerting extremely low fluid shear stress. These characteristics make the platform well suited for gradient application to a variety of sensitive cell cultures and enable application to tissue explants which are impractical to culture within microchannels.

In this chapter, we will describe the methods developed for fabrication of devices, design considerations, finite-element modeling (FEM), and characterization of devices using fluorescence microscopy. We will also demonstrate application of the microfluidic transwell insert to study chemotaxis of neutrophil cells and outgrowth of embryonic retinal explants.

4.1.1 Microfluidic transwell inserts

The goal of this work was to develop a user-friendly microfluidic concentration gradient generator that can be used with conventional cell culture technique. Our approach is based on controlling fluid communication between the device and cell culture through track-etched membranes. The track-etched membrane serves to compartmentalize flow, minimize shear stress, and enable modular application of the device to standard 6-well plates. The microfluidic transwell insert is designed for generating large-area gradients and straightforward application to cells cultured independently of the device using conventional technique.

The microfluidic transwell insert has several key design aspects: (1) The insert device is applied by simply placing it into the well of a 6-well plate where it is self-supported at a short distance (approximately 250 μm) above the cell culture surface. The device is untethered from the substrate; therefore, timing and orientation of the gradient is controlled by its manual placement inside the well. (2) Solutions of biomolecular factors are delivered to selected areas of a track-etched membrane via microchannels. Fluid communication between the device and the cell culture well is controlled through the high resistance membrane to generate gradients across and above the cell culture surface. (3) Flow within the device maintains an unlimited source and sink for soluble factors and long-term, stable gradient generation. (4) Cells or tissue explants can be cultured on standard glass-bottom 6-well plates. (5) The device materials, poly(dimethylsiloxane) (PDMS) and polyethylene terephthalate (PET), are transparent which permits real-time observations of cell morphology and migration during the course of the gradient application. (6) The track-etched PET membrane shields cells from exposure to shear stress because of its high fluidic resistance.

A 3D rendering in **Figure 4.1** depicts the application of the microfluidic transwell insert to a standard glass-bottom 6-well plate. Additional 3D views of the device are shown in **Figure 4.2.** Top views and cross-sectional schematics in **Figure 4.3** show the device inserted in a standard glass-bottom 6-well and a simulated concentration gradient. A critical feature is that when the device is inserted it maintains open sidewalls; compressive and shear forces are averted through passive application to pre-existing cell cultures. The untethered design and the modular interface simplify integration with cell cultures and conventional protocols. The photographs in **Figure 4.4** show the device filled with dye solutions to visualize the microchannel architecture and gradient.

4.1.2 Track-etched membranes

A key component of our device is an integrated track-etched membrane that restricts flow from the device to the cell culture. This type of porous membrane is manufactured in thin sheets of material by a process known as track-etching. First, particle tracks are defined in a film using irradiation or bombardment with nuclear particles and then pores are chemically etched into the material along the damaged zone[4]. The pore shape, size, and porosity of membranes can be controlled through the irradiation conditions, material properties, and chemical etching process. Track-etched membranes are commercially available in polycarbonate and polyethylene terephthalate (PET). The unique properties of the track-etching method enable the production of thin membranes, typically 5-20 μm thick, with well-defined porosity from 1×10^5 to 6×10^8 pores cm^{-2} and cylindrical pores in the range of 15 nm to 12 μm in diameter. For cell culture applications, track-etched membranes are commonly available in pore sizes of 0.4, 1, 3, 8, and 10 μm diameters in optically transparent PET for live cell imaging. In this work, we will utilize transparent PET membranes of 1.0 μm pore diameter as an integral component of our microfluidic transwell device.

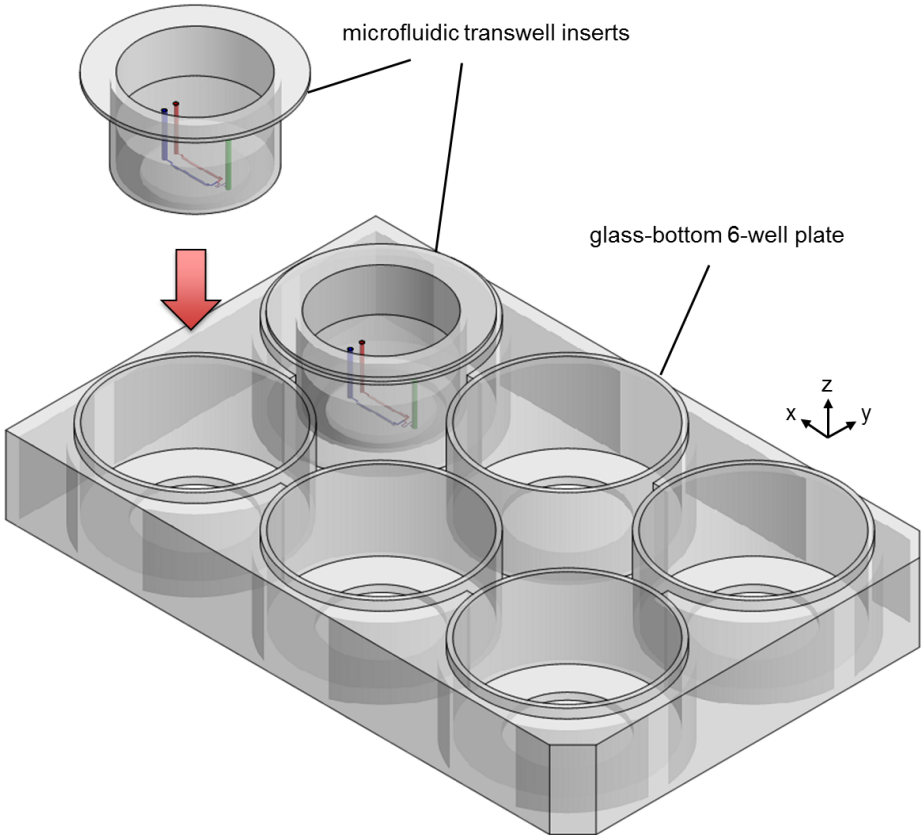

Figure 4.1: 3D rendering of the microfluidic transwell insert and 6-well plate assembly. The modular device can be placed into a standard cover-glass bottom 6-well plate to interface with pre-existing cell or tissue cultures.

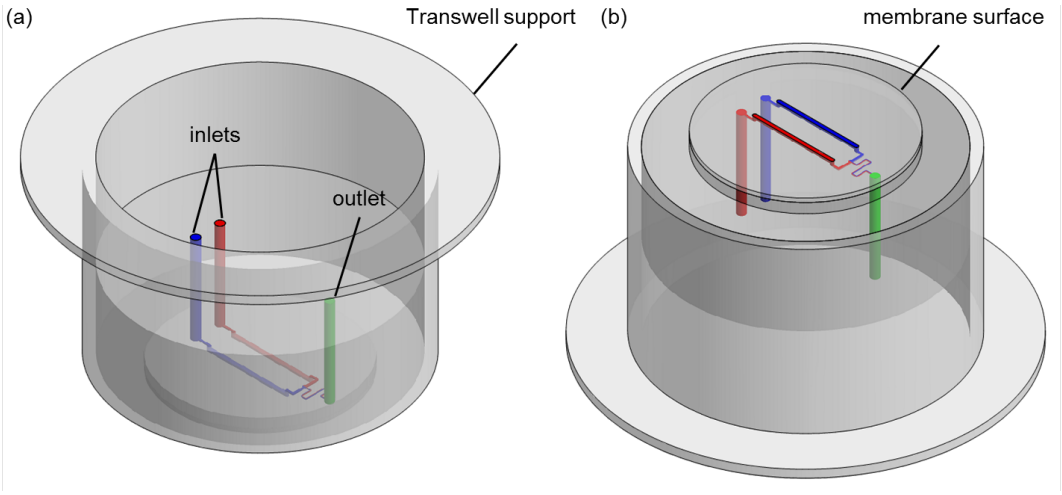

Figure 4.2: 3D rendering of the microfluidic transwell insert and cross-sectional views. (a) Top and (b) bottom isometric views. Inlet and outlet ports are accessible from the top of the device. The embedded microfluidic channels (shown in red, blue, and green) deliver flows to 2 portions of the membrane surface.

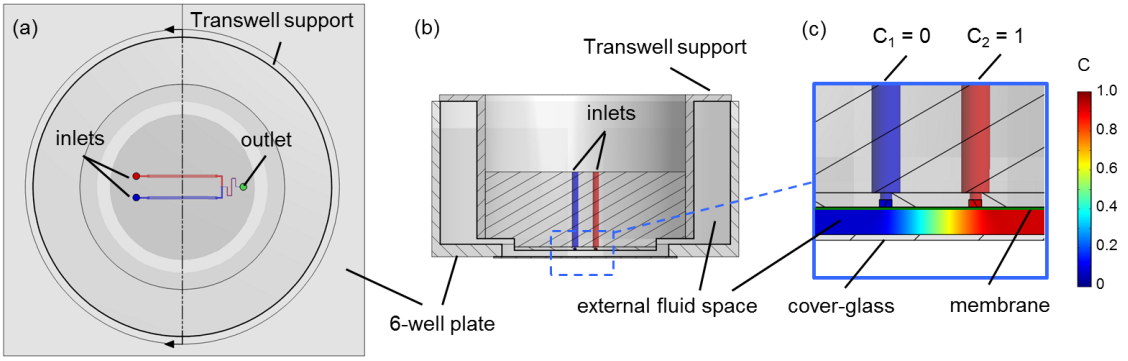

Figure 4.3: Top and cross-sectional views of the microfluidic transwell insert. (a) A top view of the device as it rests self-supported in a 6-well. The well can be seeded with cells or tissue explants before inserting the device. A cross-sectional view taken along the dotted line is shown in (b). The 'external fluid space' is defined by the fluid between the device surfaces and the well plate. An enlarged view of the gradient generating region is shown in (c). Soluble factors delivered by the inlets flow along the membrane through the microchannels. A portion of the flow passes through the membrane (green line) and into the 'external fluid space'. The gradient is generated in this fluid space between the membrane and the cover-glass cell culture surface. The device hangs self-supported, so that the membrane surface is 250 µm above the cell culture surface. Adjacent channels loaded at relative concentrations of $C_1 = 0$ and $C_2 = 1$ establish a concentration gradient above the cell culture surface (shown as a color map).

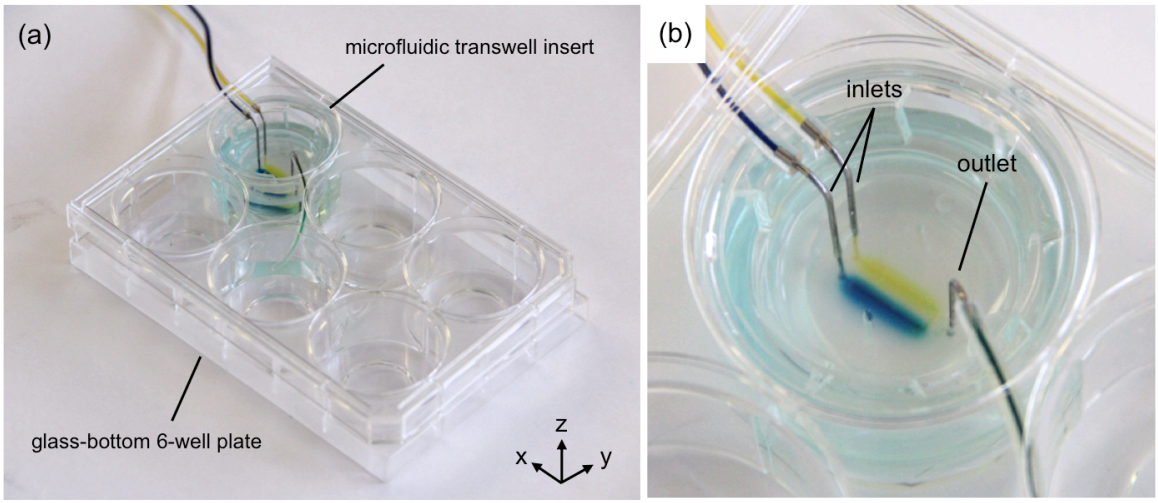

Figure 4.4: Photographs of a microfluidic transwell insert loaded with colored dyes. Yellow and blue dyes are used here to visualize the microfluidic network and gradient delivery. (a) The device is self-contained within a 6-well plate. Inlet tubing runs in through a slit in the lid of the well plate. (b) A close-up view shows the routing of inlets and outlets to the device. The outlet drains into the inter-well space of the well plate.

4.2 Fabrication of Microfluidic Transwell Devices

4.2.1 Multilayer soft-lithography

Fabrication of transwell microfluidic inserts was accomplished using multilayer soft-lithography of PDMS replicas[6], oxygen plasma for PDMS-PDMS bonding, and silane coupling for PDMS bonding to membranes. The device was assembled from 4 parts including an injection-molded plastic support, embedded PDMS replica, a thin PDMS layer, and a track-etched membrane (**Figure 4.5**). For fabrication of master molds, silicon wafers were spin-coated with SU-8 2000 series photoresists (Microchem Co., Newton, MA) and photopatterned using multilayer photolithography. For the master mold to the embedded layer shown in **Figure 4.5(b)**, a 75 μm thick layer was spin-coated using SU-8 2075 at 3000 rpm to define the inlet and outlet channels. After post-exposure baking of the first layer, a second layer of 100 μm was spin-coated using SU-8 2075 at 2125 rpm to pattern the low-resistance channel that feeds flow to the membrane and to a

common outlet. The master of the thin PDMS replica layer (**Figure 4.5(c)**) was designed to produce a perforated PDMS layer through exclusion-molding technique[7]. The features for the molding of the gradient delivery channels were patterned with a 200 μm thick layer of SU-8 (produced by spin-coating SU-8 2075 at 2125 rpm and pre-baking twice). Next, an additional 200 μm thick layer was spin-coated to pattern the vias and boundary features (see **Figure 4.7(b)**). After photopatterning, post-exposure baking, and development of the SU-8, masters were hard baked at 150 °C on a hotplate. Masters were then treated using several drops of a fluorinated-trichlorosilane (#448931, Sigma, St. Louis, MO) in a desiccator under house vacuum.

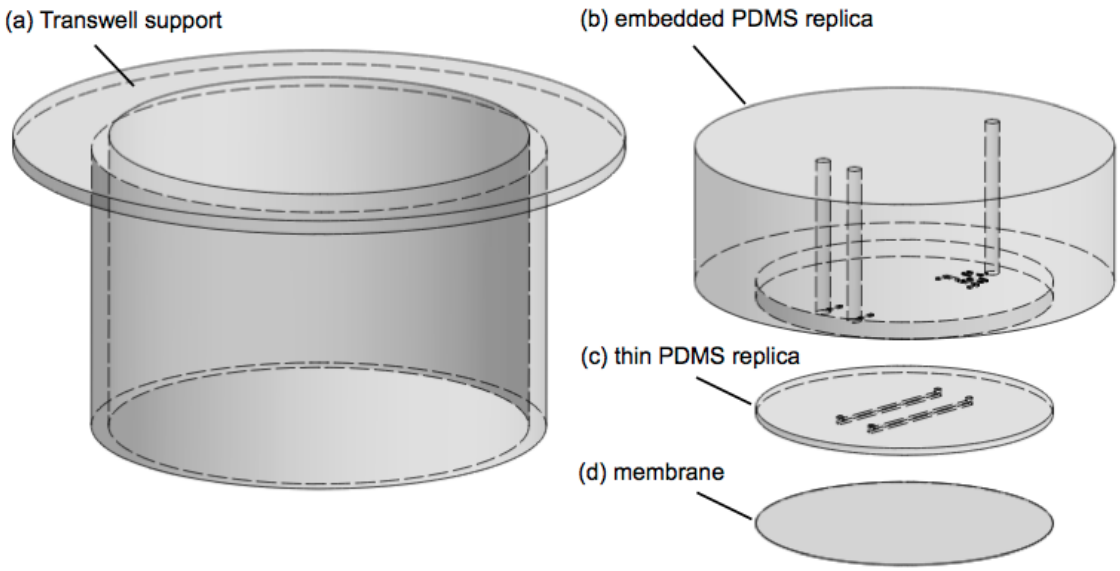

Figure 4.5: Multilayer soft-lithography and plasma bonding assembly of devices. (a) A transwell insert plastic support. (b) A microchannel featured PDMS replica is embedded in the plastic transwell support. (c) A thin PDMS layer is produced using exclusion molding technique. (d) A track-etched membrane is modified using a bis-amino silane method to render it reactive with oxygen plasma treated PDMS for hydrolytically stable bonding of the complete device.

4.2.2 Embedding of PDMS into plastic supports

The top microchannel layer of the microfluidic transwell insert was replica molded to embed the PDMS into a plastic support (**Figure 4.6(a)**). The plastic supports from Transwell-brand inserts were harvested by removing the track-etched membrane. The supports were oxygen plasma treated, then the inside surface is coated with a 1% APTES, 1% vinyl silane, 5% water, 93% methanol solution using a cotton swab and allowed to air dry in a chemical fume hood. We found that without the vinyl/APTES silane treatment, PDMS of the embedded layer cured within the plastic support could be easily detached under mild force such as punching holes for inlets. Spacers of 34 mm outer diameter and 18 mm inner diameter were made by laser cutting a stack consisting of a .06" thick acrylic sheet and an adhesive backed 10 mil thick acrylic film. Spacers were fixed onto the SU-8 photopatterned master to provide a pedestal for the plastic support during molding. As a result of the spacer, the featured surface of the embedded PDMS extends past the plastic support and nests into the 20 mm diameter miniature well of the cover-glass bottom 6-well (**Figure 4.6(b)**). The silane-modified supports were lightly dipped in uncured PDMS, placed on the spacers, and baked at 80 °C on a hotplate to secure in place on the master mold. After curing and cooling to room temperature, uncured PDMS (7:1) was poured onto the master to fill the support. Room temperature curing is critical to prevent deformation of the flatness of the molded surface from heat shrinkage. The layer is left to cure for 48 hours at room temperature on a level surface. After curing, the device is carefully removed from the mold by prying it free with a straight edge razor blade and lubrication with 70% ethanol and water solution. Inlets and outlets are cored into the embedded PDMS using a 0.75 mm diameter biopsy punch (Z708798, Sigma-Aldrich, St. Louis, MO). 70% ethanol and water is injected into the inlets and outlets to rinse away any remaining PDMS debris.

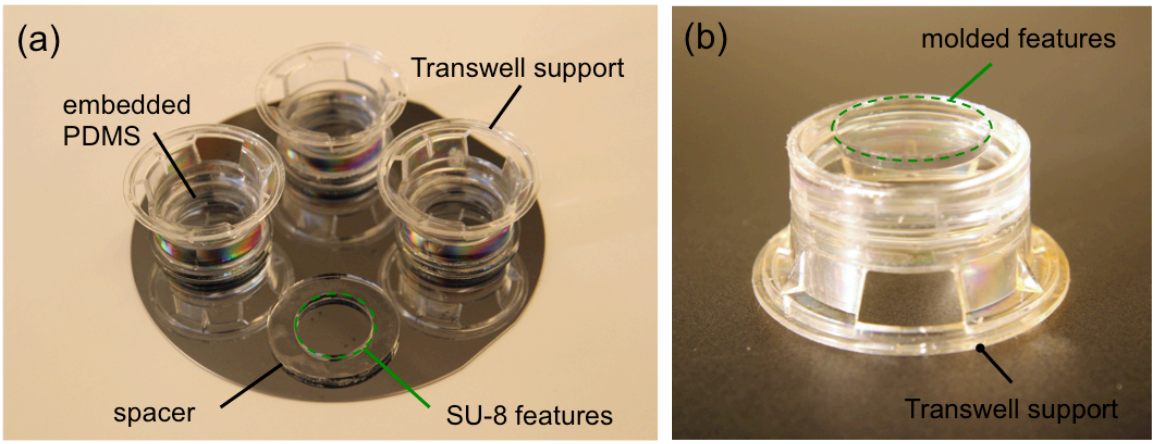

Figure 4.6: Embedding of microchannel layer in plastic supports. (a) Plastic transwell supports modified with a coating of vinyl/APTES silane are placed on spacers to embed a thick micromolded PDMS layer. (b) After curing for 48 hours at room temperature, the layer is removed from the wafer. The 'molded features' extend an additional 1.8 mm beyond the edge of the Transwell support in order to define a 250 µm separation distance between the final device and the cover-glass of the 6-well plate.

4.2.3 Exclusion molding of thin PDMS layers

The thin PDMS layer was produced with 400 μm tall vias and 200 μm tall microchannel features using exclusion-molding technique (**Figure 4.7**). The master mold was placed on 4 sheets of polyester film on a 4" diameter, ½" thick steel disc. Uncured PDMS (7:1) was mixed, degassed, then poured onto the master, and degassed again to remove any residual air bubbles from the features. A sheet of polyester film was placed onto the uncured PDMS taking care to prevent trapping of air. Using a straight edge razor blade, the surface of the film was smoothened against the SU-8 features of the master. Next, 4 additional sheets of polyester film and a 4" diameter, 1/8" thick acrylic disc were stacked on top of the mold to add compliance to the stack. Finally, another steel disc was placed on top and the assembly was compressed using a no-twist C-clamp (#5046A18, McMaster-Carr, Santa Fe Springs, CA). The mold was allowed to cure overnight at room temperature before baking for 1 hour in a convection oven at 70 °C.

Room temperature curing was used because PDMS cured at elevated temperatures shrinks after cooling causing problems with registration of layers. Upon disassembly of the molding apparatus, the PDMS layers were cut out from the master using a sharp blade and placed onto a clean sheet of polyester film in preparation for plasma bonding. Care must be taken to ensure air bubbles and dust do not deform the flatness of the PDMS layer when applied to the film, so this step was done in a clean room.

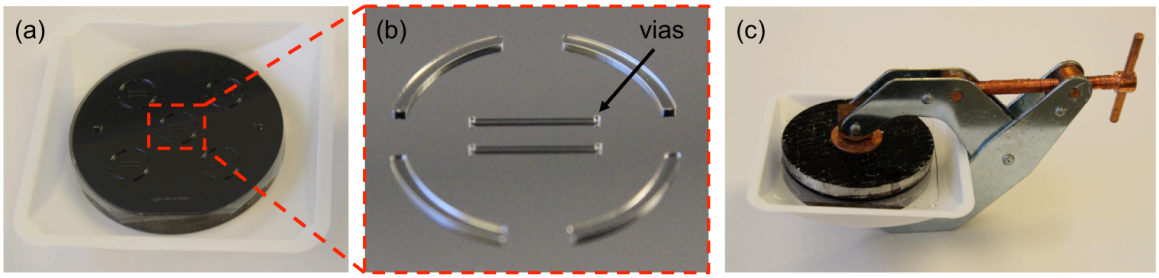

Figure 4.7: Exclusion molding of thin PDMS layers. (a) Photograph of the SU-8 photopatterned silicon wafer. (b) Enlarged view of a single mold. The circular boundary perforates the layer to assist de-molding. (c) The complete exclusion molding assembly. The large weigh boat catches the uncured PDMS that is displaced during clamping.

4.2.4 Plasma bonding assembly and silane coupling of membranes

Transparent PET track-etched membranes with 1.0 μm pore size and 1.6×10^{10} pores m^{-2} (BD Bioscience, #353102) were activated with oxygen plasma using 60 W, 670 mtorr, 60 sec, and 40 kHz RF from a Zepto plasma system (Diener Electronic GmBH, Ebhausen, Germany). Oxygen plasma treated membranes were treated in a solution of 2% bis-amino silane, 1% water, and 97% IPA solution at 80 °C on a hotplate as described in **Chapter 3**. After treatment, the silane modified membranes were cured for 30 min in a convection oven at 70 °C, then soaked in 70% ethanol in water solution for 30 min while the PDMS layers of the device were assembled. The PDMS layers were assembled using oxygen plasma to bond the exclusion and embedded layers (**Figure**

4.5(b-c)). After curing for 5 min at 80 °C, the devices were allowed to cool then activated with oxygen plasma once again and bonded to the silane modified membranes while wetted with a small amount of 70% ethanol in water solution to facilitate positioning and optimal contact with the PDMS. The surface of the membranes were dried using a compressed N_2 air gun, and then the devices were placed in a convection oven to cure at 70 °C. After curing, the excess membrane around the perimeter of the PDMS was removed using dissection tweezers to complete the devices.

4.3 Design of Membrane Micro-Flows

4.3.1 Hydraulic-electric circuit analogy

The design of microfluidic transwell insert was conceptualized using the hydraulic-electrical circuit analogy based on the similarities of the Hagen-Poiseuille's law for the flow of fluid and Ohm's law for the flow of current. For generating wide concentration gradients with the microfluidic transwell insert we desired a microfluidic circuit in which the flow delivered through the track-etched membrane was uniform along the length of the delivery microchannels. In the ideal scenario, shown in **Figure 4.8(a)**, each pore of the track-etched membrane can be considered to have equal flow, so that multiplying by the number of pores gives the total membrane flow:

$$I_m = I_p \rho A \qquad (1)$$

where *Ip* is the flow through an individual pore, *Im* is the total membrane flow, ϱ is the porosity of the membrane, and *A* is the area of the membrane. For uniform membrane flow the delivery channel must be designed to have significantly less hydraulic resistance than the membrane such that the pressure applied to each pore is equivalent. We can evaluate this situation by calculating the hydraulic resistances of our device. The

hydraulic resistance of the track-etched membrane can be calculated from the equivalent resistance of the individual pores in parallel:

$$\frac{1}{R_{mem}} = \frac{1}{R_1} + \frac{1}{R_2} + \cdots + \frac{1}{R_n} \tag{2}$$

Knowing that individual pores of the track-etched membrane are largely homogenous in diameter and length due to the track-etching process, we assume

$$R_{pore} = R_1 = R_2 = R_n \tag{3}$$

Simplifying Eq. (2) and (3) we can define the resistance of the membrane:

$$\frac{1}{R_{mem}} = \frac{n}{R_{pore}}$$

$$R_{mem} = \frac{R_{pore}}{A\rho_{pore}}. \tag{4}$$

The resistance of an individual pore is calculated from the resistance of a circular pipe:

$$R_{pore} = \frac{8\mu L}{\pi R^4} \tag{5}$$

where the μ is the viscosity, L the thickness of the membrane, and R the radius of the pore. Given the 1.0 μm pore diameter and 12 μm thickness of a BD falcon brand track-etched membrane used for the devices, we calculate the resistance of a single pore as:

$$R_{pore} = \frac{8\mu L}{\pi R^4} = \frac{8 \cdot 1{\times}10^{-3} \cdot 12{\times}10^{-6}}{\pi\,(500{\times}10^{-9})^4} = 4.89{\times}10^{17}\ \frac{kg}{m^4 s} \tag{7}$$

For the microfluidic transwell insert, the area of the membrane that receives flow from one inlet is 8 mm long and 350 μm wide with circular ends. The nominal membrane area is 2.896×10^{-6} m^2. Solving Eqs. (4) and (5) using the area of the membrane and the porosity, $1.6{\times}10^{10}$ pores m^{-2}, we calculate the resistance of the membrane for one inlet as:

$$R_{mem} = \frac{R_{pore}}{A\rho_{pore}} = \frac{4.89\times10^{17}}{2.896\times10^{-6}\cdot 1.6\times10^{10}} = 1.06\times10^{13}\,\frac{kg}{m^4 s} \quad (8)$$

For the delivery microchannel we use the equation for the hydraulic resistance of a rectangular microchannel[8]:

$$R_d = \frac{12\mu L}{wh^3\left(1-\frac{h}{w}\left(\frac{192}{\pi^5}\right)\sum_{n=1,3,5}^{\infty}\frac{1}{n^5}\tan h\left(\frac{n\pi w}{2h}\right)\right)} \quad (9)$$

Calculating Eq. (9) for w = 350 μm, h = 200 μm, and L = 8 mm, we determine that

$$R_d = 3.44\times10^{10}\,\frac{kg}{m^4 s} \quad (10)$$

Comparing the results of Eqs. (8) and (10) shows that resistance of the membrane is 3 orders of magnitude greater than the resistance of the membrane. By this design, the pressure along the length of the delivery channel, P_{mem}, is insensitive to the flow lost through the membrane and uniform. Therefore, we can simplify our hydraulic circuit model by ignoring the pressure drop in the low resistance delivery channel. The diagram in **Figure 4.8(b)** shows how the hydraulic circuit is simplified by this situation. The actual microfluidic transwell insert shown in **Figure 4.2** has 2 inlet and delivery channels, so we can model the flow by combining 2 circuits in parallel as shown in **Figure 4.9**. Following a similar logic for the negligible resistance of the delivery channel compared to the membrane, we have designed a connection between the 2 inlets that is low resistance. This ensures that the membrane area supplied by each inlet is at the same pressure and simplifies the fluid routing with a common outlet.

While having the resistance of the delivery channels much higher than the membrane is desirable for uniform flow delivery, we also require non-trivial resistance at

the outlet to drive enough flow through the membrane. The pressure at the membrane can be defined using the conservation of energy according to Kirchhoff's laws:

$$P_{mem} = I_{in} \frac{R_{out}(0.5)R_{mem}}{R_{out} + (0.5)R_{mem}} \tag{11}$$

For our design, we have an outlet microchannel with dimensions w = 100 μm, h = 75 μm, and L = 6 mm. Solving Eq. (9) we calculate the outlet resistance to be:

$$R_{out} = 1.71 \times 10^{12} \frac{kg}{m^4 s} \tag{12}$$

Using the analogy to Ohm's law, we can rearrange Eq. (11) to solve:

$$I_{mem} = \frac{P_{mem}}{(0.5)R_{mem}} = I_{in} \frac{R_{out}}{R_{out} + (0.5)R_{mem}}$$

$$= I_{in} \frac{1.71 \times 10^{12}}{1.71 \times 10^{12} + 0.53 \times 10^{13}} \tag{13}$$

$$I_{mem} \approx I_{in} \cdot 0.24$$

The hydraulic circuit model described here predicts that 24% of the flow applied by the syringe pump will escape through the membrane.

We can extend the analysis further to describe the membrane with Darcy's law:

$$I_{mem} = \frac{kAP_{mem}}{\mu L} \tag{14}$$

where for one delivery channel, I_{mem} is the flow, μ is viscosity, A is area of membrane, L is thickness of the membrane, P_{mem} is the pressure drop, and k is the permeability parameter of the membrane. Rearranging Eq. (14) using Ohm's law we define k as:

$$\frac{I_{mem}}{P_{mem}} = R_{mem} = \frac{\mu L}{kA}$$

$$k = \frac{\mu L}{R_{mem} A} \tag{15}$$

Simplifying Eq. (15) further using Eqs. (7) and (8), the permeability parameter can be described as a function of the porosity and pore radius as follows:

$$k = \frac{\pi \rho R^4}{8} \tag{16}$$

Solving with the 1.0 μm pore diameter and porosity of 1.6×10^{10} pores m^{-2}, we can calculate the permeability parameter, $k = 3.927\times10^{-16}$ m^2. This parameter is important for modeling the bulk properties of the track-etched membranes since it describes hydraulic conductivity independent of the area and thickness of the membranes used. In the following section, we will utilize this parameter in FEM simulations to predict the full 3D flow and molecular transport of the microfluidic transwell devices.

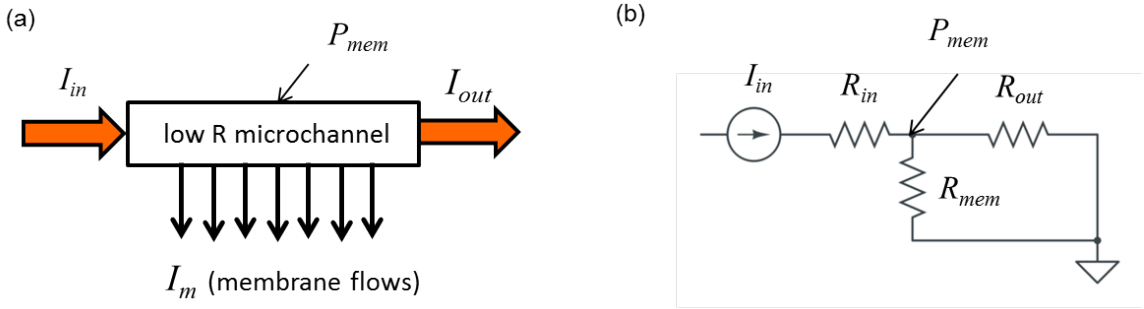

Figure 4.8: Hydraulic circuit for microfluidic transwell flows depicting the flow network for one inlet. Syringe pump driven flow is indicated by I_{in}. Flow entering the circuit at the inlet can either pass through the membrane or through the outlet of the device. (a) The membrane can be modeled as a series of parallel conduits that connect to ground in parallel with the resistance of the outlet microchannels. (b) The low resistance microchannel supplying flow across the membrane is 3 orders of magnitude lower in resistance compared to the membrane; therefore it is negligible and each pore can be treated as the same pressure. This simplifies the model to a single high resistance path in parallel with the outlet resistor.

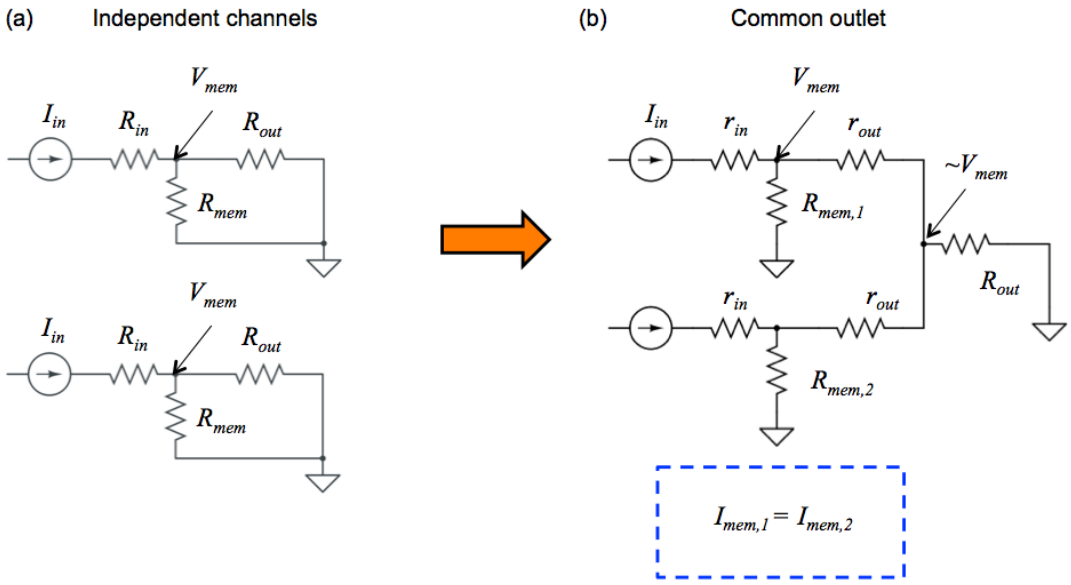

Figure 4.9: Hydraulic circuit for a microfluidic transwell device with 2 inlets and a common outlet. (a) Independent hydraulic networks. (b) Each network can be connected via a low resistance bridge to establish the same pressure at each portion of the membrane and ensure that equal flow is delivered.

4.4 FINITE-ELEMENT MODELING OF DEVICES

The finite-element modeling software, COMSOL Multiphysics, was used to predict and analyze 3D models of the microfluidic transwell insert. Using this approach time dependent and steady state models were solved to describe the fluid velocity and molecular transport controlling the generation of microfluidic transwell gradients. Importantly, models were used to study the effects of device geometry, flow rates, and diffusivity on the ultimate gradient shape and time dependence. Simulations were computed on a MacBook Pro with a 2.3 GHz Intel Core i5 processor, 16 GB RAM, and a solid-state drive.

4.4.1 3D finite-element model and method

The *Free and Porous Media Flow* physics module was used to simultaneously solve for the free flow in both the microchannels and 6-well, and porous flow in the track-etched membrane for the microfluidic transwell devices. The *Free and Porous Media Flow* module approximates the physics at the interface between the free flow and porous regimes using the Navier-Stokes and Brinkman equations in a single domain model as described by Bars and Worster[9]. The velocity field and pressure gradient are treated as continuous across the transition from free flow to porous flow. It is possible to couple the free flow interface to a separate Darcy's law interface using a multi-domain Stokes-Darcy model[9], but the relatively small dimension of the track-etched membrane (12 μm) compared to the surrounding fluid channels demands attention to the transitional flows that are approximated by the Brinkman equations. The simulated region includes the device microchannel network and the 20 mm diameter-external fluid space of the 6-well plate surrounding as depicted in **Figure 4.10**.

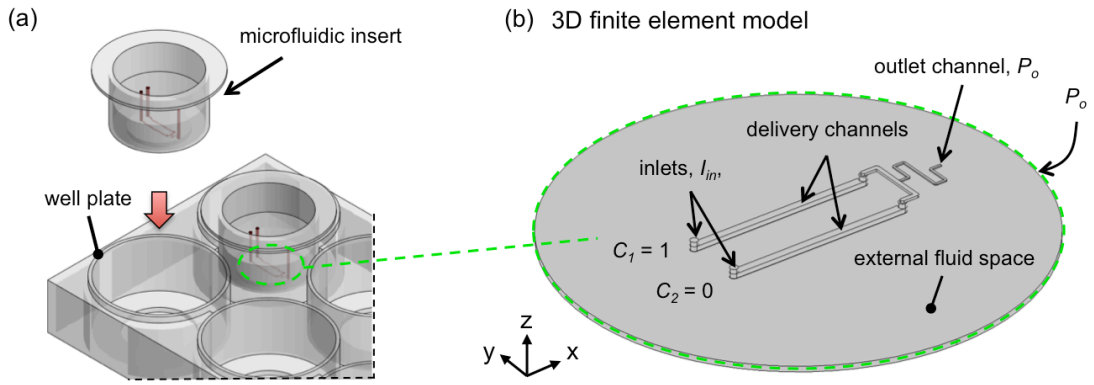

Figure 4.10: Contextual diagram of the simulated region and FEM geometry. (a) The model represents the fluid flow of the device microchannel network and the external fluid space between the membrane and the cell culture surface of the 6-well plate. (b) The boundary conditions for the simulation assume defined inlet flows I_m with normalized concentrations of $C_1 = 1$ and $C_2 = 0$. The edge of the fluid space and the outlets microchannels are set to $P_o = 0$ and open for convective flux of the transported species. Walls are defined with a no slip condition. Separating the gradient channels and the fluid space is a 12 µm thin domain of the same area that defines the track-etched membrane flows using the permeability parameter, $k = 3.927\times10^{-16}$ m^2.

Global parameters used in the model were density $\rho = 1\times10^{3} kg\ m^{-3}$, dynamic viscosity $\mu = 1\times10^{-3} Pa\cdot s$, and membrane permeability $k = 3.927\times10^{-16}\ m^2$. In general, to solve 3D flow problems it is important to minimize the complexity of the model or else utilize powerful computing resources in terms of memory or computation time. Ideally, the model can be solved using one of the direct solvers in COMSOL to be computationally efficient; however, the mesh must be optimized. For the geometry of the microfluidic transwell, there are features at small dimensions (e.g. the track-etched membrane thickness) and large dimensions (e.g. the external fluid space) that add to the difficulty in discretizing the model. In addition, the sharp corners present at the intersections of the membrane with the external fluid space are difficult to resolve with course meshes. FEM problems with multi-scale geometries will suffer from a large number of mesh elements when using automatic meshing in COMSOL. A solution is to

define *mesh control entities* in the geometry for improving transitions from fine to course mesh sizes and reducing the overall model complexity and ultimate solving time (**Figure 4.11**). With this mesh we solved the velocity field using the *PARDISO* direct solver with 211,210 mesh elements and 932,967 degrees of freedom in approximately 58 min. To test for possible mesh dependence and compare solution times, we solved using the iterative solver, *GMRES* with *Geometric Multigrid*, for 411,016 mesh elements and 3,208,929 degrees of freedom in approximately 4 hours. Results produced by the iterative and direct solvers did not differ in their overall flow profiles.

The results in (**Figure 4.12(a-b)**) describe the velocity field at a distance of 5 μm from the cell culture surface. Importantly, the flow velocities near the cell culture surface are low (~0-7 μm min^{-1}) in comparison to the delivery microchannel (~0-8.5×10^{2} μm min^{-1}). Characteristically, the flow decelerates as it moves further from the delivery channels into the larger space of the well. The center of the device forms a stagnation point due to the opposing flows (depicted as streamlines). Since the gradient delivery microchannel is of significantly lower resistance than the outlet and the membrane, the pressure is uniform within the membrane domain (**Figure 4.12(c)**).

The flow shown in **Figure 4.13(a-b)** originates from the membrane via the delivery channels. A pseudo-stagnation point is also formed along the cell culture surface beneath the edge of the delivery microchannels. Adjacent to this region, the majority of flow directly originating from the membrane impinges on the surface and curls away from the center of the device. The regions of relatively high convection are an unlimited source or sink due to convective transport of soluble factors from the delivery channels and the membrane. In contrast, the region between the 2 delivery channels receives significantly less flow.

The *Transport of Diluted Species* physics module for Fick's law was used to model the concentration profile resulting from the convection and diffusion. The velocity field obtained with either of the previously described methods was coupled to the convection physics. The concentration gradient generated at distance of 5 μm above the surface is shown in **Figure 4.13(a-b)**. A cross-sectional plot of the concentration in the y-z plane is shown in **Figure 4.13(c)**. The plot demonstrates that the concentration is uniform in the z-direction between the membrane and cell culture surface, an important characteristic for imaging gradients through the bulk fluid.

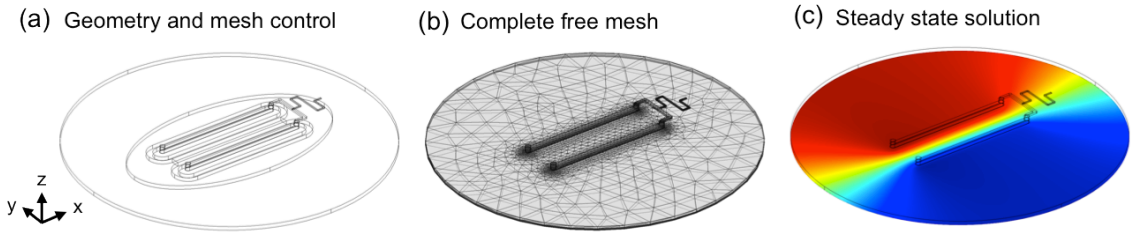

Figure 4.11: Representative FEM geometry, meshing, and steady state solution for microfluidic transwell inserts. (a) The geometry is shown with additional mesh control entities to guide changes in mesh element size. The mesh controls reduce the total number of elements required to achieve suitable mesh quality. (b) Elements size grows from small to large as required by the gradients in the velocity field. Larger gradients in the velocity field and smaller elements are required near the no slip conditions of the walls and especially within the microchannels and membrane domains. (c) An example of the steady state concentration profile achieved by solving the flow and transport physics for a flow rate of 50 µL hr^{-1} and 6.4×10^{-10} m^2 s^{-1}.

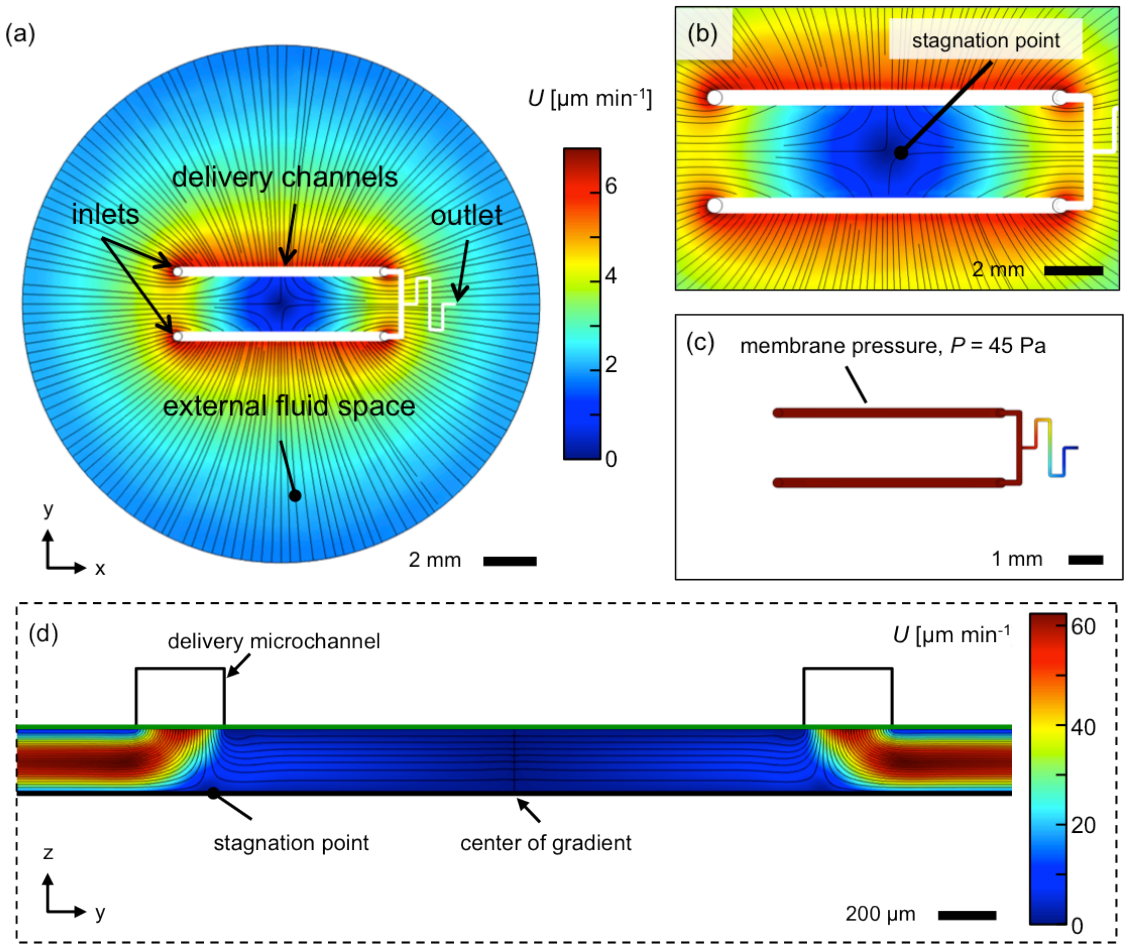

Figure 4.12: Steady-state simulation of flow in the microfluidic transwell device. The model results are for an inlet flow rate I_{in} = 50 μL hr^{-1} using the Navier-Stokes and Brinkman equations. (b) A color map of the velocity field U [μm min^{-1}] is shown at a distance of 5 μm above the cell culture surface. Black streamlines indicate the direction of flow as it emerges from the membrane via the delivery channels (white). (b) An enlarged view of the gradient generating region of the device. The center of the device forms a stagnation point. (c) A top view of the model predicts uniform pressure, P = 45 Pa, within the delivery channel (shown here as red) and a pressure drop to P = 0 along the outlet microchannel (shown as a color map). (d) A cross-sectional view of the velocity profile across the center of the device (at x = 0) in the y-z plane. Black streamlines designate the instantaneous direction of flow that emerges from the membrane. At the center of the gradient opposing flows generate a stagnation point.

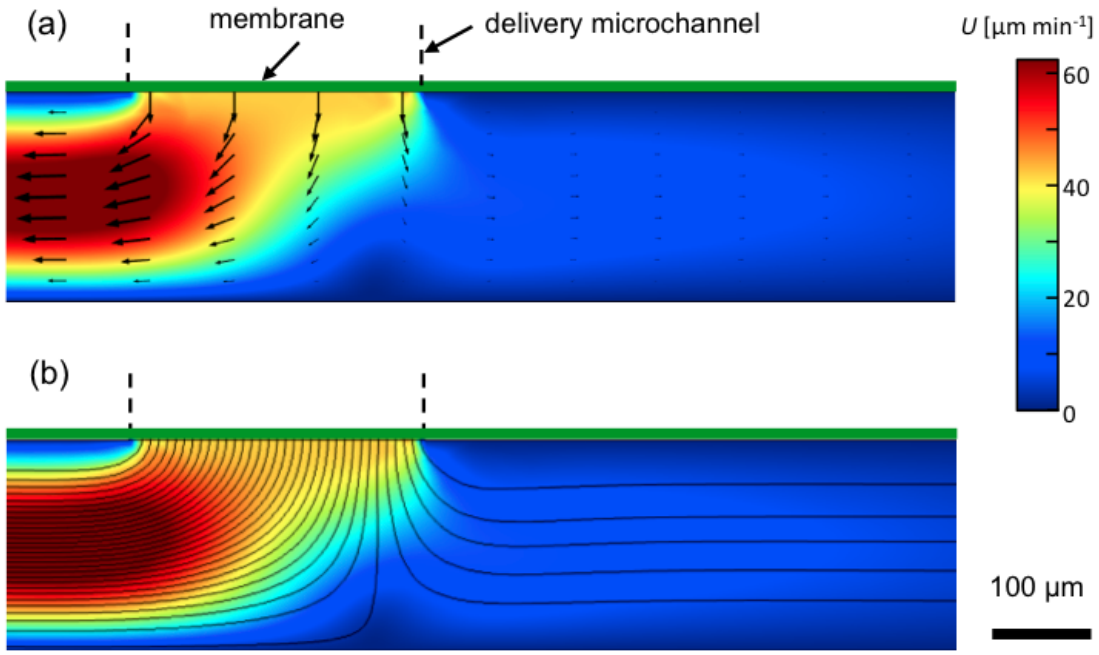

Figure 4.13: Enlarged cross-sectional profile for the steady-state flow velocity generated in the external fluid space. The model results are for an inlet flow rate I_{in} = 50 μL hr^{-1} using the Navier-Stokes and Brinkman equations. (a) A color map of the velocity field is shown with arrows designating the direction and magnitude of the flow velocity. (b) Uniformly distributed streamlines emerge from the membrane (green line). At a given point along the streamline, the tangent to the curve is the instantaneous flow direction while the density indicates the magnitude of the flow.

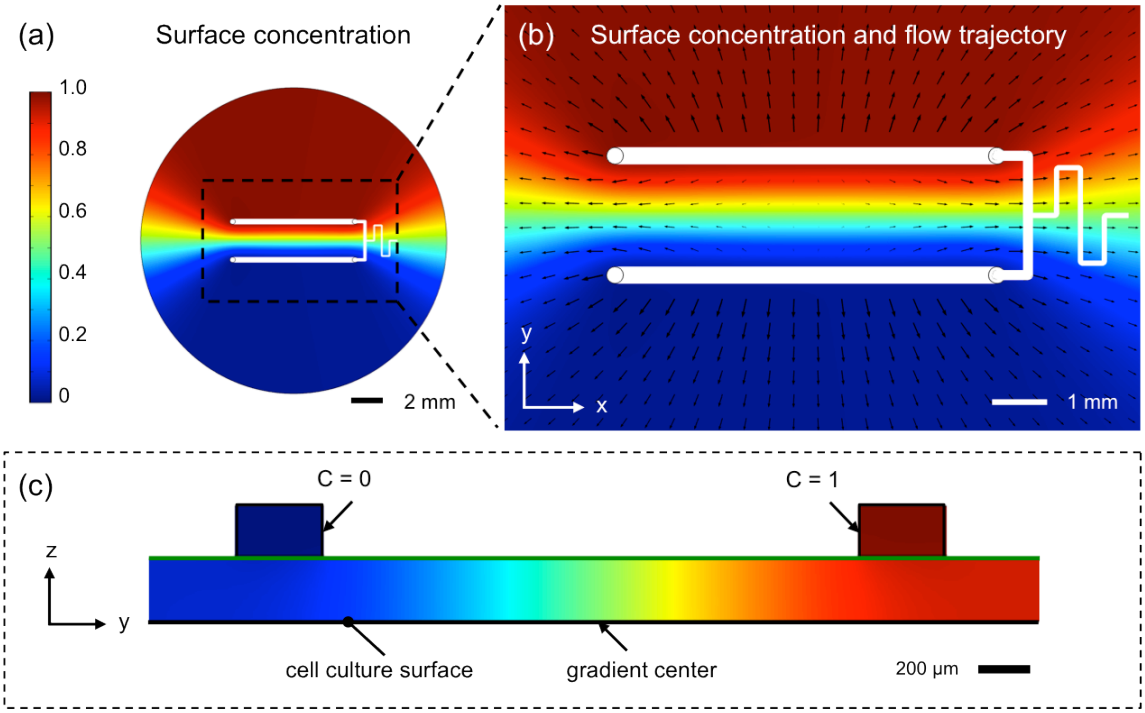

Figure 4.14: Steady-state simulation of surface concentration for a microfluidic transwell gradient. (a) A color map of the concentration profile produced when inputs are $C_1 = 0$ and $C_2 = 1$. The diffusing species modeled is fluorescein (6.4×10^{-10} m^2 s^{-1}). (b) An enlarged view of the gradient region between the negative and positive sources. Arrows represent the relative flow velocity and direction. (c) A cross-sectional view of the concentration gradient across the center of the device (at x = 0) in the y-z plane. The gradient is uniform in the z-direction.

4.4.2 Time dependent simulations of concentration gradient development

The effect of having a region of higher convection adjacent to a region of low convection (relative to the diffusion coefficient) is that the gradient is generated primarily by diffusive transport. The scenario presented by the microfluidic transwell device is an approximation of a linear gradient generated between a source and sink boundary conditions, because the flow ejected from the membrane curls away from the surface as shown in **Figure 4.13**. We studied the time-dependence of the evolving concentration profile by running simulations of the *Transport of Diluted Species* physics module with

time stepping against the steady-state solution for the flow. A series of concentration profiles in **Figure 4.15(a)** show the evolution of the surface gradient with time. In **Figure 4.15(b)** a series cross-sectional slices show the evolution of the gradient along the y-z plane. The traces in **Figure 4.15(c)** characterize the gradient shape in 2 min intervals from 0-4 hours and the final steady state solution.

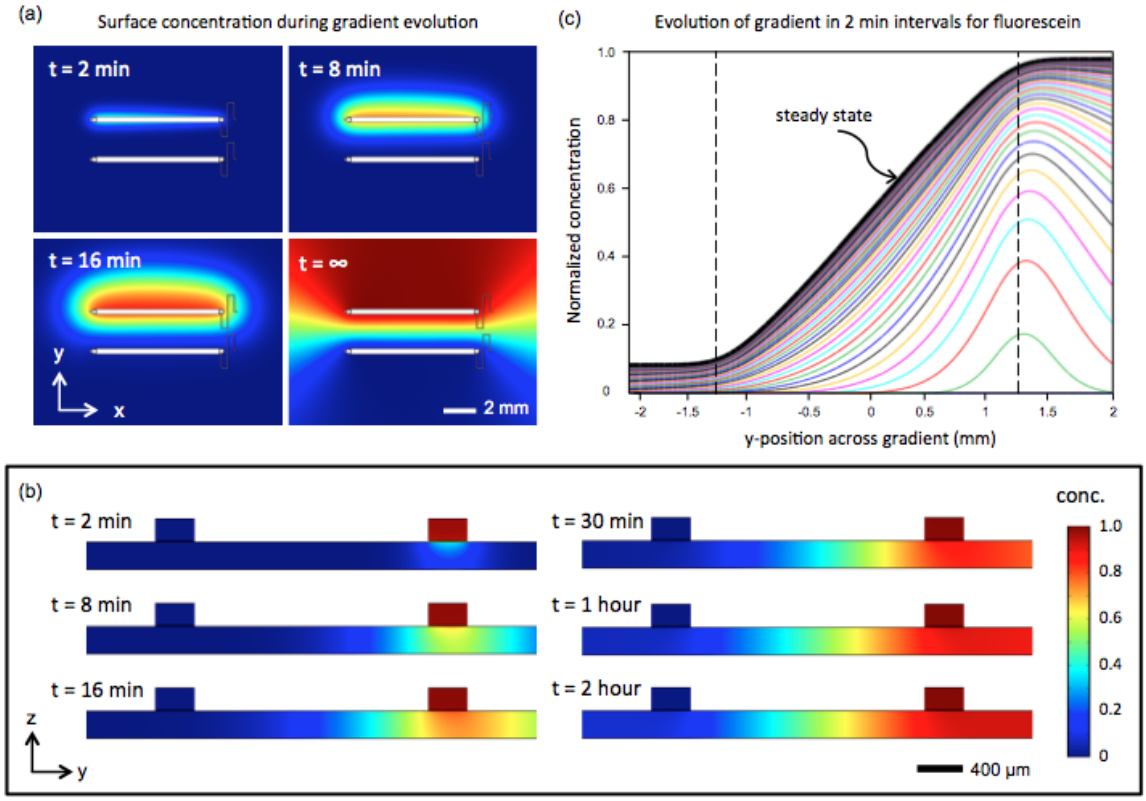

Figure 4.15: Time dependence of microfluidic transwell gradients. (a) A time series is shown for the surface gradient of a microfluidic transwell device flowing at 50 µL hr^{-1} with fluorescein, $D = 6.4 \times 10^{-10}$ m^2 s^{-1}. (b) A time series of cross-sectional slices of the concentration gradient in the y-z plane. (c) Surface concentration profiles across the width of the gradient in 2 min intervals from t = 0-4 hours and steady state.

4.4.3 Parametric study of flow rate and diffusivity sensitivity

A series of models were simulated to investigate the sensitivity of the device for flow rates and diffusion coefficients. The steady state flow was solved using the *Free and Porous Media Flow* module with the direct solver as previously described using a parametric sweep across flow rates of I_{in} = 10, 20, and 50 μL hr^{-1} then solved for convection and diffusion using diffusion coefficients for fluorescein, an intermediate molecule, and BSA (D = 6.4 × 10^{-10} m^2 s^{-1}, 3.2 × 10^{-10} m^2 s^{-1}, and 7.2 × 10^{-11} m^2 s^{-1}). The results shown in **Figure 4.16** demonstrate that there is a preferred range of flow rates for a given diffusing species to produce a linear gradient shape. As convective forces begin override diffusion, as is the case for slow diffusers like BSA and higher flow rates, the gradient profile becomes more parabolic. Similarly, for fast diffusers like fluorescein, at low flow rates diffusive mixing will flatten the gradient and raise the minimum and lower the maximum concentrations seen at the surface (**Figure 4.16(b)**). Flow rates of 50 μL hr^{-1} produce similar gradient shapes for the range of diffusing species tested. In order to conceptualize the molecular transport within the external fluid space, we can examine the ratio of advection to diffusion with the dimensionless local Péclet number for different diffusing species as shown in **Figure 4.17**. From this analysis, it is demonstrated that convection is the primary mode of transport at the boundaries of the delivery channel and regions extending to the periphery of the device, whereas diffusion is mainly responsible for the generation of the gradient.

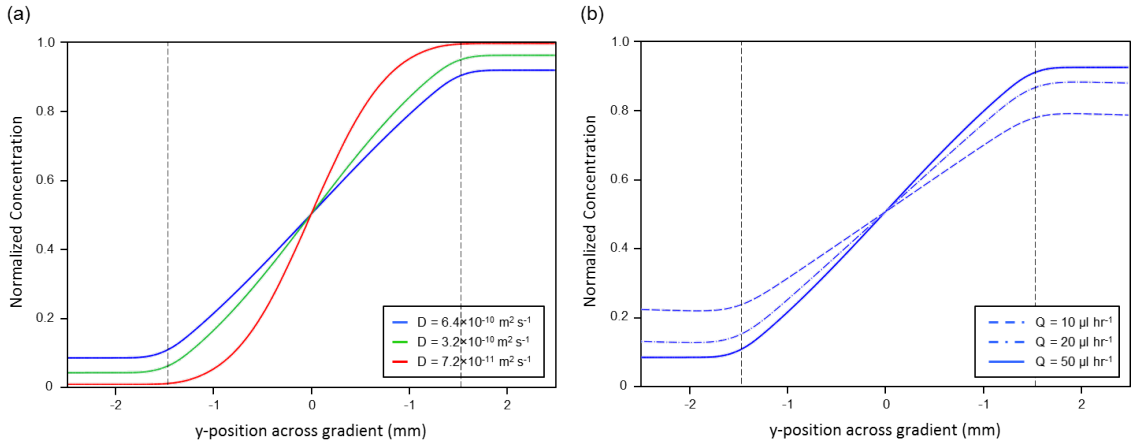

Figure 4.16: Convection and diffusivity dependence of microfluidic transwell gradients. (a) A series of concentration profiles for steady-state gradients for different diffusing species. (b) A series of concentration profiles for steady-state gradients generated for fluorescein at different flow rates.

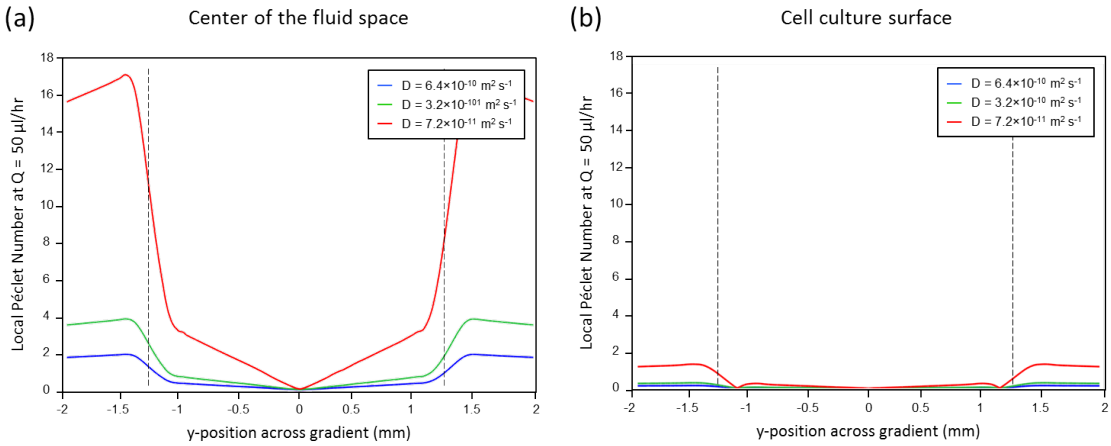

Figure 4.17: Local Peclét number analysis of simulated microfluidic transwell gradients. The local Peclét number is plotted across gradients at the (a) cell culture surface (z = 5 µm) and (b) the center of the fluid space (z = 125 µm) for different diffusing species at 50 µL hr^{-1}.

4.4.4 Shear stress at the cell culture surface

For cell culture studies, it is important to consider the effects of fluid shear stress on cell migration and cell viability. The shear stress imparted at the surface of the microfluidic transwell is described by the equation:

$$\tau = \mu \frac{\partial u}{\partial z} \tag{16}$$

where μ is the dynamic viscosity, and $\partial u/\partial z$ is the change in the horizontal component of the velocity vector with respect to the z-axis. Due to the dominant viscous forces at low Reynolds numbers and the no-slip condition the velocity changes sharply near the walls of the microchannels. The effect of different flow rates on the chemotactic migration of neutrophils was reported by Walker et al.[10]. They reported a migration bias in the direction of flow for neutrophils exposed to 687 mPa or greater shear stress. For the laminar flow gradient device used in their analysis, the flow rates required to generate shear stress below this threshold limited the overall gradient size and the amount of space in which to analyze responsive cells[10,11]. For neurons the shear stress sensitivity is much higher; Wu et al.[12] used optically actuated particles to create rotational fluid shear stress adjacent to the growth cones of axons in culture and found that as little as 1.2 mPa was required to elicit turning in the direction of shear stress. Furthermore, Wang et al[13] found that fluid shear stress of only 7.2 mPa was enough to cause retraction of axon outgrowth. Low fluid shear stress is essential then not only for unbiased chemotaxis results, but also studies with sensitive cell types such as neurons. We simulated the shear stress at the surface for the microfluidic transwell using the results of the flow velocity predicted for 50 μL hr^{-1} as shown in **Figure 4.18**. We found the shear stress at the cell culture surface to reach a maximum at 2.2×10^{-3} mPa; 4-5 orders of magnitude lower than the threshold for neutrophil migration bias and 2-3 orders of magnitude lower than the shear stress to induce growth cone turning. Importantly, the minimal shear stress is accomplished

without compromising the effective gradient area. In contrast, a typical approach to reducing shear stress is to limit overall flow rate and the effective gradient area for laminar flow mixing devices such as the type developed by Jeon et al.[11]

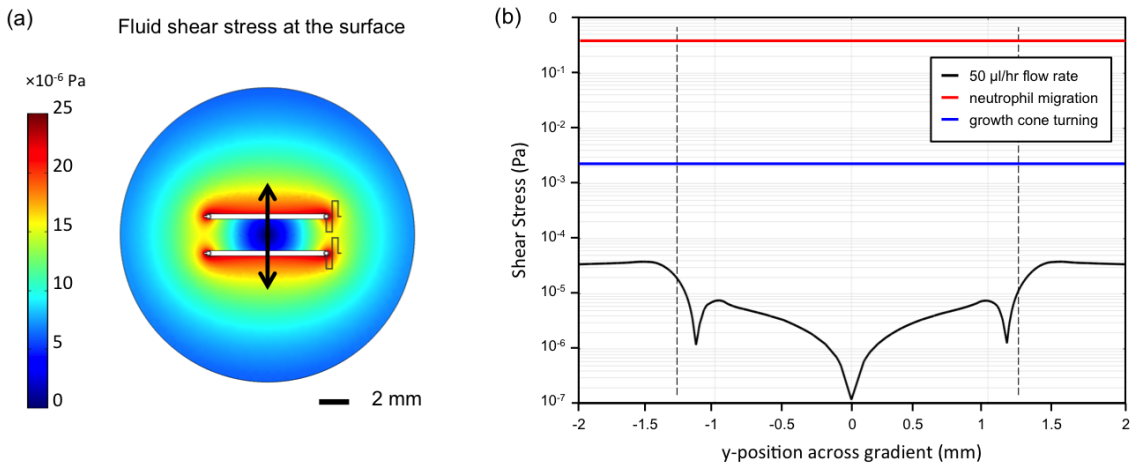

Figure 4.18: Fluid shear stress at the cell culture surface for microfluidic transwell gradients. (a) A color map of the fluid shear stress at the cell culture surface. Maximal shear stresses occur beneath the delivery channels as flows impinge on the surface after entering the fluid space through the membrane. (b) A plot of the fluid shear stress across the gradient and its comparison to the shear stresses reported for neutrophil migration bias and induced growth cone turning[10,12]. Local minima are the results of pseudo-stagnation points adjacent to the delivery channels and the central stagnation point. The maximum shear stress exerted by the microfluidic transwell at 50 µL hr^{-1} is 2.2×10^{-3} mPa.

4.5 Operation of Devices

For the operation of microfluidic transwell devices, they were first treated with oxygen plasma for 1 min using the same conditions for bonding. Immediately after plasma activation, devices were flushed with a few mL of water using a syringe and blunt 22g dispensing needle to connect to the inlets and outlets. For cell culture, devices were then immersed in water in a 6-well plate and UV treated for at least 2 hours to sterilize. Flow and solutions were supplied to the devices using a Fusion Touch 100 syringe pump

(Chemyx Inc., Stafford, TX) and 3 mL syringes with luer lock fittings, blunt dispensing needles, and thin bore Tygon tubing (Cole Parmer, Vernon Hills, IL) as shown in **Figure 4.19**. In order to connect to the device, first the top of the device is submerged under liquid and de-bubbled by manually rinsing with a spare syringe. Then syringes are installed in the syringe pump and primed so that liquid is dispensed from the inlet needles. With a flow rate of 50 uL hr^{-1} applied, the inlets are submerged into the liquid and then fitted into the device to ensure no air bubbles are trapped. For use with cell culture mediums special care must be paid to the filling of the syringes to prevent bubbles from accumulating. Drawing fluid into the syringe using the plunger will cause a large amount of bubbles from being trapped in the barrel. To prevent this, syringes are loaded by pipetting solution into the barrel and then the plunger is replaced. Air that is trapped at the plunger is dislodged by tapping the edge of the barrel. Fluid is primed to the edge of the luer and a sterile 0.2 μm syringe filter is fitted to maintain sterility. The loaded syringes are stored with the filter side upward in a 4 °C fridge for several hours or overnight. After refrigeration, air bubbles are drawn to the tip of the syringe and easily dispensed when priming the needles and tubing. Neglecting this step with cell culture mediums will generally result in bubbles nucleating in the tubing or syringe over the course of an experiment.

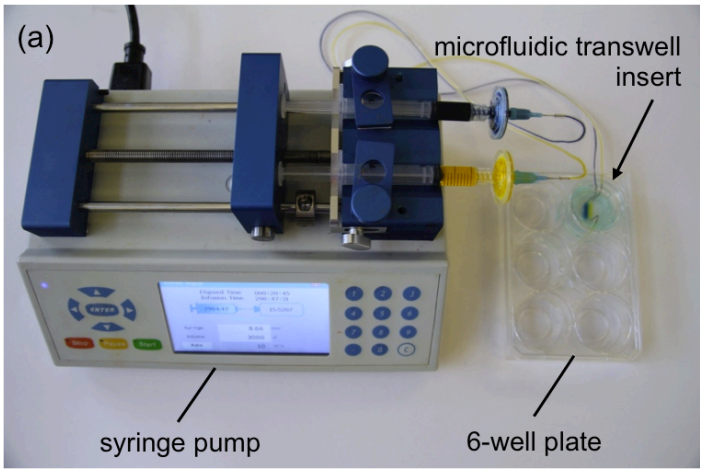

Figure 4.19: Experimental setup for device operation, cell culture, and microscopy. The device is fed through two 3 mL syringes, 22g dispensing needles, and small bore Tygon tubing. The apparatus is simple enough to be transported between cell culture hoods and microscopy stations. A primed and connected device can be stored in a fridge until needed or additionally UV treated to maintain sterility between successive experiments.

4.6 Characterization of Diffusible Gradients

Images were collected using a Nikon TE-Eclipse model inverted microscope equipped with automated objectives, fluorescence filter turrets, translational stage, and z-positioner (Nikon Instruments, Melville, NY). Images were acquired with a 12-bit cooled CCD camera (ORCA-ER, Hamamatsu, Japan). Nikon Elements-AR software was used to control acquisition and peripheral devices. A Perfect Focus System (PFS) module enables rapid, automated focusing through the detection of the fluid-cover glass interface of 6-well plates. Large surface area (20 mm diameter), phase-contrast and fluorescence images were stitched from large arrays of overlapping fields of view. An important feature, the PFS enables rapid acquisition of a large number of images in combination with the translational stage to generate time-lapse image sets. For on-stage incubation and imaging of cells, a Live-Cell stage insert (Pathology Devices) was used with CO_2, and temperature control.

4.6.1 Orange-G for characterization of surface-level gradients

Surface-level gradients were quantified using an imaging technique for adapting regular epi-fluorescence microscopy to collect surface-level intensity[14]. We can limit the penetration length of the excitation light into our sample by flowing a mixture of non-fluorescent and fluorescent dyes, Orange-G and fluorescein, respectively. The dyes are chosen because Orange-G absorbs strongly at the excitation wavelength (490 nm) and weakly at the emission wavelength of fluorescein (540 nm). In combination, the dyes compete for a finite amount of excitation energy. With a concentration of 40 mM for Orange-G the characteristic penetration length is approximately ~4.9 μm (for which the excitation light intensity is 1/e times the incident intensity of the excitation light)[15]. Since the intensity of the excitation light decays exponentially as it penetrates the solution, 95% of the collected emission light is from within ~15 μm of the surface of the well plate. Using this technique, we characterized the stability and uniformity of the device by imaging over a large area of approximately 25 mm square area as shown in **Figure 4.20**. Gradients evolved to steady state at around 1 hour and demonstrated long-term stability (here shown at 19 hours after continuous imaging and driving flow of 50 μL hr^{-1}). A comparison of the fluorescence intensity profiles taken across the gradient for every 2 min during evolution of the gradient shows strong similarity between the results of the time dependent FEM simulations (**Figure 4.20(c-d)**). In other instances, devices operated for up to 65 hours showed similar stable gradient profiles after placing on the microscope stage and collecting surface-level fluorescence images. A feature of the modular design, the gradients can be altered rapidly by repositioning the device or removing the device altogether. In **Figure 4.21** the device was repositioned at different angles by simply rotating the device relative to the original position in the 6-well plate.

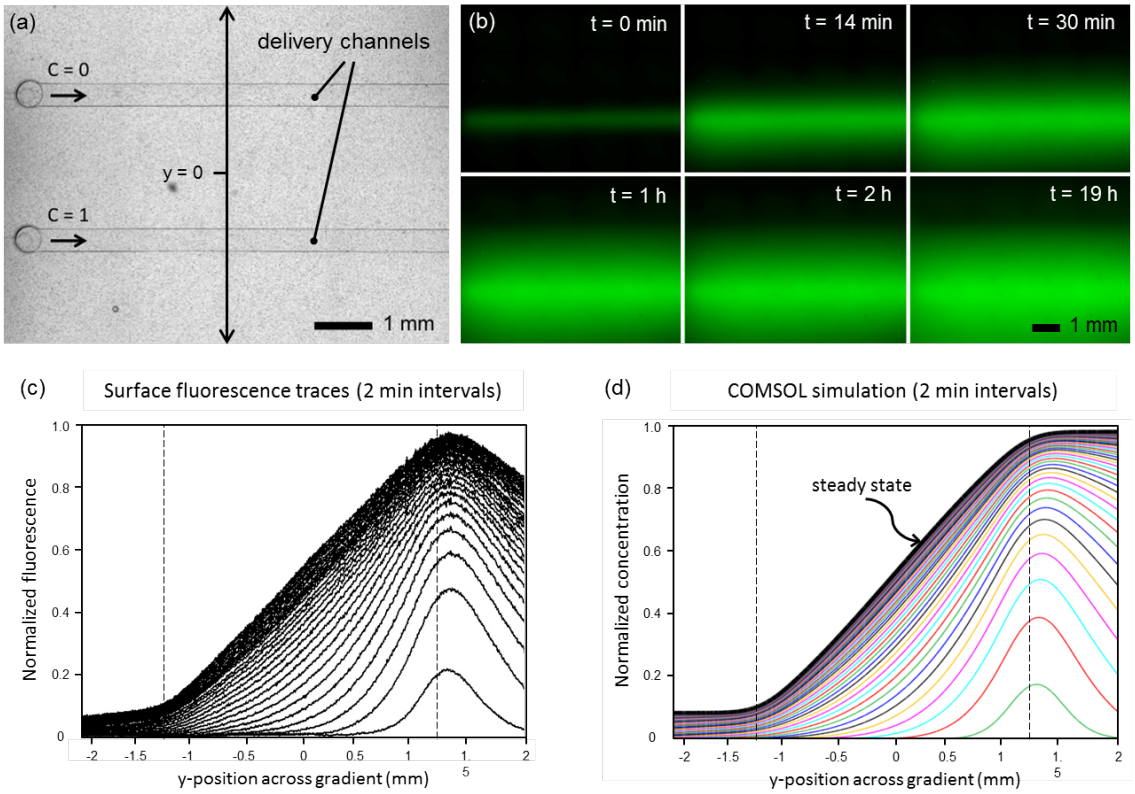

Figure 4.20: Characterization of the microfluidic transwell gradients using surface-fluorescence. (a) A large area bright-field image shows the area of interest and position of the delivery channels for the positive and negative gradient solutions that flow into the fluid space between the device and the well-plate surface. (b) A time series showing the evolution of the surface gradient for the region of interest shown in (a). At t = 0 min, the device was inserted into the well while flowing at a rate of 50 µL hr^{-1} (c) Fluorescence intensity profiles were plotted along the y-axis in the position indicated in (a) for 2 hours in 2 min increments. (d) The COMSOL simulation predicts a similar behavior for the evolution of the gradient profile with time. Vertical dotted lines indicate the position of the midpoint of the delivery channels with respect to the y-axis.

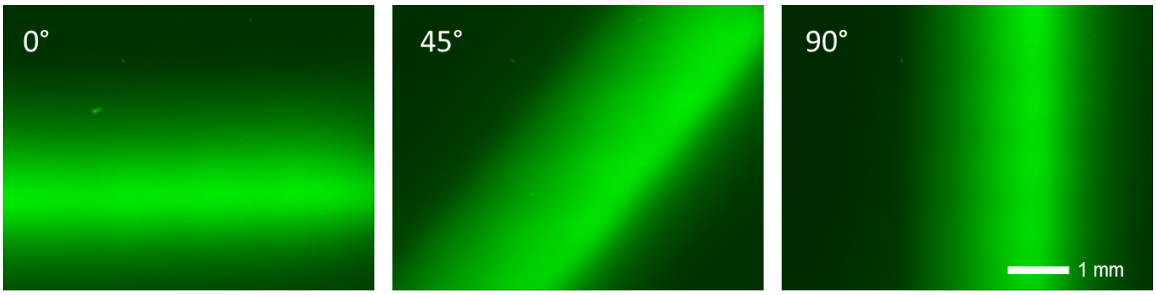

Figure 4.21: Demonstration of tunable gradients through rotation of the device. The series of surface-fluorescence images were taken at different rotational positions after allowing 30 min for the gradient to evolve using fluorescein and Orange G solutions.

4.6.2 Diffusible Tracers for Epi-Fluorescence Live-Monitoring

The surface-level fluorescence technique described previously was used as a general method for characterizing different device designs and operating parameters; however, it is not suitable for cell culture applications because the Orange G dye is cytotoxic at the concentrations used. An important feature for this device then is the ability to monitor the state of the gradient without the use of surface-level fluorescence or confocal microscopy. Since the concentration is uniform in z-direction of the device (see **Figure 4.14(c)** and **Figure 4.15(b)**) and the delivery microchannels are at the edges of the gradient space, the emission light collected from regular epi-fluorescence is linearly related to the surface concentration in the gradient region. Therefore, regular epi-fluorescence microscopy was used with fluorescently conjugated tracers to observe the development and steady state profiles for gradients generated with diffusing species of different molecular weights (**Figure 4.22**).

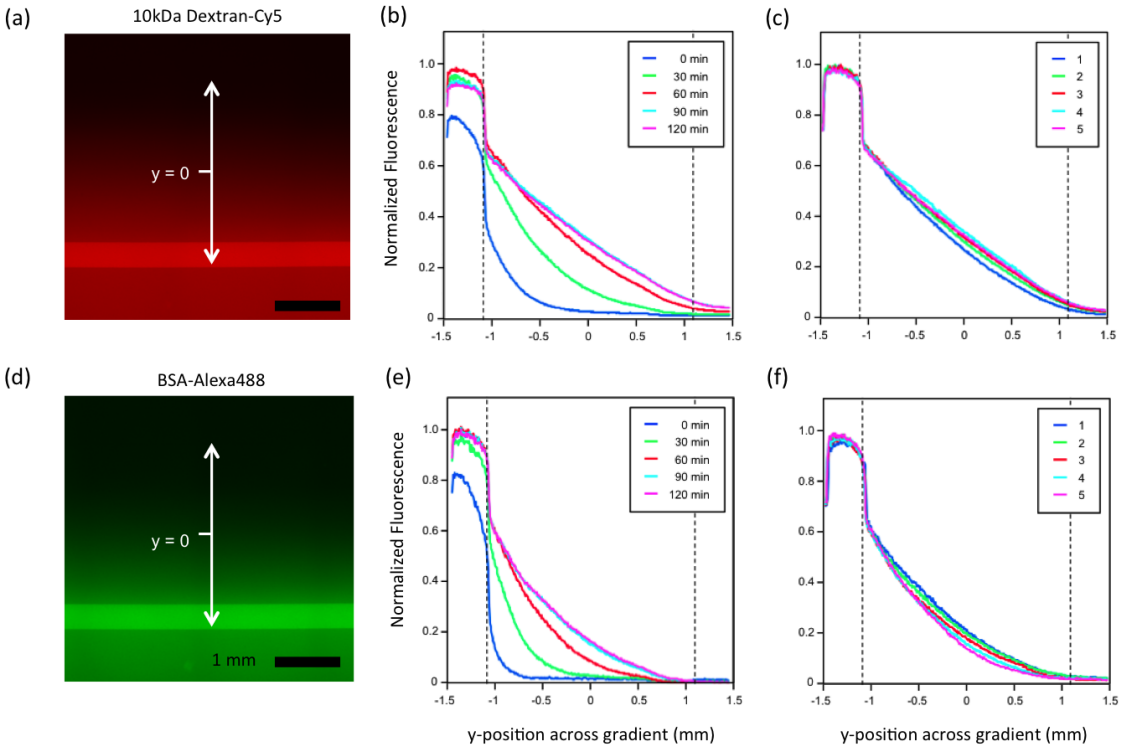

Figure 4.22: Live-monitoring of microfluidic transwell gradients using fluorescent tracers. (a) A large-area stitched epi-fluorescence image taken after 24 hours with 5 µM 10 kDa dextran-Cy5 in the lower channel and the device operated with Q = 50 µl hr^{-1}. (b) The fluorescence intensity profile of the gradient reaches steady state at approximately 90 min. (c) The gradient profile is plotted in five 2 mm increments along the length of the 8 mm delivery channel to demonstrate lateral uniformity. Similarly, the gradients generated for a BSA–Alexa488 conjugate show (d) steady state gradients, (e) evolution in 90 min, and (f) lateral uniformity.

4.7 Applications of Microfluidic Transwell Inserts to Cell and Tissue Cultures

The modular design of the microfluidic transwell insert affords broad applicability to cell and tissue cultures that can be prepared and maintained in conventional 6-well plates. Biological samples can be prepared using conventional technique before interfacing with the device to apply chemical gradients. The clear optical properties of the PDMS and PET materials used in the device allow for phase-contrast microscopy and imaging of individual cells. To demonstrate the low shear and large-area gradients we sought to observe unbiased chemotaxis by tracking the migration of a large population of cells. Additionally, we demonstrate application to neuronal tissue explants that are sensitive to shear stress and typically impossible to culture in an enclosed microchannel due to their large size (0.5-1 mm diameter).

4.7.1 HL-60 cell culture and device preparation

We used the promyelocytic leukemia HL-60 cell line which can be differentiated to a neutrophil-like phenotype[16,17]. HL-60s were obtained from American Type Culture Collection (Manassas, VA). Cells were grown and sub-cultured using RPMI 1640 with L-glutamine, 25 mM HEPES, and phenol red which was supplemented with 10% heat-inactivated fetal bovine serum and 1% antibiotic-antimycotic. Cells were propagated at initial concentrations of $0.1\text{-}0.2\times10^6$ cells mL^{-1} and passaged every 3-4 days before they reached 1×10^6 cells mL^{-1}. For differentiation, cells were passaged into fresh medium with 1.3% dimethyl sulfoxide at $0.1\text{-}0.2\times10^6$ cells mL^{-1} and cultured for 4-7 days during which cells adopt a granular and irregular morphology. For chemotaxis assays, Gey's medium was prepared using the formulation in **Table 4.1**. Glass-bottom 6-well plates were treated with 1 μg mL^{-1} human fibronectin (FC010, Millipore, Billerica, MA) for 15 min at room temperature. Wells were rinsed once with PBS solution then blocked for

15 min with 1% endotoxin-free BSA (Rockland Immunochemicals, Gilbertsville, PA). We observed that neglecting the blocking step with the 1% BSA solution or using higher concentrations of fibronectin resulted in over-adherent cells that could not sufficiently migrate. After blocking, the solution was aspirated and 200 μL of 20 nM fMLP in Gey's medium (F3506, Sigma-Aldrich, St. Louis, MO) was added to the well. 200 μL of cell suspension was dispensed into the well with the fMLP solution and allowed 15 min for cells to activate and attach to the surface. After attachment, the well was rinsed with 3-4 mL of fresh Gey's medium by gently rocking the plate and gentle aspiration. Remaining cells were covered with 2 mL of 0.2% BSA in Gey's medium in preparation for interfacing with the microfluidic transwell insert. The BSA facilitates cell motility by competing with the attachment of the cells to the coated surface.

Devices were operated as described earlier with 0.2% BSA in Gey's medium and driving flow at 50 μL hr^{-1}. For the gradient source syringe, 100 nM fMLP was used with 1 μg mL^{-1} of 3 kDa Dextran-Alexa488 to monitor the gradient. Typically, during preparation of substrates, the devices were setup and characterized using epi-fluorescence in a spare well-plate. When the cells were ready, the devices were transported to the cell culture hood and applied to the HL-60s in the sterile environment before imaging.

Components	Mol. Wt. (g/mol)	Molarity (mM)	Conc. (g/L)	Conc. (mg/L)	No. of particles	Osmolarity (mOsm/L)
KCl	74.551	6	0.447306	447.31	2	12
$MgCl_2$	95.21	1	0.09521	95.21	3	3
HEPES	238.3	20	4.766	4766.00	1	20
Na_2HPO_4	141.96	1	0.14196	141.96	3	3
NaCl	58.442	138	8.064996	8065.00	2	276
D-Glucose	180.16	5	0.9008	900.80	1	5
$CaCl_2$	110.983	1	0.110983	110.98	3	3

Table 4.1: Formulation for Gey's medium used in HL-60 chemotaxis assays.

4.7.2 Tracking of neutrophil migration and chemotaxis

Time-lapse images of HL-60s underneath microfluidic transwell gradients were collected at 30 second intervals using a Nikon TE-Eclipse as described earlier. Automated large-area image stitching was used to generate a composite image of 24 fields of view with 15% overlap using the 10X objective for phase-contrast and epi-fluorescence (**Figure 4.23(a)**). Automated shading correction was enabled in the NIS-Elements software to correct for non-uniform illumination of both phase-contrast and fluorescence images. 12-bit tiff images were collected with a bin of 2 that were sufficient to resolve single cells as shown in **Figure 4.23(b)**. Time-lapse image series of 1.5 hours in length were collected for experiments applying gradients of 100 nM fMLP and controls with either uniform 100 nM fMLP or no fMLP. The fluorescence images were used to verify the development of the fMLP gradient and equivalent flow conditions for the controls in which a tracer was still used (**Figure 4.24**).

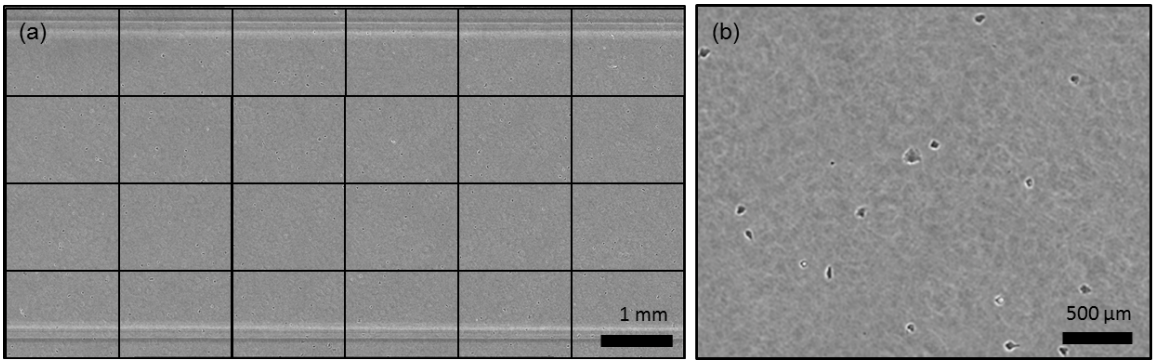

Figure 4.23: Large-area image stitching for time-lapse tracking of HL-60 migration during chemotaxis experiments. (a) A large-area stitched image was acquired every 25 seconds by capturing the composite of 24 individual fields of view using the motorized translation stage. (b) The cells are visible in phase-contrast for a single field of view captured using the 10X objective. High contrast, large-area imaging, and sufficient time resolution is essential for the automated tracking of individual migrating cells.

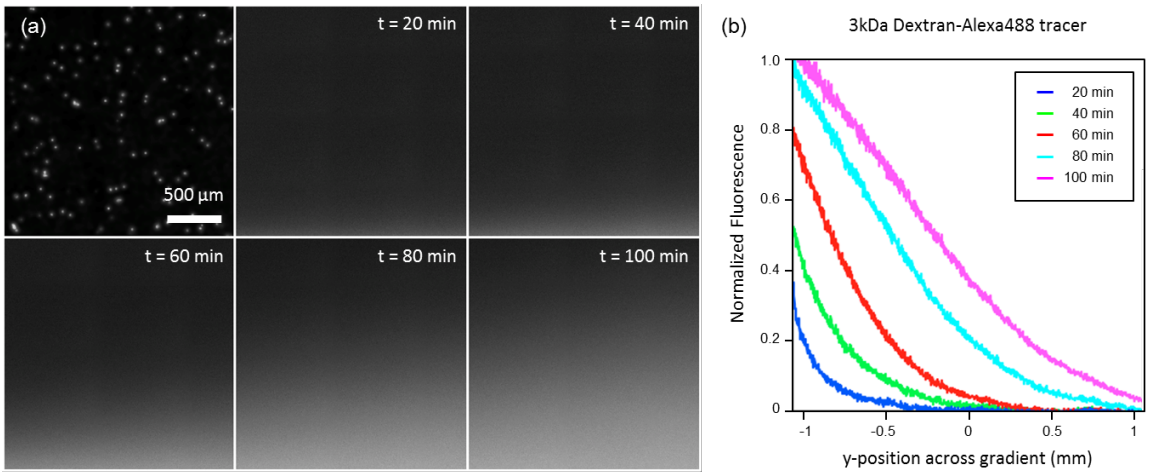

Figure 4.24: Monitoring of the 100 nM fMLP gradient with a fluorescent tracer during time-lapse of HL-60 chemotaxis. (a) A reference image showing the detected cells for a field of view spanning the length of the gradient and a time series of fluorescence images monitoring the 3 kDa Dextran-Alexa488 tracer. (b) The fluorescence intensity profiles corresponding to the time sequence demonstrate the evolution of the gradient.

Image processing and automated tracking of cells

Image processing and automated tracking of cell migration was accomplished in the FIJI package of Image J. First, the phase-contrast tiff images were processed using edge detection to enhance local regions of sharp changes in intensity as shown in **Figure 4.25(a-b)**. Next, images were despeckled to remove small diameter regions of high-intensity that result from background noise (**Figure 4.25(c)**). Finally, a Gaussian filter is used to smooth the images and fill in the low intensity "hole" from the center of the cell bodies. The final result, shown in **Figure 4.25(d)**, is a dark image with intensity maxima located roughly where the cell center was located in the original images.

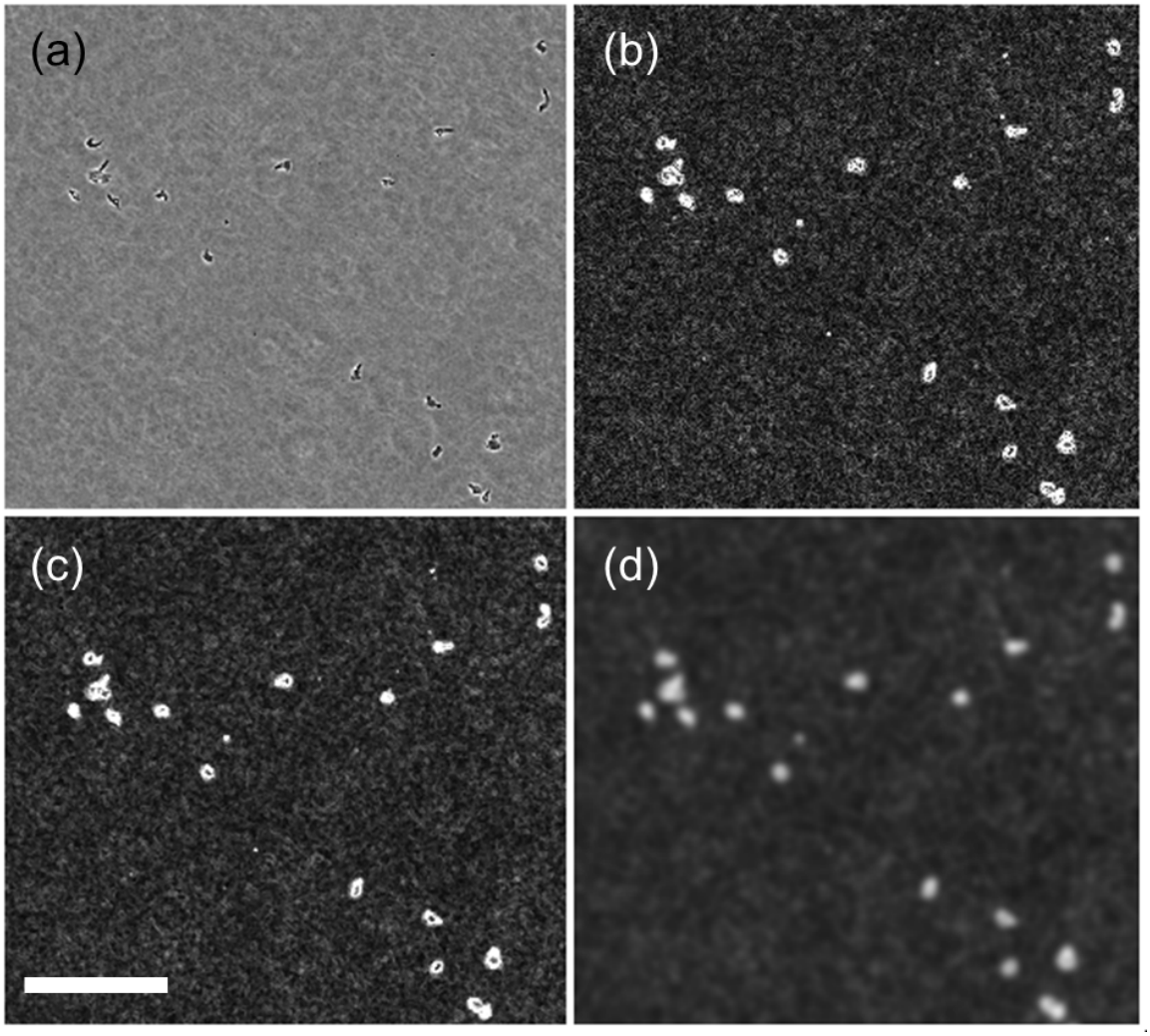

Figure 4.25: Image processing setup for automated identification of cell bodies with Image J. (a) A cropped view of an original phase-contrast image taken at 10X. (b) The edge detected image enhances sharp changes in contrast. (c) The despeckle filter is applied to remove small diameter and high intensity noise from the background. (d) A 4 pixel diameter Gaussian filter is applied to smooth the image and enhance identification of the cell bodies from high intensity regions. Scale bar is 100 μm.

TrackMate automated tracking of cell migration

The processed images were assembled as a stack of tiffs and analyzed using the TrackMate plugin developed for Image J based on the algorithm described in Jaqaman et al.[18]. The algorithm using a mathematical framework referred to as the Linear

Assignment Problem (LAP). TrackMate first identifies spots in each image of the stack based on the estimated diameter of the cells (20 μm) and a threshold value for the minimum intensity. The Otsu method was applied using the built-in plugin to determine the optimal value for the threshold fed into TrackMate. For the full large-area stitched image, it took approximately 1-1.5 hours for spot detection in a stack of 200 images. Next, the plugin solves the LAP by linking spots between frames based on several parameters for the entire image sequence (**Figure 4.26**). We used a frame-to-frame max linking distance of 20 μm, and a gap-closing distance of 50 μm for a maximum duration of 5 frames. Gap-closing enables linking spots between frames when the cell drops out of detection for a few frames. An example sequence of the TrackMate tracking for crowded cells is shown in **Figure 4.27**.

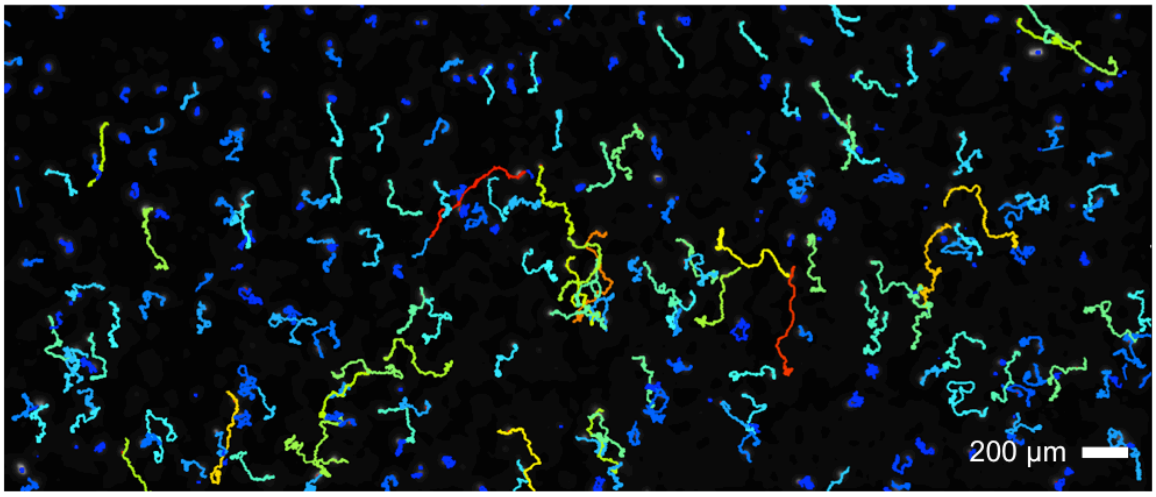

Figure 4.26: TrackMate plugin generated tracks for HL-60 cells and a 100 nM fMLP gradient. The color of the tracks represents increasing total displacement from blue to red in color.

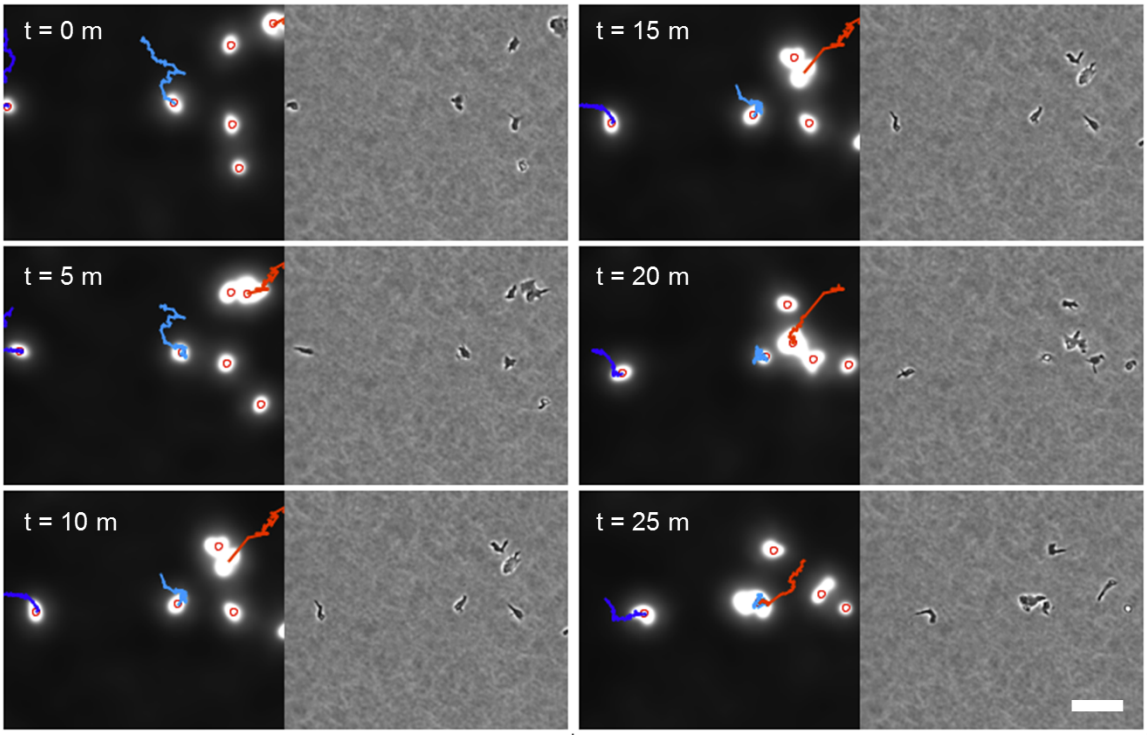

Figure 4.27: A TrackMate sequence showing the tracking of cells in crowded regions. The sequence of filtered (left) and phase-contrast (right) images is shown in 5 min intervals with the trace of the target cell shown in red for the last 50 frames. Detected spots are red circles. The TrackMate plugin loses detection for the red trace at frames t = 10, 15, and 25 min, however the gap closing capability resolves the trace by connecting segments even when cells pass through crowded areas. The scale bar is 50 µm.

Statistical analysis of chemotaxis parameters

After generating tracks, the plugin can output the data to an Excel file with the spot locations for each track generated. This file was then fed through a custom MATLAB code to sort and reformat the data so that the coordinates are sorted by frame for each track. The sorted data was then loaded into another freely available Image J plugin, the Chemotaxis and Migration Tool (Ibidi GmbH, Germany). Using the plugin, the full traces were filtered to remove non-migratory cells by applying a threshold of at least 10 μm in total displacement. The cumulative trajectory plots for the gradient data and the controls are shown in **Figure 4.28**. From a total of 282 cells observed in the

gradient, 208 migrated in the direction of the higher concentration of fMLP or 74% of cells. In comparison, an even distribution was seen for uniform fMLP and no fMLP with 51% and 50% of cells moving in direction of the negative y-axis (implying no directed response). We applied the Rayleigh statistical test for a circular distribution of points and found a low p-value ($p < 0.001$) indicating an irregular distribution. Controls did not have significant p-values (**Table 4.2**). We applied further statistical analysis of various chemotaxis parameters as described by Zengel et al.[19] for the measure of forward migration index (FMI), directedness, velocity, and total displacement of cells for each condition. The FMI for the x- or y-axis is calculated from the ratio of the vector component of that axis for the final displacement divided by the total accumulated cell path. The directedness is calculated from the ratio of the vector displacement to the total accumulated cell path. An unpaired Student-t test was applied between each condition as shown in **Figure 4.29**. The mean FMI, directionality, and total displacement for the 100 nM fMLP gradient group were statistically significant ($p < 0.0001$). The mean velocity of the gradient and uniform group were statistically significant ($p < 0.0001$) demonstrating that fMLP stimulates motility even in the absence of a gradient. The FMI, directionality, and total displacement were not statistically significant between the two controls indicating that cells exposed to uniform fMLP tended to meander even though there overall migration speed and accumulated distance was greater.

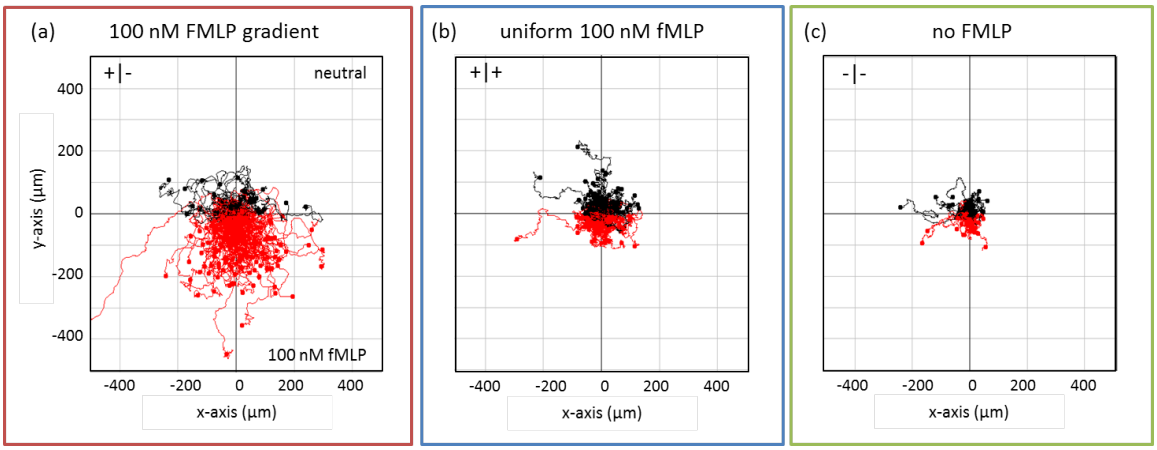

Figure 4.28: Trajectory plots for 100 nM fMLP gradient and controls showing the cumulative traces of each individual cell tracked. (a) The red traces designate cells which migrated down (towards higher fMLP for the gradient) and black for cells which migrated upwards. The cumulative traces for controls with (b) uniform 100 nM fMLP and (c) no fMLP show even distribution of cells migrating in either direction.

Condition		Total number of cells	Number of cells migrated in y-axis	p-value (Rayleigh test)
gradient	+|-	n = 282	+74/-208	p = 2.36×10 -28
uniform	+|+	n = 379	+184/-195	p = 0.69
neutral	-|-	n = 127	+64/-63	p = 0.54

Table 4.2: Results of chemotaxis and control experiments with the Rayleigh test for a circular distribution.

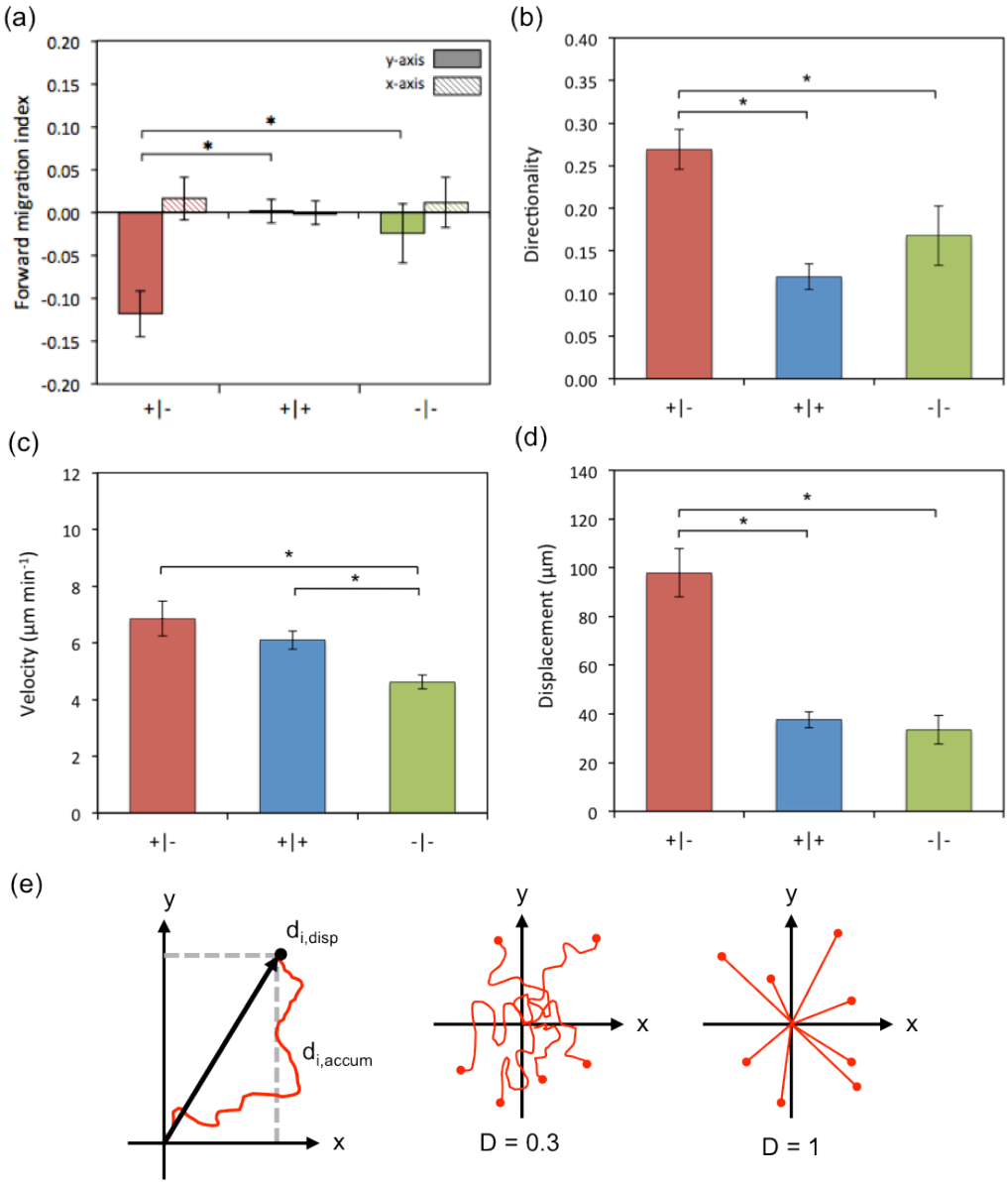

Figure 4.29: Statistical analysis of chemotaxis for HL-60 migration experiments. (a) The forward migration index measures effectiveness of migration in a particular direction for the y-axis or x-axis. (b) The directionality is a measure of the straightness of the cells trajectory relative to the final position. (c) The average velocity. (d) The vector displacement. (e) A schematic of a single trajectory showing the vector and cumulated displacement on the left and different directedness ratios on the middle and right. Whiskers indicate the 95% confidence intervals and (*) indicates $p < 0.0001$.

4.7.3 Application to Retinal Explant Tissue Cultures

Retinal explants were harvested from timed pregnant mice supplied by Charles River Laboratories. Pregnant mice were dissected in accordance with a protocol approved by the University of Washington Animal Care and Use Committee. The eyes of the E15 pups were enucleated while immersed in artificial cerebral spinal fluid (ACSF) while bubbled with 5% CO_2, 95% O_2. The retinal pigment epithelium, the lens, and the vitreous humor were extracted to reveal the intact retina tissue. Retinas were fragmented into quadrants and plated onto glass-bottom 6-wells that were coated with 25 μg/ml poly-d-lysine and 12.5 μg/ml laminin overnight at 4 °C. Medium used for retinal culture (Neurobasal, 2% B27, 1% N2, 2 mM GlutaMAX, 1% antibiotic-antimycotic) was supplemented with 0.4% methylcellulose. Methylcellulose increases the viscosity of the medium and assists in maintaining attachment of the explants. For normal cultures as shown in **Figure 4.30**, the addition growth factors, 50 ng mL^{-1} brain-derived neurotrophic factor (BDNF) and 10 ng mL^{-1} cilliary neurotrophic factor (CNTF), were added to medium as described by Barres et al.[20]

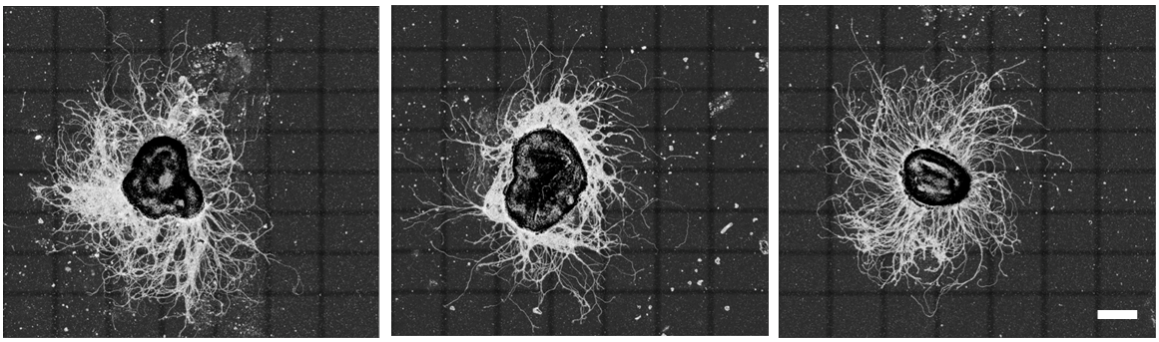

Figure 4.30: E15 mouse retinal explants after 40 h cultured with BDNF and CNTF growth factors. Large-area stitched images are shown after edge detection to enhance neurite contrast. The scale bar is 250 µm.

In a preliminary study, we applied the microfluidic transwell device to an E15 embryonic mouse retinal explant cultured using conventional methods but without the addition of growth factors. The explant was cultured in a glass-bottom 6-well plate using standard culture protocol for 3 days in vitro before the device was applied to generate a gradient of 50 ng/ml BDNF and 10 ng/ml CNTF for the duration of 12 h as shown in **Figure 4.31**. Large-area stitched images where taken with a time-lapse to observe the resulting neuronal outgrowth. Since the microfluidic transwell is modular by design, we tested the effect of disrupting the outgrowth by removing the device, agitating the surrounding medium, and applying a new gradient of 20 μM Sp-8-Br-cAMP (Santa Cruz Biotechnology, CA) (**Figure 4.32**). Sp-8-Br-cAMP is a cell membrane permeable cyclic adenosine monophosphate (cAMP) analog[21]. We chose cAMP because it is a key mediator of growth cone responses to a number of extracellular guidance molecules and previously implicated in micropipette-based studies with single neurons[21,22].

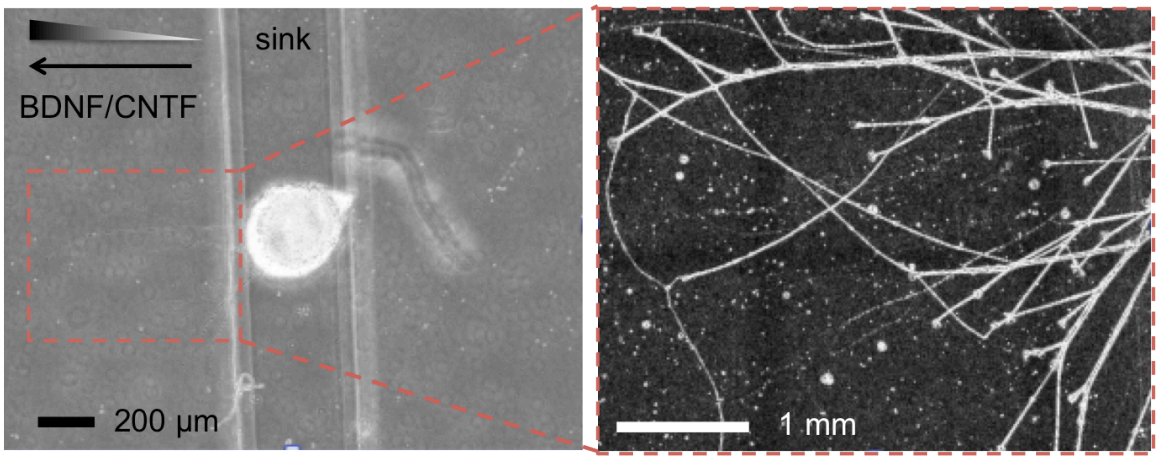

Figure 4.31: Application of a microfluidic transwell gradient of BDNF and CNTF growth factors to a retinal explant cultured 3 days in vitro. (Left) large area stitched images were collected over the course of a 12 h time-lapse. (Right) An enlarged view with an edge detection filter applied to enhance contrast.

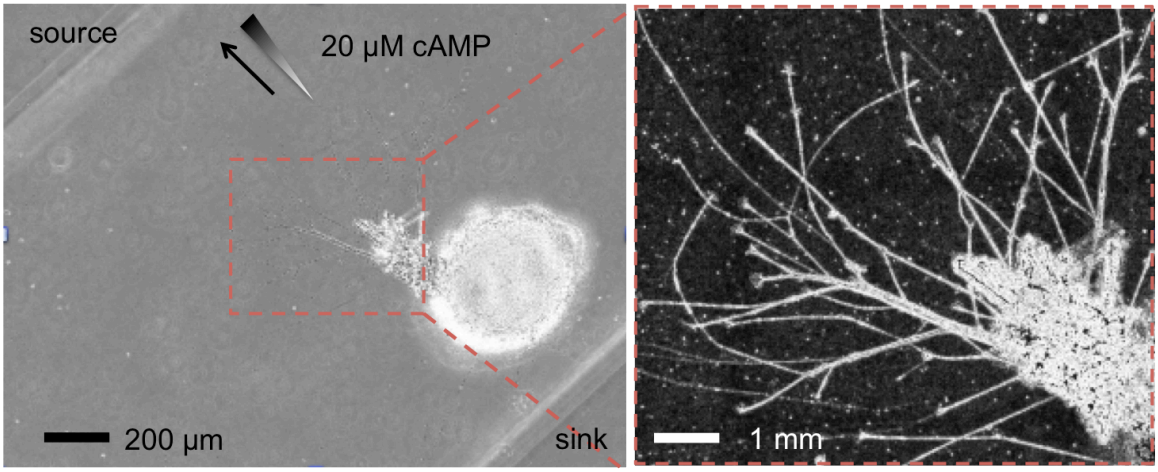

Figure 4.32: Repositioning of the microfluidic transwell and application of a new gradient using a cAMP analog. The device was removed and outgrowth was disrupted by agitating the medium. The device was then reapplied with a gradient of 20 µM. (Left) Large-area stitched images were collected over the course of a 12 h time-lapse. (Right) An enlarged view with an edge detection filter applied to enhance contrast.

Automated analysis of axon directionality

Analysis of axon outgrowth directionality was performed using the Image J plugin 'Directionality', developed by Jean-Yves Tinevez and demonstrated by Woolley et al.[23]. A selection of 681x1224 pixels was cropped from the final time point of the BDNF/CNTF and cAMP gradients, flipped horizontally, and analyzed using the plugin (**Figure 4.33**). The plugin uses Fourier spectrum analysis to calculate the preferred orientation of structures in the image[24]. It then generates a histogram for the amount of structures in a given direction with the positive x-axis designated as an angle of 0°. From the manual, it states that images with completely isotropic content are expected to give a flat histogram, whereas images in which there is a preferred orientation are expected to give a histogram with a peak at that orientation. The plugin generated statistics for the highest peak for each area analyzed (**Table 4.3**).

In **Table 4.3** the 'direction' designates the angle of the center of the Gaussian function fitted to the peak for the histogram (**Figure 4.33(c)**). The 'dispersion' is the standard deviation of the fitted Gaussian. The 'amount' is the sum of the histogram data from the center plus and minus a standard deviation divided by the total sum of the histogram, which is a measure of the relative frequency of objects at the peak angle. The 'goodness' reports the quality of fit for the data, with '1' being best fit and '0' being worst fit. The Directionality plugin calculated a peak direction angle of $\theta = -3.99°$ for the horizontally applied growth factor gradient and $\theta = 42.1°$ for the gradient of cAMP applied at 45°. This image analysis technique could be useful for analyzing large data sets of convoluted neurite outgrowth in a computationally efficient and automated manner.

Condition	Direction	Dispersion	Amount	Goodness
BDNF/CNTF at 0°	-3.99	1.26	0.17	0.51
cAMP at 45°	42.1	1.05	0.09	0.44

Table 4.3: Results for Fourier spectrum analysis of retinal explant outgrowth.

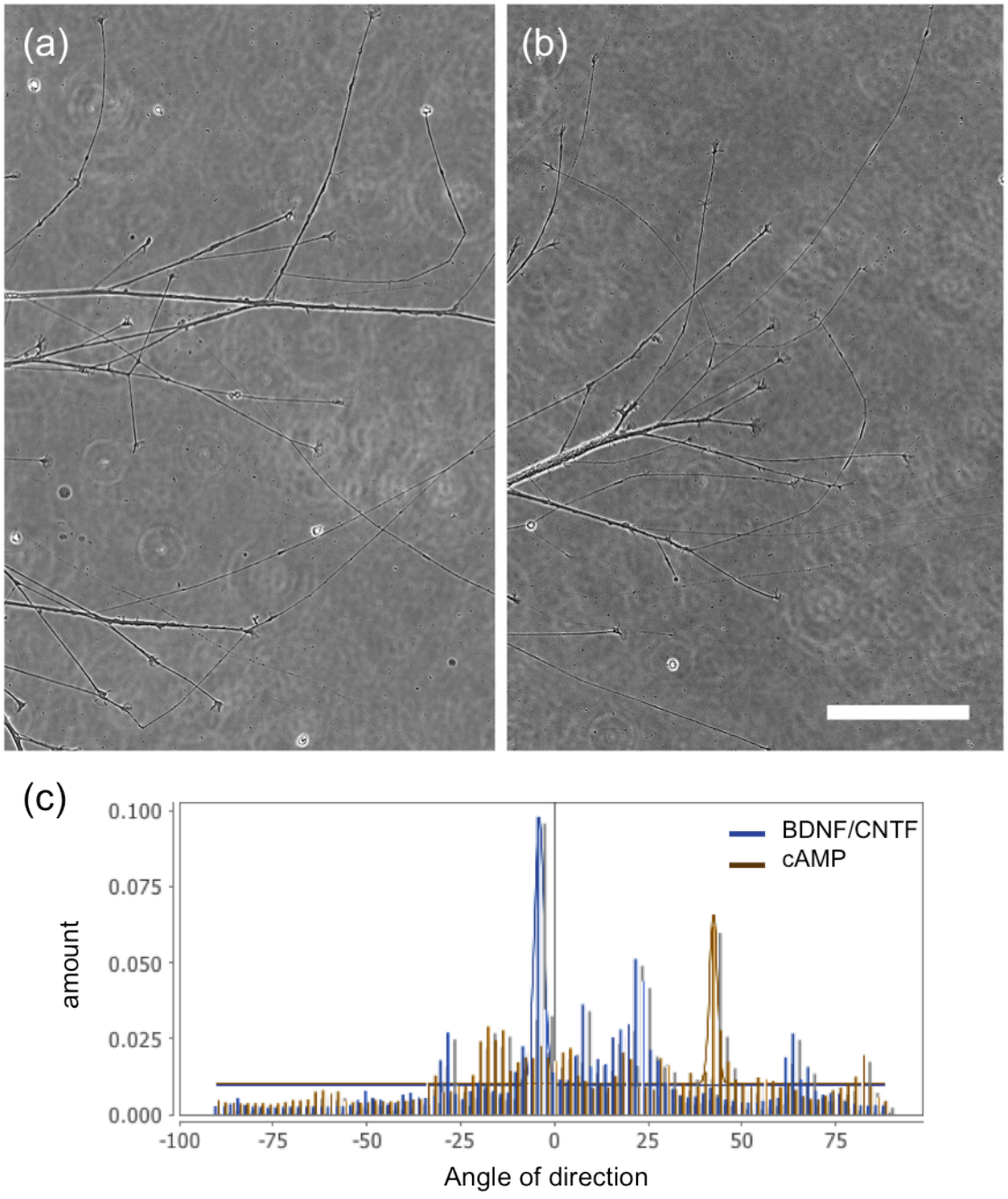

Figure 4.33: Fourier spectrum analysis of neuronal outgrowth for gradients of growth factors applied at 0° and cAMP at 45°. The images analyzed for the (a) BDNF/CNTF gradient and (b) cAMP analog were flipped horizontally. (c) The histogram generated by the plugin shows a distinct peak for the growth factor gradient near at 0° and cAMP at 42°.

4.8 SUMMARY AND FUTURE WORK

In this chapter, we have described the development of a cell culture-friendly gradient generating device. The novel design strategy of the microfluidic transwell device satisfies 5 important criteria for gradient generator design: (1) quantifiable gradients, (2) large numbers of cells or tissue, (3) direct observation of cells, (4) user-friendly operation, and (5) compatibility with conventional cell culture technique. Finite-element modeling was used to predict porous membrane flows and resulting gradients. The device was used to analyze the chemotaxis of HL-60 cells using direct visualization and automated image analysis. Our results demonstrate a significant chemotaxis response for HL-60 cells towards a gradient of 100 nM fMLP. Furthermore, the low-shear exerted by the porous membrane flows enables the device to interface directly with neuronal tissue explants. In a preliminary experiment, we demonstrated application of the device to an existing retinal explant culture and demonstrated outgrowth indicative of a gradient response. Future studies could explore application of the microfluidic transwell for different cell types and gradient sensing biology without necessarily changing the overall design because it interfaces simply with standard cell culture 6-well plates. This characteristic makes the microfluidic transwell suitable for translation and dissemination to non-microfluidic oriented laboratories. Ultimately, our contributions to the development of microfluidic technology and in vitro gradient assay technique are important to the further study of gradient sensing biology.

4.9 REFERENCES

1. Keenan TM, Folch A. Biomolecular gradients in cell culture systems. *Lab Chip*. 2008;8(1):34.

2. Kim S, Kim HJ, Jeon NL. Biological applications of microfluidic gradient devices. *Integr Biol*. 2010;2(11-12):584.

3. Wu J, Wu X, Lin F. Recent developments in microfluidics-based chemotaxis studies. *Lab Chip*. 2013;13(13):2484–2499.

4. Apel P. Track etching technique in membrane technology. *Radiat Meas*. 2001;34(1–6):559–566.

5. Cate DM, Sip CG, Folch A. A microfluidic platform for generation of sharp gradients in open-access culture. *Biomicrofluidics*. 2010;4(4):044105.

6. Xia Y, Whitesides GM. Soft Lithography. *Angew Chem Int Ed*. 1998;37(5):550–575.

7. Hsu C-H, Chen C, Folch A. Microcanals for micropipette access to single cells in microfluidic environments. *Lab Chip*. 2004;4(5):420.

8. Oh KW, Lee K, Ahn B, Furlani EP. Design of pressure-driven microfluidic networks using electric circuit analogy. *Lab Chip*. 2012;12(3):515–545.

9. Le Bars M, Worster MG. Interfacial conditions between a pure fluid and a porous medium: implications for binary alloy solidification. *J Fluid Mech*. 2006;550:149–173.

10. Walker GM, Sai J, Richmond A, Stremler M, Chung CY, Wikswo JP. Effects of flow and diffusion on chemotaxis studies in a microfabricated gradient generator. *Lab Chip*. 2005;5(6):611–618.

11. Jeon NL, Baskaran H, Dertinger SKW, Whitesides GM, Van de Water L, Toner M. Neutrophil chemotaxis in linear and complex gradients of interleukin-8 formed in a microfabricated device. *Nat Biotechnol*. 2002;20(8):826–830.

12. Wu T, Nieminen TA, Mohanty S, Miotke J, Meyer RL, Rubinsztein-Dunlop H, Berns MW. A photon-driven micromotor can direct nerve fibre growth. *Nat Photonics*. 2012;6(1):62–67.

13. Joanne Wang C, Li X, Lin B, Shim S, Ming G, Levchenko A. A microfluidics-based turning assay reveals complex growth cone responses to integrated gradients of substrate-bound ECM molecules and diffusible guidance cues. *Lab Chip*. 2008;8(2):227.

14. Bancaud A, Wagner G, Dorfman KD, Viovy JL. Measurement of the surface concentration for bioassay kinetics in microchannels. *Anal Chem*. 2005;77(3):833–839.

15. Bhattacharjee N, Li N, Keenan TM, Folch A. A neuron-benign microfluidic gradient generator for studying the response of mammalian neurons towards axon guidance factors. *Integr Biol*. 2010;2(11-12):669.

16. Collins SJ. The HL-60 promyelocytic leukemia cell line: proliferation, differentiation, and cellular oncogene expression. *Blood*. 1987;70(5):1233–1244.

17. Hauert AB, Martinelli S, Marone C, Niggli V. Differentiated HL-60 cells are a valid model system for the analysis of human neutrophil migration and chemotaxis. *Int J Biochem Cell Biol*. 2002;34(7):838–854.

18. Jaqaman K, Loerke D, Mettlen M, Kuwata H, Grinstein S, Schmid SL, Danuser G. Robust single particle tracking in live cell time-lapse sequences. *Nat Methods*. 2008;5(8):695–702.

19. Zengel P, Nguyen-Hoang A, Schildhammer C, Zantl R, Kahl V, Horn E. μ-Slide Chemotaxis: A new chamber for long-term chemotaxis studies. *Bmc Cell Biol*. 2011;12:21.

20. Meyer-Franke A, Kaplan MR, Pfrieger FW, Barres BA. Characterization of the signaling interactions that promote the survival and growth of developing retinal ganglion cells in culture. *Neuron*. 1995;15(4):805–819.

21. Murray AJ, Tucker SJ, Shewan DA. cAMP-dependent axon guidance is distinctly regulated by Epac and protein kinase A. *J Neurosci*. 2009;29(49):15434–15444.

22. Song H, Ming G, Poo M. cAMP-induced switching in turning direction of nerve growth cones. *Nature*. 1997;388(6639):275–279.

23. Woolley AJ, Desai HA, Steckbeck MA, Patel NK, Otto KJ. In situ characterization of the brain–microdevice interface using Device Capture Histology. *J Neurosci Methods*. 2011;201(1):67–77.

24. Liu ZQ. Scale space approach to directional analysis of images. *Appl Opt*. 1991;30(11):1369–1373.